LINC-NIRVANA Piston Control
and
Near-Infrared Polarization Images
of the Orion Proplyds

vorgelegt von

Steffen Rost
aus Düsseldorf

Köln 2008

Abstract

This thesis is focussed on the development of optimized techniques to overcome limitations of astrophysical observations. The goal is an optimal signal estimation in noisy measurements by the consideration of underlying physical processes. This principle was applied to two different fields in astrophysics: intrumental design and analysis of polarimetric observations.

In the observational part of this thesis near-infrared images of young stellar objects in the Orion constellation are studied. Limitations in resolution and sensitivity of current astronomical instruments prohibit the detailed analysis of interesting proto-stellar sources to improve theories of star formation. Radiation from the astronomical targets is not only characterized by its spectral energy, but also by polarization properties. The modeling of typical configurations of star-disk systems and the simulation of their polarization patterns helped to understand and interprete features, that were found in observations.

For the case of a proto-stellar systems with both a disk and an envelope analysis techniques were developed, which are based on polarimetric effects of the scattering of light by dust. These techniques substantially improve the sensitivity and resolution and are reliable under different observing conditions. Although the obtained data did not allow investigations of substructures of the circumstellar material, the techniques are suitable to obtain constraints on star formation processes. With larger telescopes, such as the Large Binocular Telescope (LBT), the analysis of principles down to the scale of planet formation will be possible.

LINC-NIRVANA, the near-infrared imaging system at the LBT, will provide unprecedented resolution and sensitivity performance combined with a wide field of view. The interferometric combination of light from two telescopes imposes new challenges in the instrument design. A so-called fringe tracker is mandatory for the interference of light at the detector by compensating optical path differences with an actuated mirror. The performance suffers from structural vibrations, limited sensitivity of sensors and processing latencies. The dynamics of actuators with significant amount of moving masses are limited. These effects are studied in the instrumental part of this thesis.

Giant telescopes with large mirrors and high-resolution instruments are complex, expensive projects. The telescope time, i.e. the allocated time to the observations of individual astronomical topics, is very limited and hence valuable. It is of great importance to improve the performance in terms of sensitivity and

resolution of observations under difficult conditions.

By modeling all performance related subsystems of the interferometric instrument critical parameters were identified. For a realistic model several precision measurements of the telescope and parts of the LINC-NIRVANA instrument were necessary. Simulations of atmospheric effects completed the model.

Several approaches for the optimization of the instrument performance were proposed. The determination of atmospheric and instrumental optical path difference or differential piston is improved by the detailed analysis of the statistical variation and appropriate filtering. The application of modern control theory provides stability and optimal dynamic response of the mirror actuator.

Since both parts of this thesis deal with the impact of the atmosphere on the observational result of astronomical instruments, chapter 1 gives an overview on the basic principles and techniques. Chapter 2 presents the modeling and control analysis of the fringe tracker for the LINC-NIRVANA instrument. A software simulation is introduced and first results of a laboratory experiment are denoted. Chapter 3 gives a short introduction into star formation theories and unsolved problems, followed by the detailed description of polarimetric observations of proto-stellar objects in the Orion constellation in chapter 4. Some concepts and atmospheric effects as introduced in chapter 1 are discussed. Promising findings of one source of the sample led to extensive modeling and analysis of polarimetric properties of proto-stars and the development of innovative analysis techniques, presented in chapter 5. In the last chapter these methods are applied to the observational data and the obtained configuration parameters are compared to results of previous investigations in the literature.

Zusammenfassung

Diese Dissertation befasst sich mit der Entwicklung von optimierten Methoden, die die Einschränkungen astrophysikalischer Beobachtungen kompensieren können. Das Ziel ist die optimale Bestimmung von Signalen aus verrauschten Messungen unter der Berücksichtigung der zugrunde liegenden physikalischen Prozesse. Dieses Prinzip wurde auf zwei Bereiche der Astrophysik angewendet: die Entwicklung eines astronomischen Instruments und die Analyse von polarimetrischen Beobachtungen.

Nahinfrarot-Bilder von jungen Sternen im Orion werden im beobachtenden Teil dieser Arbeit untersucht. Die eingeschränkte Auflösung und Empfindlichkeit heutiger astronomischer Instrumente verhindern genauere Analysen von Proto-Sternen, die nötig wären, um ausstehende Fragen der Theorie der Sternentstehung beantworten zu können. Die Strahlung solcher Quellen ist dabei nicht nur durch ihre spektrale Energieverteilung charakterisiert, sondern auch durch ihre Polarisation. Das Modellieren typischer Stern-Scheiben-Systeme und das Simulieren ihrer Polarisationsmuster half bei der Interpretation von Merkmalen, die in Beobachtungen auftauchten.

Für protostellare Systems, die sowohl eine Staubhülle, als auch eine protoplanetare Scheibe aufweisen, wurde eine Methode zur Analyse entwickelt, welche auf polarimetrischen Effekten der Streuung von Licht durch den umgebenden Staub beruht. Diese Methode verbessert erheblich die Empfindlichkeit und Auflösung und ist auch unter schwierigen Beobachtungsbedingungen verlässlich. Obwohl die verwendeten Daten keine Untersuchungen der Unterstruktur des den Stern umgebenden Materials zuließen, konnten mit dieser Technik Parameter der Sternentstehungsprozesse bestimmt werden. Mit größeren Teleskopen wie das Large Binocular Telescope (LBT) wird dann die Beobachtung kleiner Strukturen bis hinab zur Planetenentstehung möglich sein.

LINC-NIRVANA ist das Nahinfrarot Kamerasystem am LBT und wird unerreichte Empfindlichkeit und Auflösung mit einem großen Blickfeld paaren, sobald es den Betrieb aufgenommen hat. Die interferometrische Zusammenführung des Lichts von zwei Teleskopen bedeutet eine Herausforderung bei der Konstruktion des Instruments. Für die kohärente Überlagerung ist ein so genannter "Fringe Tracker" zwingend notwendig, um Gangunterschiede mit einem bewegten Spiegel ausgleichen zu können. Die Regelgüte wird dabei beeinflusst von Vibrationen, begrenzter Empfindlichkeit der Sensoren und Verzögerungen

bei der Verarbeitung der Signale. Eine erhebliche zu bewegende Masse begrenzt die Dynamik des Aktuators. Der instrumentelle Teil dieser Arbeit beschäftigt sich mit diesen Effekten.

Grosse Teleskope und hochauflösende Instrumente sind komplexe und teure Projekte und die Zeit, die den verschiedenen astronomischen Gebieten zur Beobachtung zur Verfügung steht, ist limitiert. Es ist daher von großer Wichtigkeit, die Qualität der Beobachtungen auch unter schwierigen atmosphärischen Bedingungen zu optimieren.

Durch das Modellieren aller relevanten Teile des interferometrischen Instruments konnten die kritischen Parameter identifiziert werden. Um ein möglichst realistisches Modell zu erhalten, mussten verschiedene Messungen am Teleskop und an Teilen des LINC-NIRVANA Instruments durchgeführt werden. Simulationen der Atmosphäre komplettierten das Modell.

Verschiedene Ansätze zur Verbesserung der Leistung des Instruments wurden erarbeitet. Die Bestimmung des Gangunterschieds aufgrund von atmosphärischen und instrumentellen Effekten wurde durch eine eingehende Untersuchung der statistischen Verteilung und durch adäquates Filtern verbessert. Moderne Methoden der Regelungstechnik sorgen für Stabilität und ein optimiertes dynamisches Verhalten des Systems.

Da sich beide Teile dieser Arbeit mit den Auswirkungen der Atmosphäre auf Beobachtungen mit astronomischen Instrumenten beschäftigen, liefert das erste Kapitel einen Überblick über die grundlegenden Prinzipien und Techniken. In Kapitel 2 wird das Modell und die Analyse der Regelung des Fringe Trackers für das LINC-NIRVANA Instrument vorgestellt. Eine Simulation in Software und erste Experimente im Labor werden beschrieben. Kapitel 3 umfasst eine kurze Einführung in die Theorien der Sternentstehung und zeigt noch ungelöste Fragen auf. Es folgt eine genaue Beschreibung der polarimetrischen Beobachtungen von Proto-Sternen des Orion in Kapitel 4. Einige Konzepte und atmosphärische Effekte werden diskutiert, die in Kapitel 1 eingeführt wurden. Viel versprechende Befunde einer der Quellen führten zur ausgiebigen Modellierung und Analyse der polarimetrischen Eigenschaften von Proto-Sternen und der Entwicklung neuartiger Analysetechniken. Diese werden in Kapitel 5 präsentiert. Im letzten Kapitel werden diese Methoden schließlich auf die Beobachtungsdaten angewendet und die Resultate mit vorigen Untersuchungen in der Literatur verglichen.

Contents

High-resolution NIR imaging

1.1 Introduction

The quest for new insights in astronomy is strongly connected with efforts to achieve higher spatial resolution and sensitivity of the light-collecting instruments. A simple approach to overcome observational problems seems to be the usage of larger telescope apertures, as the size of the telescope directly affects the performance of these parameters. In practice there are a number of new problems arising with this approach. In the case of space telescopes the limitations are evident. For ground-based telescopes, besides the exploding costs of giant mirrors and support structures, the first obstacle to overcome is the limitation of the effective resolution, the atmospheric *seeing*. The principle of correcting the atmospheric turbulence distortion of astronomical images was already proposed by Babcock (1953), but a realization of the technique was not possible until recent technology provided enough computing power and precision for this task.

1.2 Observing through the atmosphere

1.2.1 Atmospheric windows

In astronomy the IR spectrum is divided into the far-infrared (FIR) regime, including wavelengths between $40\mu m$ and $300\mu m$, the mid-infrared (MID, 4–$40\mu m$) and the near-infrared (NIR, $\sim$0.7–$4\mu m$)[1]. Wavelengths shorter than microwaves but beyond the FIR are referred to as sub-millimeter. These regimes are subdivided into wavelength bands nominated with letters. The bands refer to spectral windows, at which the Earth's atmosphere is transparent (Fig. 1.2). The band names are listed in table 1.1.

The central wavelength and the bandwidth of the individual band filters is varying. Several photometric systems exist which result in slightly different photometric classifications of the apparent magnitude of sources.

---

[1]The actual wavelength ranges vary in the literature.
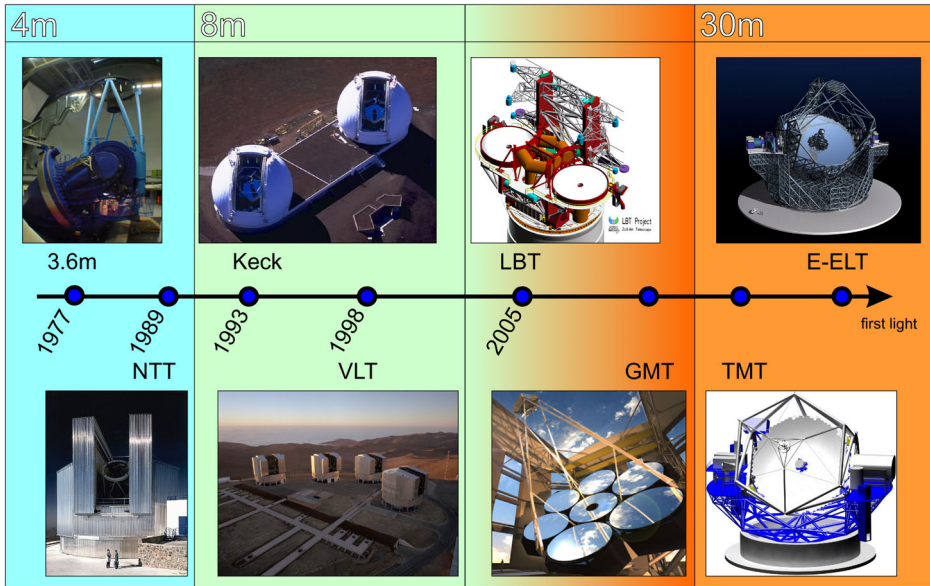
Figure 1.1: *Selected telescopes from the classes 4m and 8m and future telescopes of the 30m-class. On a sketched timeline the years of first light are denoted. For the future telescopes the dates are unclear, as road-maps are frequently shifted. The LBT is the first operating telescope of an intermediate class, in which 8m mirrors are combined to increase the light-gathering area and spatial resolution.*
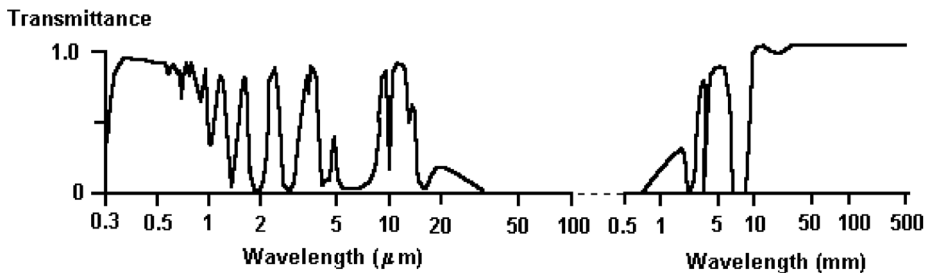
Figure 1.2: *Spectral transmittance of the Earth's atmosphere. There are few windows in the IR that allow the observation of extraterrestric radiation from the ground.*

Table 1.1: *IR bands and central wavelengths*

Band	Wavelength [μm]	Band	Wavelength [μm]
U	0.36	H	1.65
B	0.44	K	2.20
V	0.55	L	3.50
R_C	0.64	L'	3.80
R_J	0.70	M	4.80
I_C	0.79		8.40
I_J	0.90	N	10.6
J	1.25	Q	21.0

1.2.2 Turbulence

Before it travels through the atmosphere a wavefront coming from a distant source is virtually flat. The gas density in the atmosphere is varying due to temperature and pressure inhomogeneities and with it the refraction index n (Cox 1999)

$$n - 1 \approx 7.76 \cdot 10^{-5} \frac{p}{T} \; . \tag{1.1}$$

The fluctuation of the refractive index causes a time variable corrugation of the phase front. It is considered to be dominated by the temperature distribution, the influence of pressure variations is negligible. In the atmosphere areas with constant n form turbulent eddies, which occur over a wide range of spatial scales.

A statistical model of these fluctuations was formulated by Kolmogorov (1961), which considers pressure, temperature and density in the atmosphere and the variation of wind velocities and directions. The assumption is, that the kinetic energy is induced as large-scale motion in the system and then is propagated to smaller scales in the turbulent flow. The dimensions are limited to the outer scale length L_0 for large eddies and the inner scale l_0. For scales $l < l_0$ the energy is dissipated to heat. The spatial power-spectral density (PSD) $\Psi_n^K(\vec{\kappa})$ characterizes the distribution of the size and number of turbulent eddies in the atmosphere, $\vec{\kappa}$ being the spatial wave number vector ($\kappa = \frac{2\pi}{l}$, $\frac{2\pi}{L_0} \leq \kappa \leq \frac{2\pi}{l_0}$)

$$\Psi_n^K(\vec{\kappa}) = 0.033 C_n^2 \kappa^{-\frac{11}{3}} \; . \tag{1.2}$$

C_n^2 is the structure function of the refractive index and considers different atmospheric conditions. The unconvenient limitation to the range between l_0 and L_o

3

is solved with the introduction of the von Karman modification

$$\Psi_n^v(\vec{\kappa}) = \frac{0.033 C_n^2}{\left(\kappa^2 + \kappa_0^2\right)^{\frac{11}{6}}} \cdot \exp\left[-\frac{\kappa^2}{\kappa_m^2}\right] \tag{1.3}$$

with $\kappa_0 = \frac{2\pi}{L_0}$ and $\kappa_m = \frac{5.92}{l_0}$. It is easily seen, that $\Psi_n^v \rightarrow \Psi_n^K$ for $L_0 \rightarrow \infty$ and low wave numbers κ.

The values for L_0 vary for different observation sites and range from several m to more than 100m. At the ground, l_0 is typically less than 10mm. The slope of $-\frac{11}{3}$ for Ψ_n shows that the most powerful aberrations are concentrated at low spatial frequencies. The effective limit of the power spectrum is, therefore, given by the actual value of L_0, which significantly influences the overall performance of large-aperture telescopes.

1.2.3   Wavefront aberration

The phase difference of two points of the incident wavefront can be described with the refractive index structure function $D_n(\vec{r})$. It is defined as the variance of the refractive index at any points $\vec{r_0}$ and $\vec{r_1}$

$$D_n(\vec{r}) = \left\langle \left| n(\vec{r_0} + \vec{r_1}) - n(\vec{r_0}) \right|^2 \right\rangle \ . \tag{1.4}$$

If Kolmogorov statistics is applied it can be shown that under the zenith angle ζ the phase structure function is (Fried 1966)

$$D_\phi(\vec{r}) = 2.91 \left(\frac{2\pi}{\lambda}\right)^2 \sec(\zeta) r^{\frac{5}{3}} \int\limits_0^\infty C_n^2(h) dh \ . \tag{1.5}$$

$C_n^2(h)$ is dependent on the altitude since the turbulence strength varies between different atmospheric layers. The most dominating layer is commonly the ground layer, i.e. the first kilometers above the ground. $C_n^2(h)$-profiles characterize the quality of telescope sites and are, therefore, measured over a long period before the telescope is built at that place. Since strongly varying over the year due to seasonal changes of conditions, as well as during a night and maybe due to abnormal weather conditions, the profiles have to be averaged over several years to be representative for the site. Monitoring instruments are currently installed and tested at many telescopes to be able to measure the vertical turbulence profiles $C_n^2(h)$ and wind velocities $v(h)$ during an observation (Avila et al. 2001). A suitable and commonly used technique is SCIDAR, based on the analysis of scintillation images obtained from a binary star (Caccia et al. 1987; Fuchs et al. 1998).

1.2.4 Seeing and anisoplanatism

The isoplanatic angle defines the largest angular separation of two sources, so that the phase decorrelation is less than 1 rad^2. The standard definition of the isoplanatic angle for a characteristic turbulence altitude $\bar{h}$ is

$$\theta_0 = 0.31\frac{r_0}{\bar{h}} \tag{1.6}$$

with r_0 the Fried parameter or the atmospheric coherence radius (Fried 1965). The Fried parameter can be interpreted in two ways: r_0 corresponds to the circular aperture over which the phase root mean square is 1 rad. It also represents the diameter of the diffraction limited telescope with a resolution identical to the seeing disk size (cf. Eqn. 1.15)

$$\theta_{\text{seeing}} \approx \frac{\lambda}{r_0} \; . \tag{1.7}$$

The seeing is commonly denoted for the wavelength in V-band (Tab. 1.1). r_0 can be expressed in terms of the atmospheric turbulence profile $C_n^2(h)$ and the zenith angle ζ

$$r_0 = \left(0.423k^2 \sec(\zeta) \int C_n^2(h)dh\right)^{-\frac{3}{5}} \; . \tag{1.8}$$

The site specific isoplanatic angle is then defined as (Hardy 1998)

$$\theta_0 = 0.057\lambda^{6/5}\left(\sec(\zeta) \int C_n^2(h) \cdot h^{5/3}dh\right)^{-3/5} \; . \tag{1.9}$$

Observing at higher wavelength thus involves increased isoplanatic angles. A typical value for θ_0 in K band is ~ 20". Combining equations 1.8 and 1.5 gives

$$D_\phi(\vec{r}) = 6.88\left(\frac{r}{r_o}\right)^{\frac{5}{3}} \tag{1.10}$$

and in the case of an interferometer with baseline $r = B$ the standard deviation σ_{OPD} of optical path difference (OPD) with $\sigma_{\text{OPD}}^2 = \frac{\lambda}{2\pi}D_\phi$ follows

$$\sigma_{\text{OPD}} = 2.62\frac{\lambda}{2\pi}\left(\frac{B}{r_o}\right)^{\frac{5}{6}} \; . \tag{1.11}$$

1.2.5 Temporal correlation

The temporal evolution of atmospheric turbulence is discussed using Taylor's frozen-flow hypothesis. The variation of refractive indices can be neglected on a short time scale as only the translation of the atmospheric layer over the telescope aperture due to the corresponding wind speed is considered. The time scale is called the atmospheric coherence time

$$\tau_0 = 0.314 \frac{r_o}{\bar{v}} \tag{1.12}$$

with the average wind velocity $\bar{v}$, weighted by the C_n^2 of the individual layers. In the case of an interferometer with large baseline $B \gg L_0$ the phase patterns over the two apertures are uncorrelated on small time scales. The differential piston time is therefore (Kellerer & Tokovinin 2007)

$$t_0 = 2^{-\frac{3}{5}} \tau_0 = 0.66 \tau_0 \; . \tag{1.13}$$

In the case of large apertures D of several Fried cells r_0 phase variations are averaged over the aperture to some extent, leading to the modified time constant

$$t_1 = 0.273 \left(\frac{r_0}{\bar{v}} \right) \left(\frac{D}{r_0} \right)^{\frac{1}{6}} \; . \tag{1.14}$$

1.3 Telescope performance

1.3.1 Diffraction limit

The angular resolution of a circular optical system is under ideal circumstances

$$\alpha = 1.22 \frac{\lambda}{D} \; , \tag{1.15}$$

i.e. the angular distance from the first Airy minimum to the center. The Airy function is the point spread function (PSF) of the ideal telescope with circular aperture D

$$
\begin{aligned}
P_0(\vec{a}) &= \frac{\pi D^2}{4\lambda^2} \left[\frac{2 J_1(\xi)}{\xi} \right]^2 \\
\xi &= \frac{\pi D |\vec{a}|}{\lambda}
\end{aligned}
\tag{1.16}
$$

with $P_0(\vec{a})$ being the light intensity in the focal plane as a function of angular coordinate $\vec{a}$ and J_1 being the Bessel function.

For example at a 3.6m telescope the diffraction limit is, therefore, 88 mas for the central wavelength $\lambda = 1.253\mu m$ in J-band. In reality the resolution is seeing limited, because the aperture of this telescope is much larger than a single Fried cell r_0 at the given wavelength. The emerging flat wavefront from a distant source is distorted in the atmosphere due to the varying refractive indices.

1.3.2 Strehl ratio

The influence of the aberrations on astronomical images can conveniently be described in the Fourier domain. An obtained image $I(\vec{R})$ in the focal plane will be the convolution ($\otimes$) of the brightness distribution $I_0(\vec{r})$ on the sky and the PSF

$$I(\vec{R}) = I_0(\vec{r}) \otimes \text{PSF} . \tag{1.17}$$

The Fourier transformation of the PSF is called the optical transfer function (OTF)

$$\mathcal{F}\{\text{PSF}\} = \text{OTF} . \tag{1.18}$$

Hence, the OTF is expressed in the spatial frequency domain. The effective OTF consists both of the OTF_T of the telescope and the atmospheric OTF_A. According to the convolution theorem the convolution of the corresponding PSFs is the product of the OTFs

$$\text{OTF} = \text{OTF}_T \cdot \text{OTF}_A . \tag{1.19}$$

A measurement for the optic performance is the Strehl ratio, defined as the ratio of the peak intensity of the observed PSF to the peak intensity of the theoretical diffraction limited PSF_T

$$S = \frac{\max(\text{PSF})}{\max(\text{PSF}_T)} . \tag{1.20}$$

It describes which fraction of observed light is spread into the seeing limited halo and which is concentrated in the diffraction limited core. A higher Strehl produces therefore sharper images. Under seeing limited observation conditions the Strehl ratio is typically under one percent in K-band. With Adaptive Optics this can be increased up to $\approx 70\%$

1.3.3 Adaptive optics

Since the very first use of telescopes by Galileo in 1609 astronomers have to deal with the turbulent air. Today all main observation sites are located on high mountains preferably in desert areas with low humidity and far away from cities with

a lot of (light) pollution. Of great importance for a good site are also the weather conditions including many clear nights with no clouds covering the line of sight and moderate wind and temperature variations. Despite the careful choice of the site the atmospheric effects are limiting the performance of ground-based telescopes, which exceed the aperture size of about 0.6m in the NIR (cf. Sect. 1.2.4). There are several approaches to obtain or come close to the theoretical resolving power:

- *Space Telescopes* The advantage of totally avoiding atmospheric turbulence and the restriction of atmospheric windows (Fig. 1.2) is faced by the extremely high costs and limits of the achievable mirror diameters.

- *Speckle interferometry* If the exposure time is short compared to τ_0 (Eqn. 1.12) the atmospheric perturbation can be assumed to be frozen. As a result, the short-exposure images contain bright spots – the so-called speckles – of a number $\sim (D/r_0)^2$. The high-resolution image can be obtained by simple "shift and add" operations on the single frames. Since each exposure is affected by the read-out noise of the detector, the sensitivity that is achievable with this method is limited.

- *Adaptive Optics (AO)* The distorted wavefront from a point-source is measured with a wavefront sensor (WFS) and compensated by deformable mirrors (DM). A suitable reference star has to be located within the isoplanatic angle. As a result the sky-coverage of an AO instrument (the part of the sky that is actually observable) depends on the size of the isoplanatic angle. Only science targets which have a sufficiently bright (typically < 14 mag in V-band) point source nearby benefit from the correction. The sky-coverage of a classical AO system is, therefore, only ~1%. Currently there are efforts to increase the isoplanatic angle by using several guide stars as described in chapter 1.5.1. The restriction of available natural guide stars can be reduced with the technique of producing an artificial laser guide star (LGS) at an altitude of about 90 km by a Natrium laser.

There are different ways to describe, identify and compensate the wavefront aberrations in an AO system. The zonal approach splits the telescope pupil into cells of a regular grid and evaluates the distorted wavefront as deviations from the mean value at the central points (Fried 1977). The modal approach defines a appropriate base for the description of the instantaneous wavefront $\psi(r, \phi)$

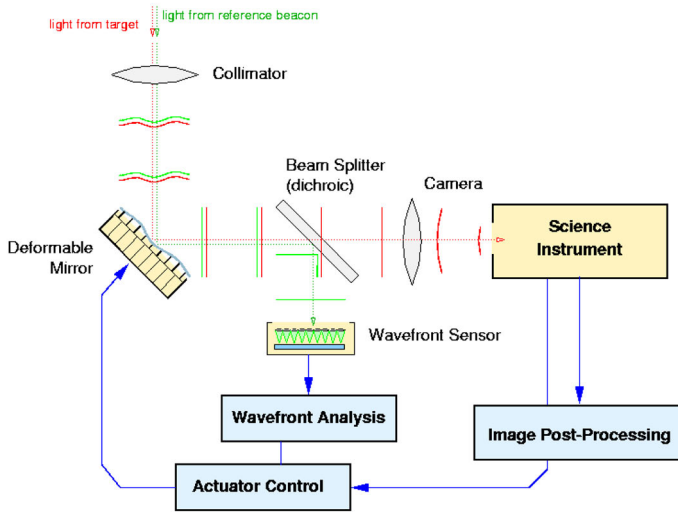$$\psi(r, \phi) = \sum_J a_j Z_J(r, \phi) \ . \tag{1.21}$$

Figure 1.3: *Scheme of an adaptive optics system (image credit: CfAO)*

Any aberrations can be composed by Zernike modes (Noll 1976)

$$
\left.
\begin{aligned}
Z_{J\,\text{even}}(r,\phi) &= \sqrt{n+1}R_n^m(r)\sqrt{2}\cos m\theta \\
Z_{J\,\text{odd}}(r,\phi) &= \sqrt{n+1}R_n^m(r)\sqrt{2}\sin m\theta
\end{aligned}
\right\} \quad m \neq 0
$$
$$
Z_J(r,\phi) = \sqrt{n+1}R_n^0(r) \qquad\qquad m = 0
\tag{1.22}
$$

where

$$
R_n^m(r) = \sum_{s=0}^{\frac{n-m}{2}} (-1)^s \frac{(n-s)!}{s!\left(\frac{n+m}{2}-s\right)!\left(\frac{n-m}{2}-s\right)!} r^{n-2s} .
\tag{1.23}
$$

n is the radial order and m the azimuthal order, n and m have to fulfill $m \leq n$, $n - |m| =$ even. The first 28 modes and the corresponding aberration names are shown in figure 1.4.

Considering the Kolmogorov PSD (Eqn. 1.2) the aberations are most powerful for low spatial frequencies, so it is possible to achieve a good Strehl ratio even with a low number of corrected Zernike modes. Correcting only the first J modes results in a residual variance of (Noll 1976)

$$
\sigma_\psi^2 \approx 0.2944 J^{-\frac{\sqrt{3}}{2}} \left(\frac{D}{r_0}\right)^{\frac{5}{3}} .
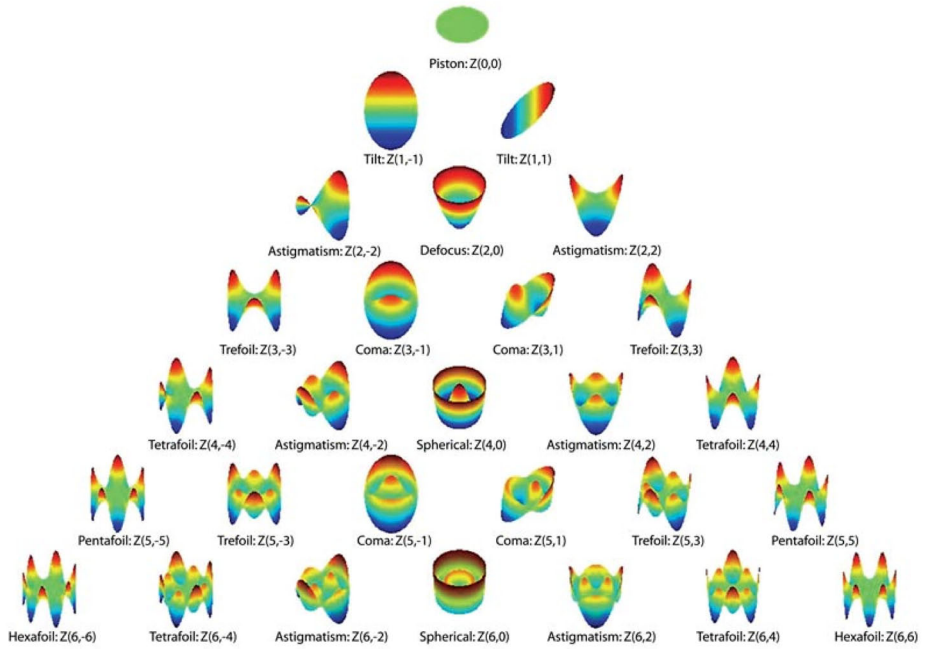\tag{1.24}
$$

Figure 1.4: *Zernike modes and corresponding optic aberration (image credit: Shaw-McMinn 2006).*
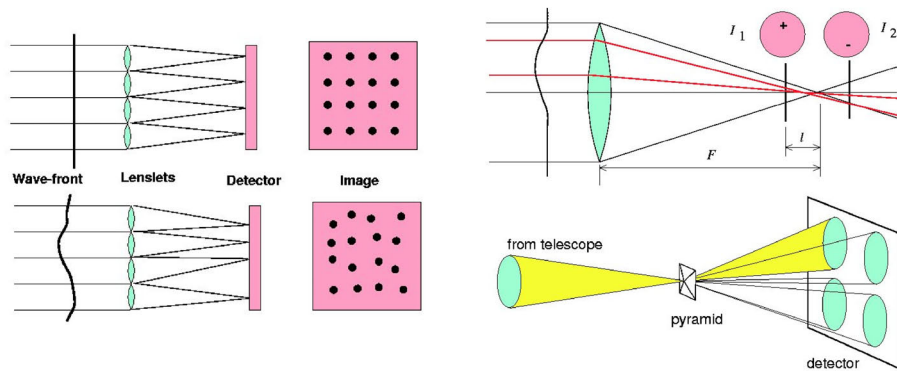

Figure 1.5: *Types of wavefront sensors. Left: Shack-Hartmann sensor with lenslet array. Right: Curvature sensor (top) and pyramid sensor (bottom, image credit: CTIO/NOAO).*

The correction of the wavefront is accomplished with a deformable mirror, consisting of a thin glass shell attached on a reference plate with piezo-electric actuators in between. The surface can be shaped according to control voltages applied to the actuators (Fig. 1.3). The number of actuators should correspond to the number of Fried cells across the aperture $N \approx \left(\frac{D}{r_0}\right)^2$. The DM is commonly supplemented by an actuated flat mirror, which compensates the tip-tilt modes only.

For the measurement of the incident wavefront several techniques are available. Most AO systems are operated with a Shack-Hartmann sensor (Fig. 1.5). It is composed by a grid of micro lenses, a so-called lenslet array. The wavefront is split into a corresponding grid of sub-apertures, each generating an image in the focal plane, which is slightly shifted due to the local tip and tilt of the wavefront. This corresponds to the first derivative of the wavefront and allows the reconstruction of the whole incident wavefront.

The curvature WFS is simpler as it measures the image at two locations, one before focus (intra-focal image) and the other outside the focus (extrafocal image). The intensity distributions of the images correspond to the wavefront curvature, i.e. the second derivative.

The principle of the pyramid WFS is to split the light into four beams and comparing the intensities of corresponding pixels of the four pupil images on the CCD (Fig. 1.5). The differential illumination is proportional to the first derivative of the wavefront. Advantages of this technique include a higher sensitivity and a better performance at the correction of low-order Zernike modes (Ragazzoni & Farinato 1999).

1.4   The Large Binocular Telescope

The Large Binocular Telescope (LBT) forms a bridge from current 8–10m class telescopes to future giant telescopes technology (Fig. 1.1). Located on Mt. Graham in Arizona at an altitude of about 3200 m, it has seen first light in 2005 (Hill et al. 2006). The LBT consists of two 8.4 m telescopes on a common altitude-azimuth mount, separated by 14.4 m (center to center). The two channels are symmetrical and each will be equipped with independent adaptive optics systems. The light-gathering power of the two mirrors corresponds to a single 11.8 m telescope and, when operated in interferometric mode, the resolving power along the baseline is comparable to that of a 22.8 m telescope. The full resolution in all directions can be achieved by consecutive observations of a target at three different parallactic angles at least, separated by 60° ideally.

The new concept of the single mount has advantages over existing interfer-

Figure 1.6: *The Large Binocular Telescope in September 2007: The two primary mirrors and prime focus cameras are installed. The other mirrors and some swing arms are still missing. (image credit: David Harvey)*

ometers with 8m-class mirrors, such as the Keck interferometer or the VLTI (cf. Fig 1.1). For the coherent combination of beams from two separated telescopes complex, time-varying delay lines are necessary. The entrance pupil geometry of the two LBT arms is independent of the pointing of the telescope, and therefore constant over observation time, so no delay line is needed. The main advantage of the fixed entrance pupil geometry is the ability to realize a so called homothetic imager or Fizeau interferometer (cf. Fig. 1.8). This special interferometer setup allows for a much larger field of view (FoV) than existing stellar interferometers.

The LBT is designed to be used in a versatile manner. The telescope provides 12 focal stations, where instruments can be operated: two wide-field cameras (LBC red and blue) are located at the prime foci, mounted on swing arms or so-called spiders. The secondary and the tertiary mirrors are also mounted on spiders, which allows a flexible configuration of the instruments used.

This flexible design of the telescope introduces some new problems, though: Besides the complexity due to the increased number of degrees of freedom, actuators and calibration issues, the support structure and the spiders in special are unique for such a system. Although they are designed to an optimum in stiffness at light-weight, the vibrational behavior as well as the flexure under varying elevation of the telescope is not known.
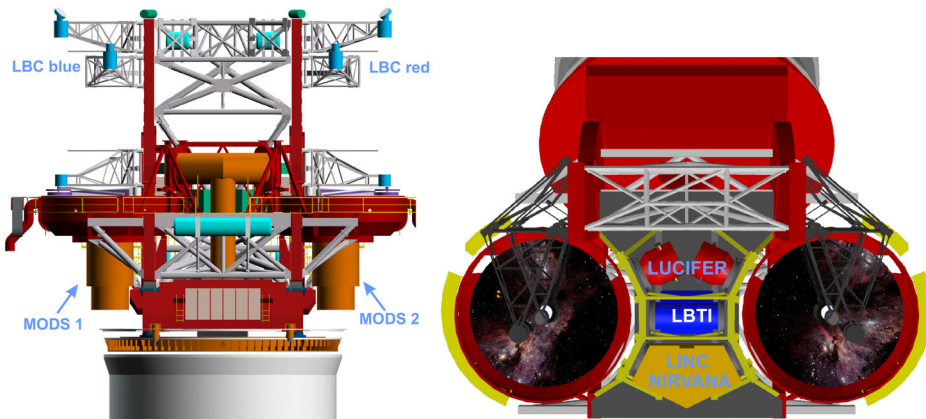
Figure 1.7: *Overview of the instruments to be installed at the LBT. There are 6 single-eye cameras and two interferometric cameras. LBTI will provide imaging and nulling interferometry at longer wavelength. LINC-NIRVANA is a NIR homothetic imager with large FoV. The PEPSI spectrograph and polarimeter is not shown, as it is a fibre-fed instrument.*
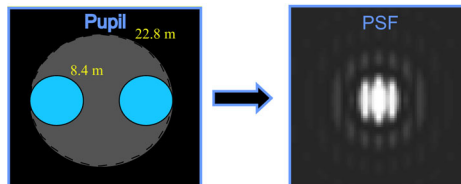

Figure 1.8: *The entrance pupil of the homothetic imager LINC-NIRVANA can be represented by a mask of two separated pupils over a large single 22.8 m aperture telescope, the so-called Fizeau-mode. The exit pupil is a scaled-down version of the entrance pupil, the case of two separated apertures is called homothetic imaging. The resulting PSF is then constant over the whole FoV.*

1.5 LINC-NIRVANA

LINC-NIRVANA (Herbst et al. 2004), the NIR interferometric imaging camera for the LBT incorporates all advantages provided by the LBT design. Because it obeys specific geometric constraints that constitute a Fizeau interferometer, LINC-NIRVANA can profit from the resulting large FoV in two ways: It allows for a virtually unlimited interferometric science FoV (limited by the cost of NIR focal plane arrays). And it allows to exploit the FoV to choose from a large pool of off-axis reference stars for fringe tracking (cf. Sect. 1.5.2). In its final expansion stage, LINC-NIRVANA (Fig. 1.9) will be equipped with a multi-conjugate adaptive optics system (MCAO) that can gather the light of reference stars in a 6 arcminute diameter field. In terms of angular resolution LINC-NIRVANA will outperform the imaging capabilities of exiting 8–10 m class telescopes by a
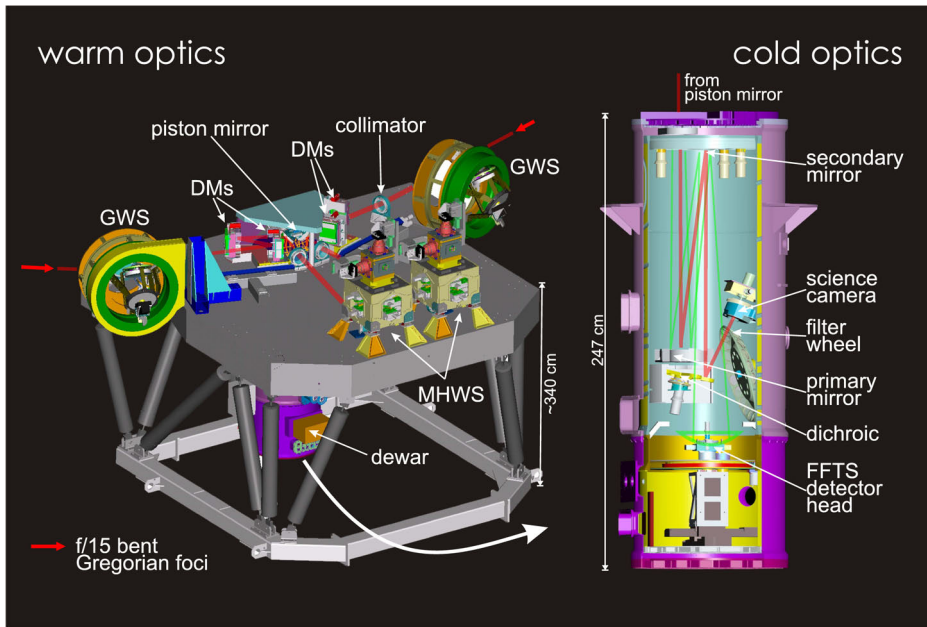
Figure 1.9: *LINC-NIRVANA will be installed in one of the interferometric focal stations of the LBT. The two beams of the interferometer will be combined by a Cassegrain telescope within the dewar of LINC-NIRVANA. The fringe tracker is located at the bottom end of the dewar (Laun et al. 2006) close to the science detector. A set of dichroic beam splitters will reflect part of the NIR spectrum in the center of the science FoV to the science detector. The remaining NIR radiation in the center is transmitted to the fringe tracker. In the FoV exceeding the central 10 arcsec covered by the science detector, the full NIR spectrum is available to the fringe tracker.*

factor of ~3.

The pioneering instrument includes a fringe tracking device, which is mandatory for the high-resolution interferometric imaging mode. A dedicated actuated mirror (Fig. 1.10) allows for correction of optical path difference (OPD) of the two arms before the beam combination according to the obtained piston information from the fringe tracker.

1.5.1 MCAO

Classical AO systems use a single star for wavefront correction. The deformations of the wavefront due to atmospheric turbulence are corrected also with a single actuator, the deformable mirror (DM). A brief description of the principle of an AO system is given in section 1.3.3. LINC-NIRVANA will be equipped
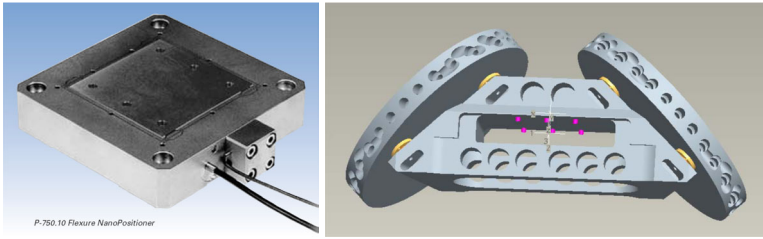
Figure 1.10: *The piezo-driven actuator (left) is mounted in the center of gravity of the piston mirror (right). The design of the frame shows high stiffness and minimum weight, resulting in optimized dynamics of the system. Rohloff (2005)*

as one of the first scientific instruments with a Multi-Conjugate Adaptive Optics system (MCAO).

The atmospheric variations are monitored for different atmospheric layers and the corresponding correction is introduced with different DMs. Foreseen are two independent wavefront sensors (Fig. 1.9) conjugated to different atmospheric layers, the ground-layer wavefront sensor (GWS) and the mid/high-layer wavefront sensor (MHWS) each equipped with pyramids (cf. Sect. 1.3.3). The adaptive secondary mirrors on the swing-arms are used to correct the most turbulent ground-layer aberrations, whereas additional DMs are located on the optical bench for the correction of higher-altitude aberrations. Several pyramids per WFS (12 and 8 respectively) allow to combine the light of multiple reference stars, which is beneficial for the wavefront reconstruction, the homogeneity and size of the corrected FoV and therefore the sky coverage (Arcidiacono 2005).

The performance of the AO-system is of substantial importance for the interferometric results. Metrology and analysis for the Mt. Graham atmospheric conditions can be found in Egner et al. (2007) and Egner (2006). The MCAO systems work independent for both arms of the interferometer, so that the wavefronts are corrected as good as possible, but a piston remains in general in between (cf. Sect. 1.2.4).

1.5.2 FFTS

The Fringe and Flexure Tracking System (FFTS) is an integral part of LINC-NIRVANA. Its purpose is the real-time detection and compensation of differential piston between the two interferometric channels and the correction of misalignment due to instrumental flexure. The interference of the two wavefronts on the detector has to be kept at a fixed phase relation – ideally with zero OPD (cf.
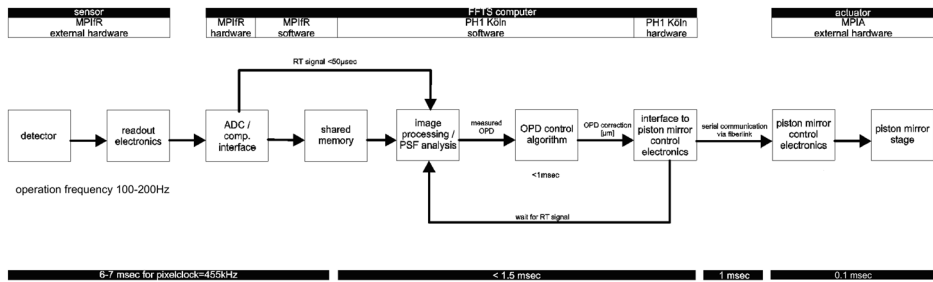
Figure 1.11: *The FFTS control loop and latencies. The control signal is distorted by a low sampling rate (∼100–200 Hz), high latency (>6 ms) and high noise (Bertram et al. 2006). This is compensated in the OPD (optical path difference) control algorithm to some extend. The actuator, i.e. the piezo stage and piston mirror, is driven in closed-loop and limited by the system dynamics. Also indicated are the different institutes contributing to the FFTS and LINC-NIRVANA instrument.*

Eqn. 1.11) – during an exposure, otherwise the advantages in spatial resolution of the interferometer are lost, since the fringes are blurred. A more comprehensive view on the FFTS can be found in Straubmeier et al. (2006) and Bertram (2007a).

The fringe pattern according to the PSF of the special aperture of the LBT (Fig. 1.8) is monitored with the FFTS detector. If OPD occurs between the two arms of the interferometer, the fringes in the pattern will move accordingly and the fringe contrast will decrease until the coherent length is reached and no fringes are visible any more. This allows the determination of the actual OPD by appropriate analysis of the pattern. The science detector will "see" the same fringe pattern and contrast, so it is important to constantly correct for the OPD to obtain science images with a maximum of fringe contrast and the full spatial resolution by applying sophisticated deconvolution techniques (La Camera et al. 2007).

Both the LINC-NIRVANA science and the FFTS detector are HAWAII focal plane arrays (FPA) from manufacturer Teledyne (Fig. 1.12). While the HAWAII-2 FPA with a resolution of 2048×2048 pixels is used as the science detector, only a single quadrant (512×512 pixels) of the HAWAII-1 is needed for the FFTS. The acquired PSF images will actually be reduced in size to a minimum sub-window (∼ 32×32 pixels) to increase the achievable frame rate. The photovoltaic semiconductor mercury cadmium telluride ($HgCdTe$) is a common material for the detection of near- to mid-infrared light (∼1 –12 μm), due to its adjustable bandgap. By the ratio of $CdTe$ to $HgTe$ in the composition any bandgap be-
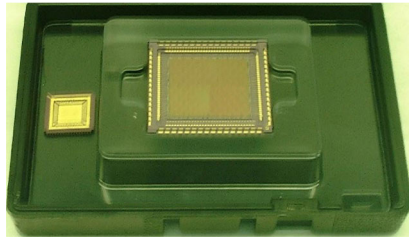
Figure 1.12: *The Rockwell Scientific HAWAII-1 FPA (focal plane array) is used as the FFTS detector. Here the HAWAII-2 –which is used as the science detector– is shown in comparison to the NICMOS-3 array to the left. (image credit: IAC).*

tween 0 and 1.5 eV can be obtained. Another common material with low drift used for astronomic IR detectors is indium antimonide (*InSb*), which was the first material used widely in high-performance NIR photo diodes (Rieke 2007). The band gap of *InSb* is suitable for detection of wavelengths of up to $5\mu m$, depending on cooling conditions. For wavelength beyond $10\mu m$ *SiGa* ($< 18\mu m$) or *SiAs* ($< 25\mu m$) are used. IR detectors are operated at cryogenic temperatures ($\sim$77K) to reduce thermal noise and enhance the sensitivity. This fact is the crux of the construction design of the FFTS instrument. The detector operates in a cryogenic environment, but has also to be moved around, since the FoV rotates around the science target during an observation. One of the main advantages of the instrument is the large FoV and a large maximum angular separation between science target and fringe tracking star. As a consequence the desired traveling range for the FFTS detector is quiet large. This problem is solved with the detector positioning unit (DPU) operating at ambient temperature and shielding the science detector from thermal radiation with a moving baffle (Fig. 1.9, right). The DPU consists of off-the-shelve linear positioning stages from manufacturer *Physik Instrumente*, operating in servo mode (feedback loop) by a dedicated motor controller with PID control (cf. Sect. 2.4.5).

For the performance of the FFTS it is of great importance, that the detector is positioned in the focal plane very precisely. The location of the fringe pattern on the FPA has to be kept as fix as possible, because uncertainties affect directly the performance of the piston determination (Bertram et al. 2006). The position error must not exceed the pixel size of the detector, i.e. $\sim 18.5\mu m$ and significant higher precision is desirable.

Hence, a testbed for the DPU was designed with measurement equipment that can resolve positions of less than $1\ \mu m$. For this regime interferometric devices are best suited. A Heidenhain KGM-182 (Fig. 1.13) was used, which enabled simultaneous measurements in two dimensions by an etched 2D cross-
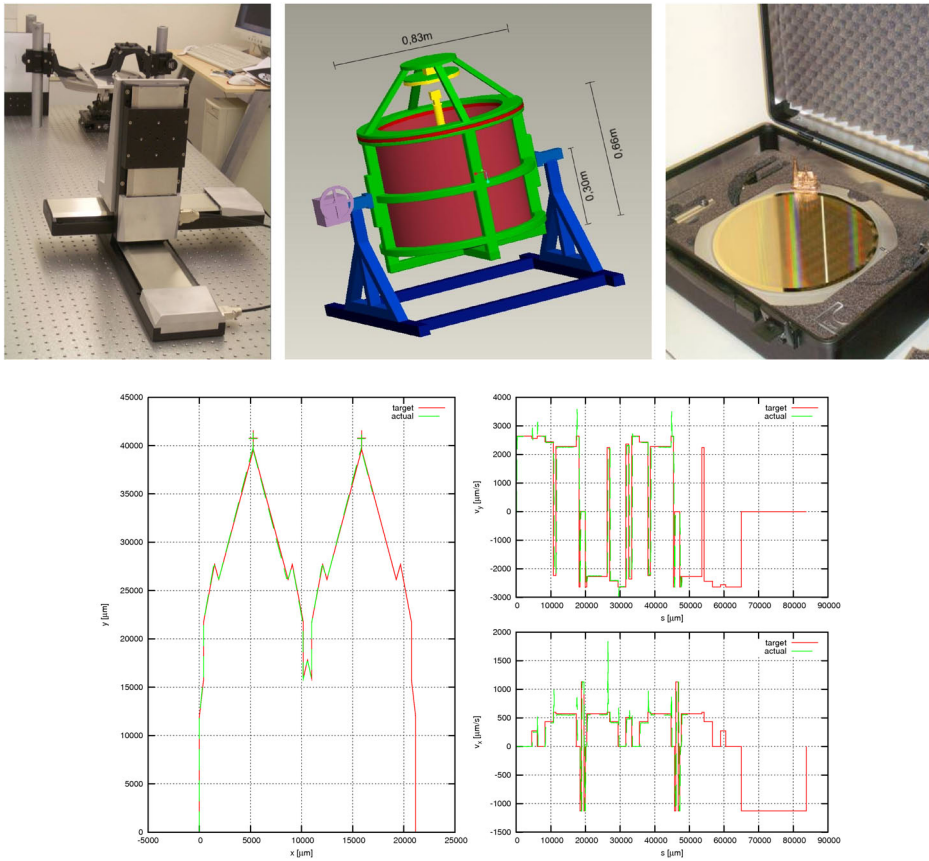
Figure 1.13: *Top: The positioning precision of the DPU (left) is measured in a testbed (middle) under arbitrary elevation with an interferometer (right). Bottom: Measurements of the DPU movement in the testbed can be obtained in 2D with arbitrary trajectories. The example shows a very snappy trajectory, this is especially useful for the optimization of the PID parameters (here strong overshooting is seen in the velocity plots to the right). The precision of the interferometric measurement is below 1 μm.*

grid titanite pattern on a glass substrate. The moving part consists of the actual interferometric head, which evaluates a signal modulated by the pattern. The pattern period is 4 μm, but since the signal measured over this length is a co-sine, the measuring step is decreased by subdivision to $\sim 1nm$ (4096-times over-sampling). The uncertainty over the measurement length of 230mm is $\sim 0.1\mu m$.

Initial tests in 2D resulted in achievable trajectories of the stages of sub-micrometer precision and repeatabilities of a few μm. However, as tests of other groups with similar devices indicate, flexure effects might reduce the perfor-mance. The advanced design of the testbed includes flexure measurements of the DPU, with a tilting mechanism of the whole fringe tracker (Fig. 1.13). Unfortu-nately, at the time of the writing of this thesis several parts of the fringe tracker were not built yet. Since the DPU flexure testbed was designed to work with the whole support structure, including the mounting plate of the linear stages as well as the detector head (or dummy weight) on a fibreglass pin (cf. Fig. 1.9), the flexure measurements are not done yet. Deviations of the positioning under specific elevation angles can be quantified very precisely with this setup and the effects could be compensated in the control software by look-up tables (LUT), assumed that the flexure deviations are repeatable.

The development of the FFTS hardware at the I. Physikalisches Institut in Cologne has reached now a mature state. First progress is made in the actual construction and manufacturing of mechanic parts. A very important part is the operating software of the system. A complex software solution is required for the the versatile preconditions (Fig. 1.14) of the fringe tracking task with a highly non-sequential work-flow. Being an interacting subsystem of LINC-NIRVANA, the FFTS software includes various interfaces, which add to the complexity of the software. Again the whole process is time-critical. In the design it was, therefore, tried to capsule as many modules as possible in independent processes and threads. A detailed description of the software details is beyond the scope of the thesis. An overview can be found in Bertram (2007b). Because the main focus in this work is on the performance of the piston control, the sequence diagram of this crucial, most time-critical part is outlined in figure 1.15.
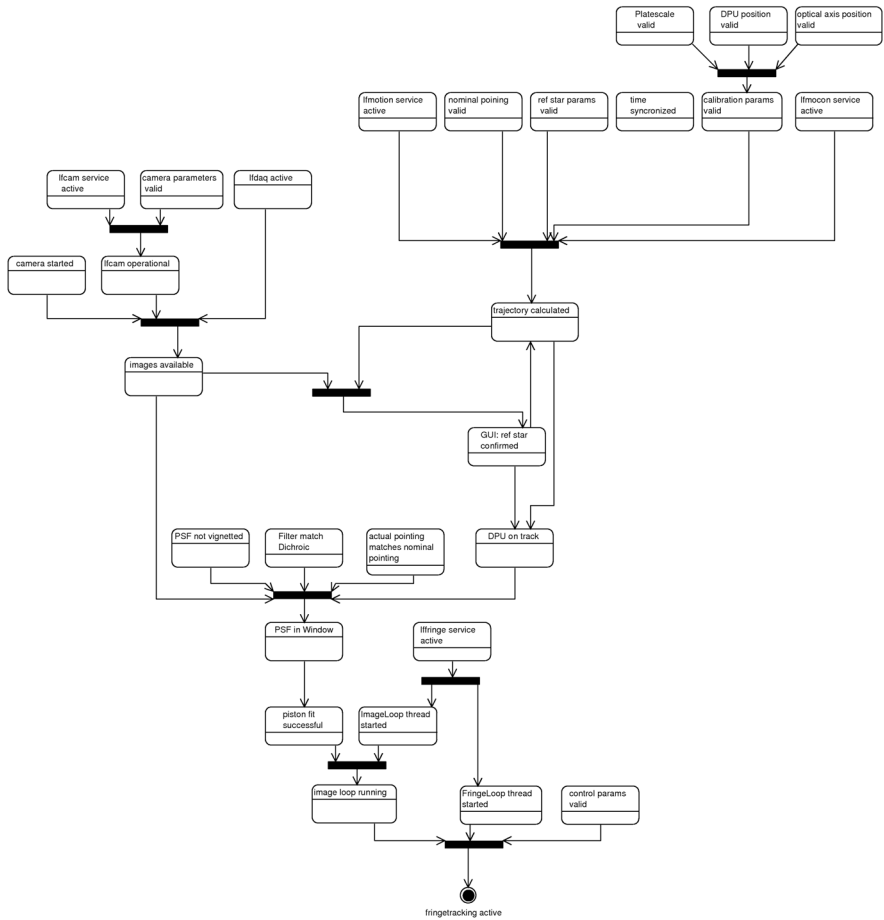
Figure 1.14: *State tree for the fringe tracking software. This except from the design of the control software emphasizes the complex states and prerequisites that are necessary for operation of the FFTS.*
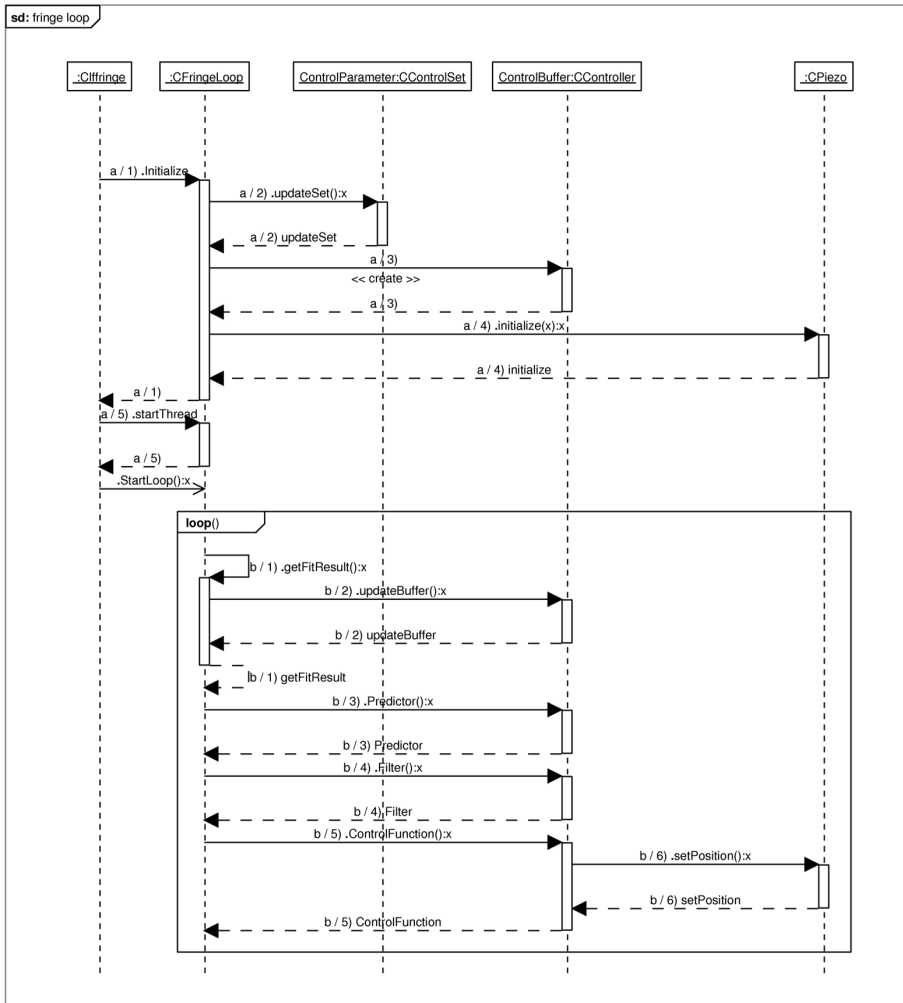
Figure 1.15: *This except from the UML model of the FFTS software module shows the critical piston control loop. It consists of a dedicated thread running at a fixed frequency for synchronous operation and stability. The interface to the image acquisition and analysis is realized with fast inter-thread communication and the piezo controller is addressed directly over the hardware interface. The whole process takes advantage of the real-time capabilities of recent Linux kernels (Wang et al. 2006).*

CHAPTER 2

Simulation of control performance

2.1 Motivation

The sky coverage of LINC-NIRVANA is closely related to the performance of the fringe tracking system (Bertram et al. 2006). A residual piston of 0.1 λ for the central wavelength of the science band is the performance goal for the FFTS. The resulting fringe contrast should then allow for highest-resolution post-processing of the scientific images. The piston performance in turn is related to many parameters, as we show in the following. Table 2.1 lists the required fringe tracking residual piston for the 0.1 λ criterion in the science band. If the FFTS operates at shorter wavelength as the science detector the limit of residual piston for the performance goal is less restrictive.

The piston error budget due to the control loop effects is analyzed with a simulation of the expected system response. The piston signal which has to be corrected for consists of the atmospheric and the instrumental piston, including vibrations of the telescope structure and flexure effects. An overview of the FFTS system and the control tasks is given in Fig. 2.1. The different aspects of the piston spectrum and the appropriate control techniques are discussed in this chapter. With a detailed model a controlling strategy and parameters can be optimized. On the other hand the limiting reference star magnitude and distance to the target can be estimated if a residual piston performance is specified.

Table 2.1: *Residual piston RMS at the fringe tracking wavelength required to achieve an RMS value of 0.1 $\lambda_{Science}$.*

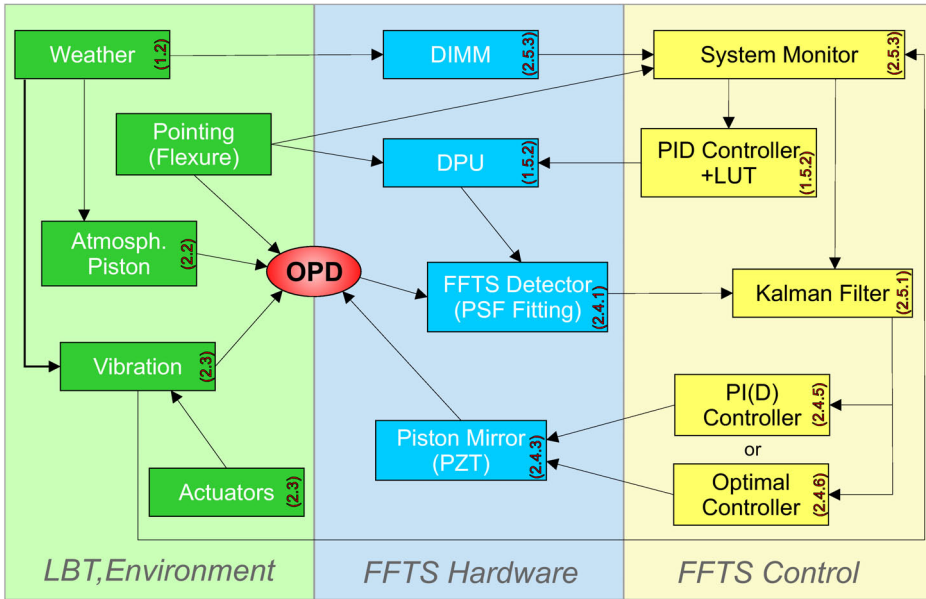|	Fringe tracking band				
λ_{Science}	J	J+H	H	H+K	K
J	0.100	0.085	0.076	0.063	0.057
H	0.132	0.112	0.100	0.083	0.075
K	0.176	0.150	0.133	0.111	0.100

Figure 2.1: *Overview of the FFTS control system. The task of the FFTS is to compensate atmospheric and instrumental piston or OPD. The actuators are the DPU for the tracking of reference stars and the piston mirror. The FFTS detector for the PSF fitting and eventually a DIMM are sensors, which provide the set points for the controllers. The noisy OPD measurement is Kalman filtered for optimal piston estimation, limited dynamics of the piston mirror actuator might impose an optimal control approach. The numbers refer to the sections in this work, in which the subjects are discussed.*

2.2 Atmospheric differential piston

The atmospheric turbulence over each aperture of one arm of the LBT is compensated with the MCAO systems independently. The tip-tilt is commonly the lowest Zernike mode that is considered in an AO system (Fig 1.4), since the piston has no influence on the quality of single aperture imaging. The residual piston inbetween the two wavefronts arriving at the LINC-NIRVANA beam combiner is mainly related to the large eddies and the outer scale L_0 in the atmospheric layers. In the model of a single-layer atmosphere following a Kolmogorov power spectrum the standard deviation of the piston is dependent on the Fried parameter r_0 only (Eqn. 1.11). The statistical distribution of the differential piston should resemble a normal distribution with standard deviation σ_{OPD} for a piston sequence of sufficient length. The temporal piston variation in turn is dependent on the actual $C_n^2(h)$ and wind profile. For an estimation of this crucial parameter numerical simulations are used.
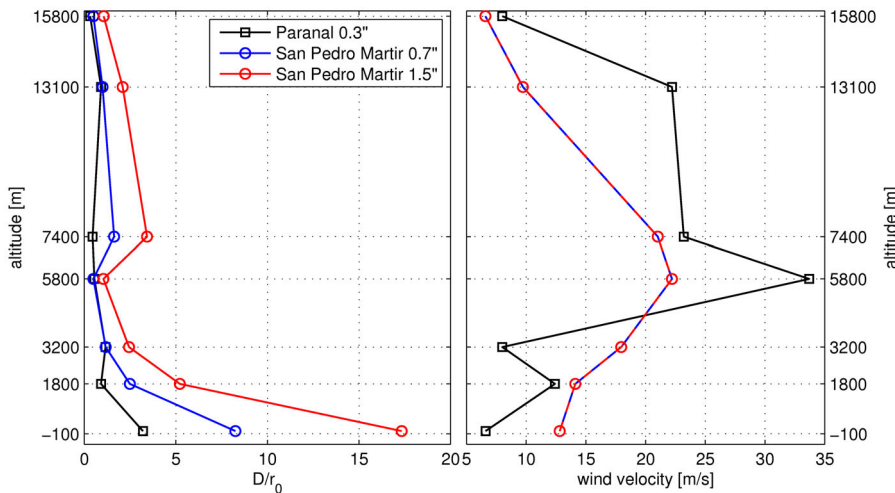
Figure 2.2: C_N^2 *altitude profiles and wind velocities for the reference seeing conditions 0.3", 0.7" and 1.5". The data was measured at the observing sites Paranal and San Pedro Martir. The original 0.7" profile was used to model a bad seeing case by appropriate scaling of the C_N^2 data.*

2.2.1 LOST

The layer-oriented simulation tool (LOST, Arcidiacono et al. 2004) is written in IDL and evaluates the response of an AO system to a simulated atmosphere, based on measured $C_n^2(h)$-profiles and wind speeds. It considers the real geometry of the telescope, the actual used wavefront sensor (cf. Sect. 1.3.3), the control loop parameters for wavefront correction and realistic noise contributions and residuals. The atmosphere is modeled with seven independent layers, characterized by $\frac{D}{r_0}$, v, h and optional L_0. The turbulence is simulated according to the von Karman/Kolmogorov model. Patterns of multiple reference stars – so-called asterisms – can be set up, which affects the performance of the multi-layer AO with ground-layer and mid-high-layer correction units (cf. Fig 1.9). The tool was successfully used to estimate the performance of the crucial parameters isoplanatic angle and isopistonic patch of LINC-NIRVANA under observation conditions (Bertram 2007a).

In the following simulations based on two atmospheric profiles are considered, namely a Paranal and a San Pedro Martir profile (Fig. 2.2). The measured Paranal data corresponds to an overall seeing of 0.7" at V-Band. This profile was scaled such that it represents an example of excellent seeing (0.3"). Cerro Paranal is an observation site (VLT) located in Chile at an altitude of 2630m,

whereas Sierra San Pedro Martir in Mexico is separated 550km from Mt. Graham with a similar altitude. To include a very bad seeing the San Pedro Martir profile was scaled up to obtain a 1.5" seeing condition. A LOST simulation is very time-consuming. Depending on the setup a simulated time sequence of 6s will take up to 2 weeks on a recent workstation with a step-size $\tau_S = 0.5ms$. This step-size is considered to be small against the turbulent time-scales t_1 (Eqn. 1.14).

2.2.2 Piston variation

Figures 2.3, 2.4 and 2.5 show the representative piston sequences. With increasing degree of atmospheric turbulence the variation of the piston signal is stronger, as expected. The expected variation between time steps of the FFTS loop is crucial for the design of the controller. Since the piston is dependent on many parameters in the atmosphere and in the MCAO setup the question arises, how the variation is statistically distributed. The atmospheric turbulent layers are generated with the Kolmogorov power spectrum (Eqn. 1.2). The number of layers and Fried cells in the apertures may cause a normal distribution regardless of the basic distribution according to the central limit theorem.

In figures 2.3–2.5 also a statistical analysis of the second derivative of the piston is shown, i.e. the acceleration. The distribution of the simulation with step-size τ_s corresponding to 2kHz has tails with greater variations, which is probably related to the underlying Kolmogorov statistics.

However, the achievable FFTS sampling rate will not exceed 200Hz. Although the reference star can be picked from a wide field of view around the science target – depending on the isopistonic patch – it is desirable to operate on reference stars that are as faint as possible. A minimum exposure time is necessary to obtain reasonable SNR and good fringe pattern fitting performance. The piston on the FFTS detector is evaluated by fitting the theoretical polychromatic fringe function to the fringe pattern with OPD as free parameter. The image is compressed along the dimension perpendicular to the baseline of the interferometer to increase the precision, but the performance of the fit depends strongly on the overall SNR of the acquired images (Bertram et al. 2006).

Down-sampling the piston signal at a rate of 100–200Hz is equivalent to a smoothing, so the variation is decreased. The down-sampled signal resembles an even closer to normal distribution in piston variation, naturally with a decreased standard deviation. In figure 2.6 to the left the change in variation or the degree of smoothing is shown. In the achievable range of the sampling rate for the FFTS the variation can assumed to be constant. The residual error which cannot be corrected for increases with lower sampling rates, as the control bandwidth is
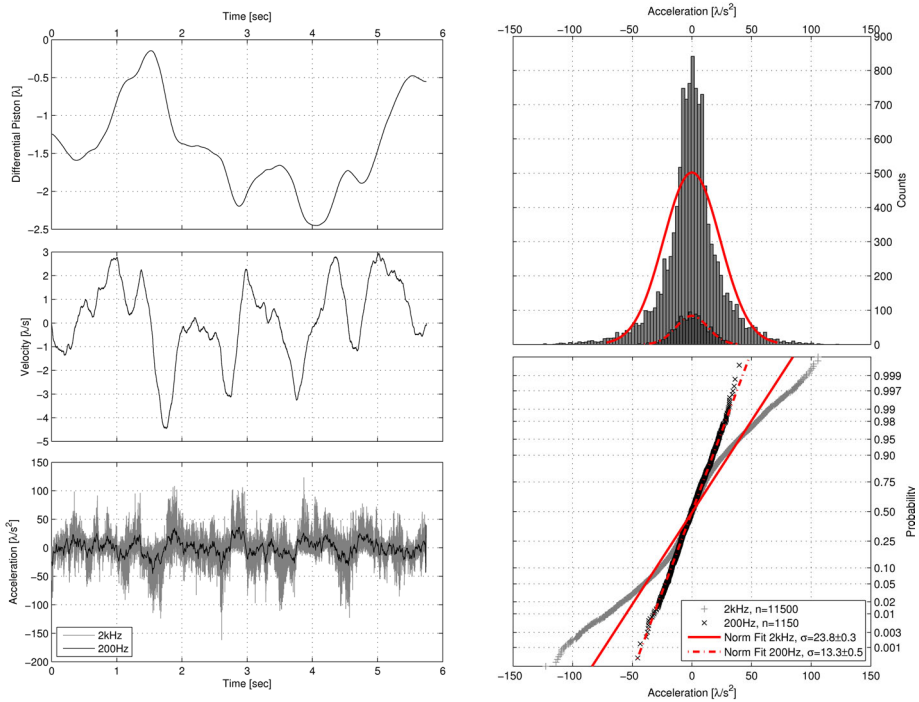
Figure 2.3: *Left: atmospheric differential piston sequence obtained from simulations of excellent seeing conditions with the Paranal 0.3"@V-band $C_N^2(h)$-profile. Shown are the total piston from atmosphere, the velocity and acceleration. The sampling time is $5 \cdot 10^{-4}s$ and $5 \cdot 10^{-3}s$ respectively. The acceleration is smoothed by the lower sampling rate. Right: The probability distribution of the variation in acceleration. To the top the histogram and fitted normal density function, to the bottom the cumulative distribution function and normal fits. The distribution differs from the normal distribution, but the deviations are small in the case of low sampling rates.*

decreased. This is shown in figure 2.6 to the right. This residual error – assuming that the piston variation obtained from the simulations at 2kHz is realistic and quasi-continuous – is an upper limit for the performance, which can be achieved with the FFTS. On the other hand there are many other aspects in the system which substantially degrade the performance. This is discussed in the following sections.

2.3 Vibration metrology at the LBT

As the quantities of vibration and flexure of the telescope directly affects the development of the LINC-NIRVANA instrument, in particular the design of the control software, it was mandatory to keep an eye on the real behavior already at
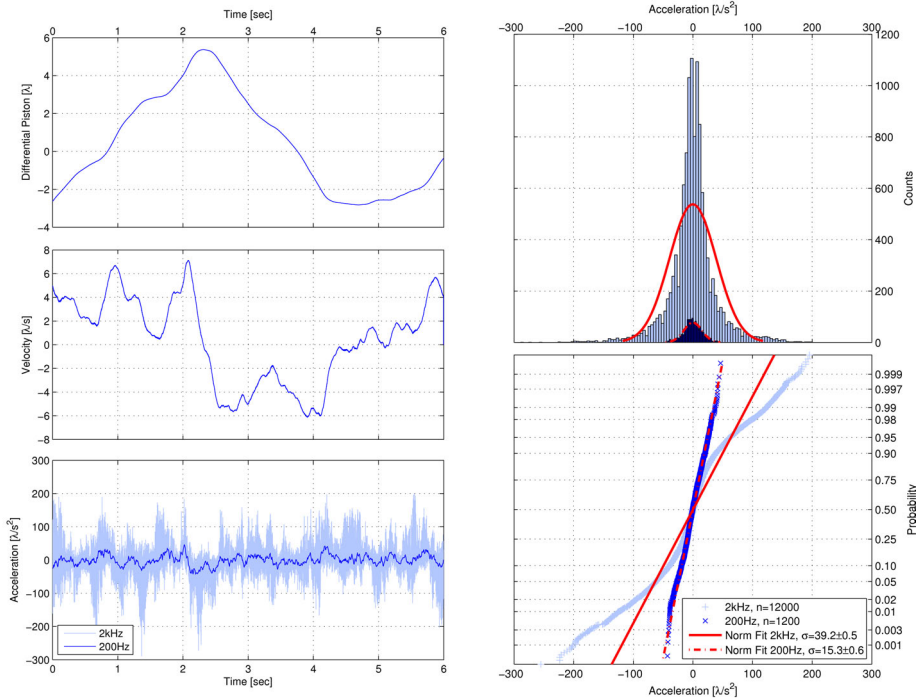
Figure 2.4: *Same as figure 2.3, but for average seeing (San Pedro Martir 0.7"@V).*

early stages of construction. In December 2006 there was a first vibration measurement campaign at the LBT site. The configuration at that time included two primary mirrors, two primary cameras (LBCs), but no secondaries and tertiaries or corresponding dummy masses. Several swing arms were also missing. As a consequence, no complete measurements of OPD effects was possible. Nevertheless a basic understanding of the system and the most critical frequencies could be obtained.

2.3.1 Equipment

The measurement equipment was contributed by LINC-NIRVANA consortium member Max-Planck-Institut für Astronomie (MPIA). Accelerometers based on the piezo-effect were chosen, as they provide convenient handling and high precision with sufficient bandwidth. Additionally a laser vibrometer was used to monitor the intrinsic vibration of the whole system. This device is able to measure true distances by interference of a reflected laser beam from the object. Special reflection markers were therefore attached on different spots on the structure,
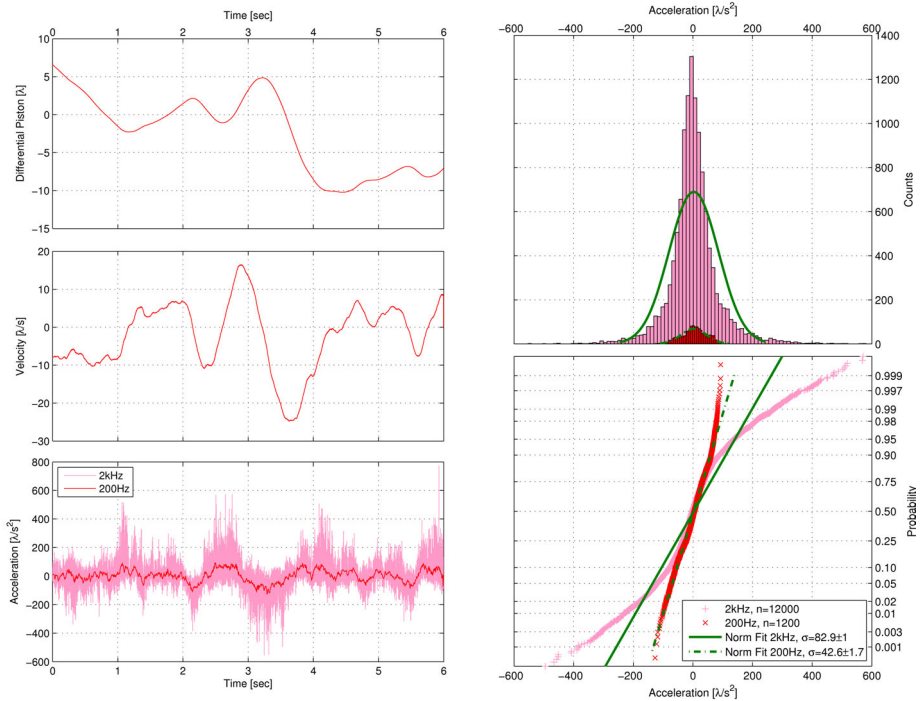
Figure 2.5: *Same as figure 2.3, but for bad seeing (San Pedro Martir 1.5"@V).*
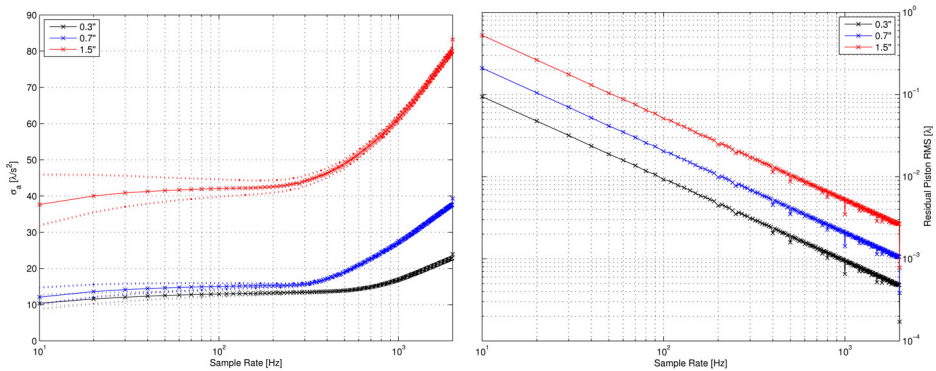
Figure 2.6: *Left: Piston variation as a function of sample rate. The variation is the standard deviation of the fitted normal distribution of the down-sampled piston acceleration. Base sample rate of the piston sequence is 2kHz. In the region of achievable piston sampling of 50–200Hz a nearly constant value can be assumed. The reconstructed piston signal is less varying with lower sample rate as the real piston sequence is smoothed by the down-sampling. The residual error is shown in the plot to the right, for instance for average seeing (0.7") at 200Hz the piston performance will not exceed ~ 0.01λ.*

29

Figure 2.7: *For the vibration measurement accelerometers based on the piezo-effect are used. A shear-force is applied to the piezo-ceramic, if the seismic mass is accelerated vertically, resulting in a voltage signal.*

e.g. LBC blue (Fig. 2.8).

2.3.2 Measurement campaign

The measurement was conducted with two primary goals. First it was tried to monitor vibrations at several strategic spots of the structure in all three translation directions to get a basic model of the system. This can help to understand the origin of critical vibrations and to develop counteraction for the active damping of vibrations, such as additional support structures or decoupling of actuators (Fig. 2.9). The crucial measurement for the FFTS is the OPD monitoring, which were repeated at varying telescope states or modes. This ranges from modes, where all actuators are switched off to the full operating mode simulating a real observation including tracking of the telescope in azimuth and elevation with a realistic velocity. In between the extreme cases actuators are switched on and off individually, if possible.

Instrumental OPD may occur through motions of the optical components in the two optical paths of the interferometer. The main external (non LINC-NIRVANA) segments of the optical path that may be subject to OPD are from the primary to the secondary mirrors and from there to the tertiary and finally to the rails, i.e. the mounting points of the optical bench of LINC-NIRVANA. All structures except the tertiary mirror contribute only in one spatial dimension. The tertiary reflects the light in an angle of 45° and therefore was monitored in horizontal and vertical directions. Since no secondary mirror was available at the time of the first measurement campaign, the LBC – which is actually not used in the interferometric mode of the LBT – was monitored as a substitution because of the similar swing arm and attached mass in comparable distance to the primary mirror. The vibration of the whole structure with the same phase is not contributing to OPD of the two arms. This is monitored additionally with the vibrometer.

Figure 2.8: *Vibration measurement of the LBT: A laser vibrometer is used in OPD direction to monitor intrinsic vibrations of the whole telescope structure relative to the dome building.*
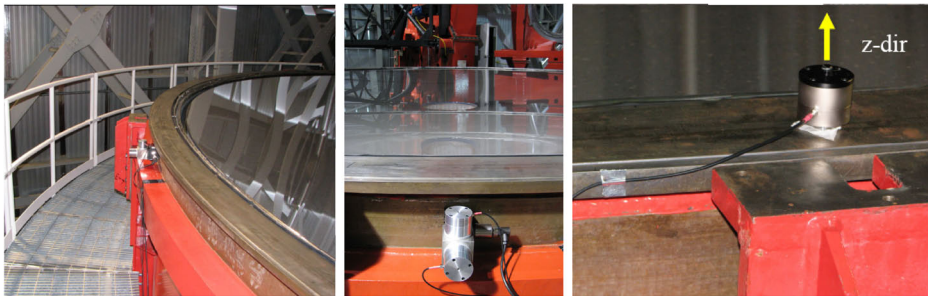

Figure 2.9: *Vibration measurement at the LBT: Accelerometers are mounted to the telescope structure or close to the mirrors. Measurements are taken in 3D simultaneously (left, middle) or in direction of OPD only (right). Additional sensors for the simultaneous OPD measurement are placed on the mounting points (rails) of the LINC-NIRVANA instrument.*

2.3.3 Results

The various actuators and potential sources of disturbance at the telescope were operated individually. This procedure allowed to identify the main contributors to the vibration spectrum. The most severe influence had the mirror floating device and the mirror ventilation respectively, which produces the strongest vibrations. These devices ensure a smooth floating with no tension forces and a homogeneous temperature and laminar air flow accross the primary mirrors. The second most vibration inducing mode is the tracking itself, as the whole telescope is moving around.

The most advanced measurement at the time of the writing of this thesis is a simultaneous OPD measurement at the above mentioned structure points of one arm (Brix & Naranjo 2008). This allows a coherent summation of the acceleration signals of the paths in between and, with appropriate signal filtering and
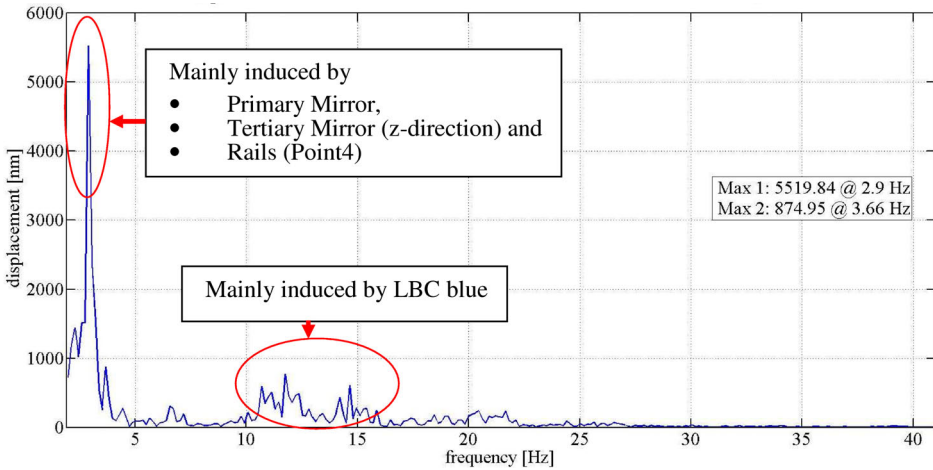
Figure 2.10: *Vibration power spectrum obtained from accelerometer measurements. Displacement is calculated from coherent summation of integrated accelerations in OPD direction (Brix & Naranjo 2008).*

numerical integration, the cumulative displacement spectrum. This first power spectrum is shown in figure 2.10, indicating also the most contributing structures. The primary, tertiary and the rails mainly vibrate at a low frequency of about 2.9Hz with a cumulative amplitude of up to 5.5μm. The swing arm of LBC blue induces vibrations of 12Hz and 15Hz, but with lower amplitudes of 0.8μm and 0.5μm respectively. The measurement was conducted at a telescope tilt of $\sim 20°$. An upper limit of about 25Hz seems promising, when considering the sampling frequency of the FFTS of 100–200Hz. Also the maximum amplitude of the displacements is in the range which can be handled by the FFTS actuator. For the first tests of the performance of the system and the design of the control loop different graduations of this power spectrum and the main contributing frequencies were used.

2.3.4 Outlook

Additional measurement campaigns at the LBT are scheduled, as there are still several open questions and the power spectrum is considered to be preliminary. The measurements have to be repeated, when additional parts are installed, such as the final secondary and tertiary mirrors. It is still not clear, how the both arms differ in their vibrational behavior. Maybe there are even phase correlations, but it is possible that a totally different power spectrum occurs.

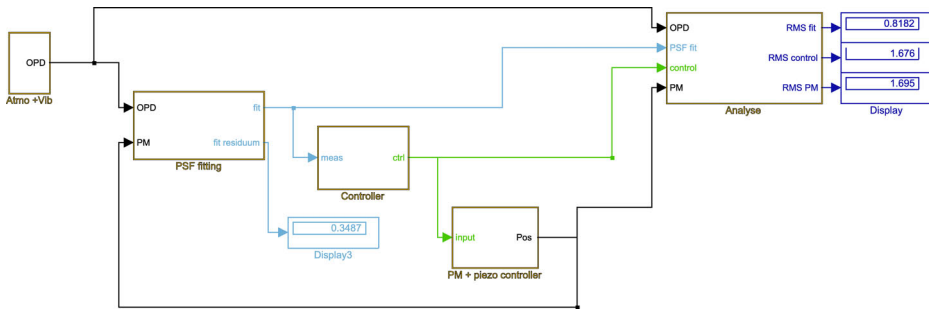From the promising results of measuring OPD accelerations at different lo-

Figure 2.11: *SIMULINK model for the simulation of the control loop performance with different atmospheric conditions and disturbances from sampling effects, latencies, PSF-fit noise and telescope vibrations. A dynamic model for the piezo actuator with piston mirror load includes the PI-control algorithm of the piezo controller.*

cations simultaneously the idea arose to permanently install the sensors at the LBT structure. The spots of critical contribution to vibration could be monitored even during observations and parameters of the control loop could be adapted accordingly. Similar to the efforts to monitor the atmospheric turbulence with a differential image motion monitor (DIMM, Kornilov et al. 2007) installed at the LBT dome, the vibration monitor could help to improve the overall performance of the instrument (cf. Sect. 2.5).

2.4 Simulation setup

The residual piston and with it the performance of the LINC-NIRVANA instrument is affected by many parameters. To investigate the performance under different conditions a simulation framework was set up as a MATLAB/SIMULINK model (Fig. 2.11). In the following an overview of the framework is given.

Figure 2.11 shows the SIMULINK model for the FFTS control loop. The inclusion of varying environmental conditions is based on atmospheric MCAO simulations by LOST as described in chapter 2.2. Because of the time-consuming simulation of the atmosphere a direct interface from LOST (IDL) to MATLAB was skipped. Pre-computed simulations of representative seeing conditions are used as atmospheric piston input. For the instrumental piston from vibration (and eventually flexure) this signal is mixed with vibrations of arbitrary frequencies and amplitudes, e. g. according to the power spectrum in figure 2.10. The system is numerical simulated with a Runge-Kutta (Dormand & Prince 1980) integrator with variable stepsize.
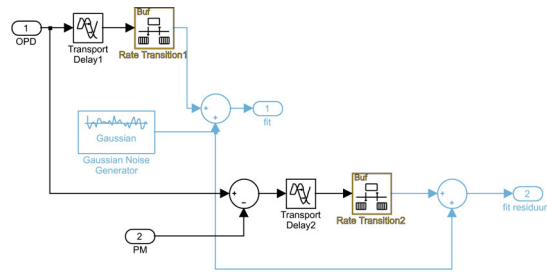
Figure 2.12: *SIMULINK model block of the disturbed piston measurement. The PSF fit error is normal distributed with standard deviation σ_{fit}. The signal is delayed due to the DIT and a rate transition is applied according to the detector sampling frequency.*

2.4.1 Piston measurement disturbance

PSF fitting

Bertram et al. (2006) developed an image analysis concept with a multidimensional PSF-fitting algorithm. Differential piston can be determined even with a low signal-to-noise ratio (SNR). Nevertheless the quality of fit will decrease with decreasing SNR, which in turn is dominated by the detector readout noise. Thus the frame rate of the detector is a tradeoff between sampling rate and measurement error of the piston signal. As the sampled signal is also delayed, extrapolation or prediction performance is important. With increasing noise due to the fitting, the prediction becomes difficult. The disturbances of the piston measurement are simulated in the SIMULINK model, an overview of the corresponding model block is shown in Fig 2.12.

The OPD is measured with the FFTS-detector at a fixed frame rate which is limited by the magnitude of the reference star. The higher the magnitude the greater the DIT to achieve a reasonable SNR. The SNR of the reference star PSF has a strong impact on the piston analysis performance and requires therefore a minimum exposure time. The achieved frame rate with an image size of 32×32 pixels is 100-200 Hz (cf. Fig. 2.13). The piston power spectrum which can be corrected for is therefore limited to the Nyquist frequency (50-100 Hz). With no knowledge of the behavior of the piston in between the samples, the FFTS performance will decrease with lower sampling rates (Fig. 2.6).

Sampling rate

To classify the discrete sampling of a signal as disturbance is somewhat misleading. Nowadays nearly all information and measurement is acquired, processed and stored in digital form and therefore sampled in some way. According to
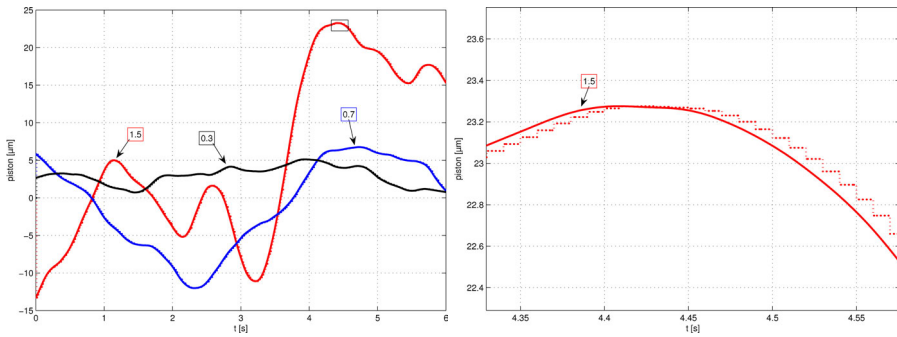
Figure 2.13: *Simulation of the differential piston at different atmospheric conditions: seeing is 1.5", 0.7" and 0.3" respectively. To the right in a zoomed view the sampled signal with a sampling rate of 100 Hz and a delay of 8 ms (estimated latency for the FFTS) is visible.*

the Nyquist-Shannon theorem (Shannon 1949) for complete reconstruction the lowest sampling frequency of a continuous signal is greater than twice the bandwidth.

It is evident, that for every process with virtually unlimited bandwidth information is lost by discrete sampling. The signal has to be low-pass filtered with the Nyquist-frequency to avoid aliasing effects. Several different techniques exist to reconstruct a continuous signal from discrete sampling (Lesurf 2001). Techniques for the piston estimation and reconstruction are discussed in section 2.5.

Latencies

Because of the integration time of the PSF image acquisition, the read-out time, A/D-conversion and image analysis the piston signal is also delayed. In figure 1.11 the estimated latencies during the analysis of the piston are noted, which sums up to a delay of $\tau_s \sim 8$ms. The effect of the delay on the error is visible in Fig. 2.13 to the right. For stable control the latency should be kept as small as possible, but also a constant delay is desired, i.e. no jitter of the processing time. Wang et al. (2006) examined the latency variance on a real-time computer system and introduced a software solution for fast and time stable data processing.

2.4.2 Dynamic model

State space equations

A general control configuration is of the form as shown in figure 2.14. This represents a wide class of control problems including the consideration of modeling
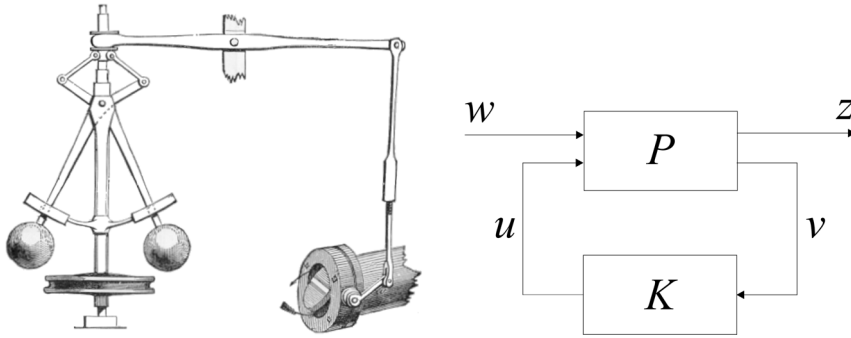
Figure 2.14: *Left: The centrifugal governor is a famous example for a feedback controller from the industrial age. It regulates the opening of the valve for a steam engine proportional to the rotation speed (Maxwell 1868). Right: general control configuration. The plant P includes also a disturbance model and the interconnection between plant and controller K, i.e. the feedback. The identification of the inner structure of P is necessary to find optimal controllers. w are the exogenous inputs, i.e. the set-point r including disturbances and noise d (w = r + d). z are exogenous outputs, i.e. the error signal to be minimized y − r. u is the control signal and v the measured (with noise n) controller inputs v = y + n.*

and measurement uncertainty. For the design of a controller it is of great importance to obtain a realistic model of the system or the plant[1]. In the case of a plant without modeling uncertainty a linear time-invariant dynamical system (LTI) with inputs u, outputs y and state vector x is most convenient noted with the state space description, i.e. a set of first-order differential equations

$$\dot{x}(t) = Ax(t) + Bu(t)$$
$$y(t) = Cx(t) + Du(t) \tag{2.1}$$

and real matrices A, B, C and D. The internal, mostly hidden state variables $x_i(t)$ are the smallest set of system variables that describe the entire state at any time. By applying the (unilateral) Laplace-Transformation

$$F(s) \quad = \mathcal{L}\{f(t)\} = \int_0^\infty e^{-st} f(t)dt \tag{2.2}$$

the system 2.1 is described in the frequency domain as

$$sX(s) = AX(s) + BU(s)$$
$$Y(s) = CX(s) + DU(s) \tag{2.3}$$

with the complex variable s. Operating in the frequency domain has several advantages for control problems. In the following a few examples are presented.

---

[1]The term "plant" in control theory refers to the combination of process and actuator

The differentiation of a time domain function $f'(t)$ converts in the frequency domain to

$$\mathcal{L}\{f'(t)\} = sF(s) - f(0) \tag{2.4}$$

as already used in 2.3. Integration gives

$$\mathcal{L}\left\{\int_0^t f(\tau)d\tau\right\} = \frac{1}{s}F(s) \, . \tag{2.5}$$

An ideal time delay converts to

$$\mathcal{L}\{\delta(t - \tau)\} = e^{-\tau s} \, . \tag{2.6}$$

These are often used relationships in control theory, for a comprehensive overview see Isermann (1992); Skogestad & Postlethwaite (2005), e. g.

Transfer functions

The forward dynamics problem is related to the response of the system to a given input $u(t)$. The transfer function is defined as the ratio from output to input in the frequency domain

$$G(s) = \frac{Y(s)}{U(s)} \, . \tag{2.7}$$

For the system 2.1 the transfer function can be noted as

$$G(s) = C(sI - A)^{-1}B + D \, , \tag{2.8}$$

so in general a transformation between state space and transfer function representations of models is possible[2]. Transfer functions are commonly expressed in the rational form

$$H(s) = \frac{\sum_n a_n s^n}{\sum_n b_n s^n} \tag{2.9}$$

with the order n. Another form of representing a LTI is the poles/zeros-notation, with each notation showing advantages in different applications and analysis approaches (Skogestad & Postlethwaite 2005).

---

[2]the matrix A has to be invertible

2.4.3 Model estimation

The actuator of the Fringe and Flexure Tracking System is the piston correction mirror, which is moved by a piezoelectric-driven linear stage (Fig. 1.10). Piezo-electric ceramics or PZTs[3] are limited to small distances but are extremely stiff and achieve high accelerations. The high force of several 10^4N that PZTs can generate makes them best-suited for the problem of moving as fast as possible a relative high weight over a moderate range with very high precision. A disadvantage, however, is a highly nonlinear input-output behavior. For a certain input there is no unique output, so the PZT shows strong hysteresis. Furthermore it tends to drift. This can be solved with closed-loop control. In conjunction with high-precision capacitive feedback sensors, which provide resolutions of 10^{-8}m and below, a repeatability of down to 1nm can be achieved.

The design of the piston mirror was optimized in terms of light-weight and stiffness (Rohloff 2005). Because of the constraints of the optical system of a homothetic imager the two beams have a quiet large diameter, so the mirror has to have a minimum surface to reflect the whole beams. As a result the load which has to be moved ist still as high as 3350g.

A rule-of-thumb is, that a PZT can reach its nominal displacement in approximately

$$t_{\min} \approx \frac{1}{3f_0} \; . \tag{2.10}$$

The resonant frequency f_0 in turn is a function of the effective load mass m_{eff} and the actuator stiffness k

$$f_0 = \frac{1}{2\pi} \sqrt{\frac{k}{m_{\mathrm{eff}}}} \tag{2.11}$$

with $m_{\mathrm{eff}} \approx m_{\mathrm{PZT}}/3 + m_{\mathrm{load}}$. This is valid for masses not exceeding the maximum load capacity. It is clear that a substantial decrease of the resonant frequency is inevitable. Relevant specifications of the piezo stage PI-750 from manufacturer *Physik Instrumente*, which was chosen to be used in LINC-NIRVANA are listed in table 2.2.

The frequency response of the piezo stage was measured with a dummy load corresponding to the mirror mass by the manufacturer. This is up to now the only information available. Currently there are efforts to precisely measure the response of the real mirror and stage at the MPIA. First results are shown in

---

[3]PZT is an abbreviation for the chemical formula of lead zirconate titanate, $Pb[Zr_xTi_{1-x}]O_3$, $0 < x < 1$
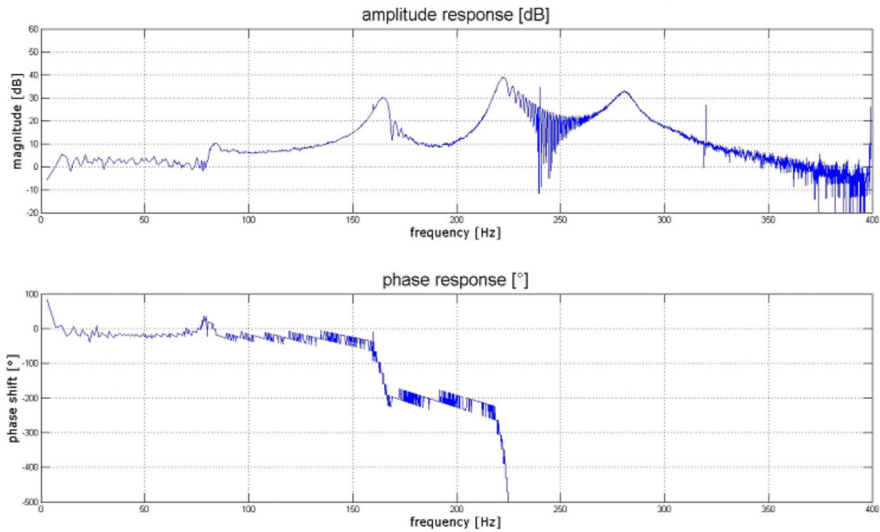
Figure 2.15: *Bode plot of the piezo stage and piston mirror in open-loop configuration. The dynamics is limited by the first resonance peak at around 160Hz, where the phase drops under -180°.*
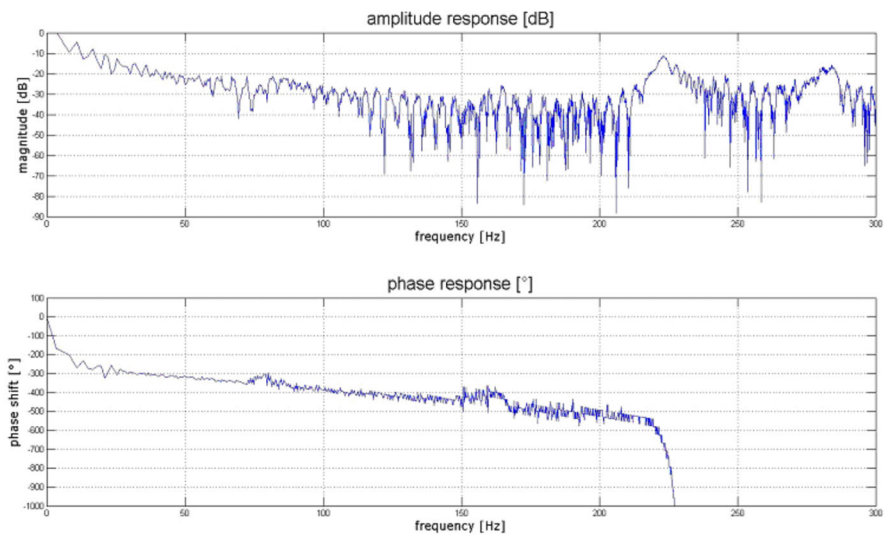

Figure 2.16: *Bode plot of the piezo stage and piston mirror in closed-loop configuration of the PI-controller. The dynamics here is dependent on the sampling rate and feedback structure of the controller. It seems the bandwidth is limited to about 8Hz.*

Table 2.2: *Parameters of the piezo-electric actuator*

Parameter	Value
Travel range	75 μm
Feedback sensor precision	1 nm
Stiffness (k)	12 N/μm
Force capacity	800 N
Max. load	10 kg
Unloaded resonant freq.	600 Hz

figures 2.15 and 2.16. In closed-loop the bandwidth drop is enormous. This is related to the control device, which is optimized for precise but slow scanning operations. The controller from *Physik Instrumente* operates with proportional-integral (PI) closed-loop control at 5kHz. Also some protocol problems are not solved yet. However, until reliable measurements are available, the simulations are based on a dynamic model obtained from the frequency response of the piezo stage with a dummy load.

Figure 2.17 shows the measured step and frequency response (Bode plot) of a piezo stage without load and with additional piston mirror load in comparison. A first resonance peak is visible at about 150 Hz. The unloaded piezo data is a parametric model taken from Chen et al. (1999). For the simulation of the mirror system dynamics a parametric model has been obtained with the MATLAB System Identification toolbox as follows: the sampled data of the measurement of the frequency response of the dummy load system can be used to fit a black-box model with the prediction error method (PEM), a recursive estimation technique (Ljung 2002). By supplying the unloaded PZT model as initial model PEM trys to fit a similar structure to the data. The result shown in figure 2.17 has the two resonant peaks, but is characterized in general by lower orders for the resonance maxima and magnitude/phase drops. Another approach is to scale the parametric model of the unloaded piezo to lower the resonance frequency as indicated by equation 2.11. The result shows a more realistic drop for higher frequencies, but the first resonance peak is located too close to the second at a slightly too high frequency. After transforming the obtained model for the sampled data to
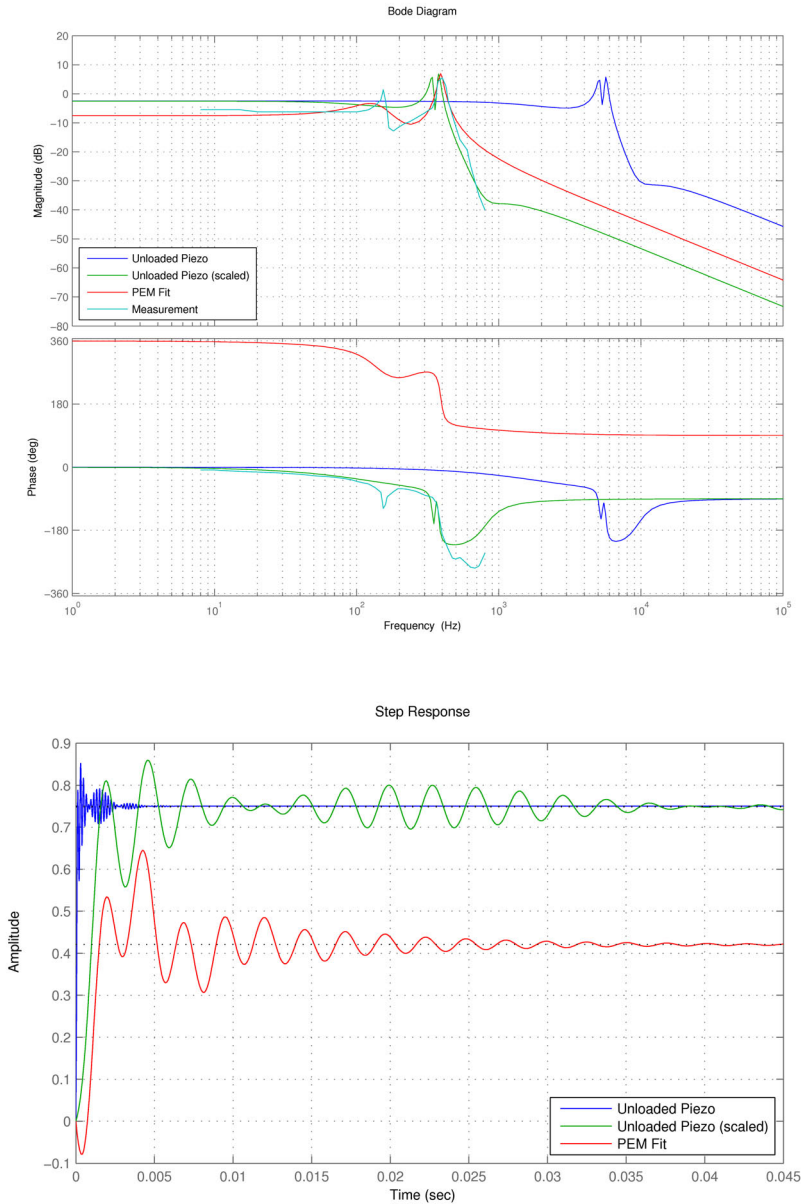
Figure 2.17: *The frequency response (top) of the piezo-driven system depends strongly on the load mass. A unloaded piezo stage has a much higher resonance frequency than a one with a additional load. First measurements were done with a dummy load corresponding to the mirror mass and show a resonance peak at ~150 Hz. To obtain parametric models the unloaded model was scaled.*

continuous time the state space formulation (Eqn. 2.3) is denoted as

$$
A = \begin{pmatrix}
-326.9 & 828.7 & 1123 & -376.4 & -186.4 \\
-678.4 & -14.72 & 25.21 & -2090 & -12.18 \\
-1624 & 91.61 & -190 & 761 & 1454 \\
761.8 & 2002 & -466.7 & -113.8 & 334.4 \\
-619.8 & 194 & -2071 & 139.4 & -493.4
\end{pmatrix}
$$

$$
B = \begin{pmatrix}
-9164 \\
4001 \\
808.1 \\
4804 \\
-12030
\end{pmatrix}
\tag{2.12}
$$

$$
C = (0.3295, -0.003964, 0.3568, -0.1368, -0.2944)
$$

$$
D = 0
$$

This is a first model of the combined actuator and piston mirror load and is used in the following for simulations of the systems response. It shows the expected decrease in resonant frequency and the critical phase behavior at higher frequencies. Tests with stronger scalings, so that the first resonance peak is better reproduced showed no significant difference in performance. However, final performance estimates of the whole FFTS will only be possible as recent as a precise model from measurements is available.

2.4.4 Control law requirements

The final control algorithm for the FFTS has to fulfill some requirements arising from the complex and varying disturbance conditions. It should have a temporal prediction ability to compensate for the inevitable delay due to the detector integration/readout time and the image processing. The prediction ideally bridges the gap between samples of the piston signal with a time-dependent extrapolation, so that the control signal is a smooth curve based on the most likely piston state and variation. As a consequence the control loop will operate with a much higher sampling rate than the image acquisition, probably limited by the available real-time processing power. Model uncertainties such as the underlying piston power spectrum, measurement covariances and the system dynamics must not affect the overall performance too much or even lead to control un-stabilities such as steady state errors. These offset errors, as well as phase shifts, substantial overshooting and temporal un-stabilities can severely reduce the fringe contrast over the science detector integration time (DIT). Residual piston from conservative and less aggressive control setups will also decrease the performance. The
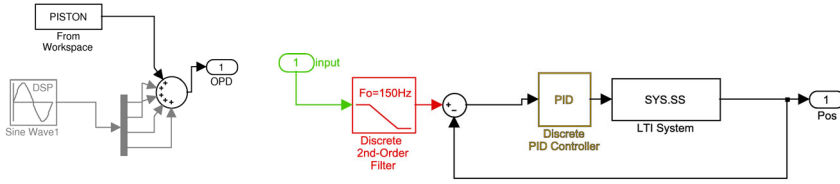
Figure 2.18: *SIMULINK model blocks OPD and PM+piezo controller (cf. Fig. 2.11). The piston signal consists of the pre-computed atmospheric piston and vibrations. The piezo system consists of the LTI model for the piezo stage and mirror load and a tuned PID controller in feedback loop.*

primary objective of the control design is to achieve precise tracking of almost arbitrary input signals with high control bandwidth in spite of external disturbance.

The variations in input conditions are not known or predictable, so the algorithm itself should not be very complex or abstract, as only simplified simulations can be tested during the design. With exotic control approaches, e.g. neural networks untested input states and sequences can eventually cause a inconsistent state of the controller which can result in total performance breakdown.

2.4.5 Classical control approach

The all purpose tool of classical control is the proportional-integral-derivative controller (PID). The transfer function of the PID with the gains K is (cf. Eqns. 2.4 and 2.5)

$$H_{\text{PID}}(s) = \frac{K_D s^2 + K_P s + K_I}{s} \ . \tag{2.13}$$

The proportional gain K_p will have the effect of reducing the rise time and will reduce, but never eliminate, the steady-state error. The integral gain K_i will have the effect of eliminating the steady-state error, but it may make the transient response worse. The derivative gain K_d will have the effect of increasing the stability of the system, reducing the overshoot, and improving the transient response. The closed-loop transfer function for a system P is in classical feedback configuration

$$H_{\text{CL}}(s) = \frac{P(s)H_{\text{PID}}(s)}{1 + P(s)H_{\text{PID}}(s)} \ . \tag{2.14}$$

It can be seen, that if $P(s)H_{\text{PID}}(s) \gg 1$ for all s the transfer function will be close to 1, and because of the definition in Eqn. 2.7, $Y(s) \approx U(s)$, i.e. the ideal control configuration.
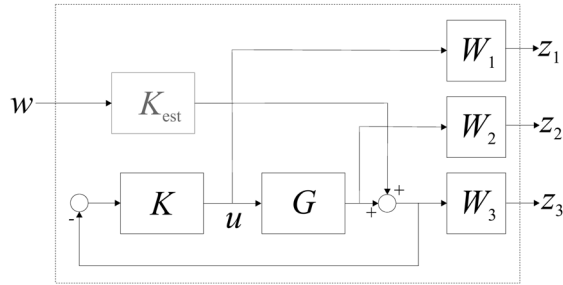
Figure 2.19: *The plant P of the general control configuration in figure 2.14 is supplemented with weighting transfer functions for the controller design. G is the actual physical system, i.e. the PZT actuator with mirror load. K is the controller, which is to be optimized. The input w includes also an estimator K_{est}, this is discussed in section 2.5.*

A simple P-controller is for example the governor of a steam engine (cf. Fig. 2.14), K_P referring to the rotating masses. The hardware piezo controller from *Physik Instrumente* is a pure PI-controller ($K_D = 0$), which explains the limited closed-loop frequency response (Fig. 2.16). However, to simulate the piezo response in the model, an optimized set of K_P and K_I parameters was obtained for the system in equation 2.12. The PI(D) was tuned by hand and was tested to be stable[4] for all piston sequences including disturbances. A systematic PID parameter tuning technique is the Ziegler-Nichols method (Ziegler & Nichols 1942). The piston signal is low-pass filtered and the PID has gain margins to avoid unstabilities due to the resonance peaks at higher frequencies (Fig. 2.18).

2.4.6 Optimal control

The term optimized controller refers to a mathematical optimization, i.e. minimization of a cost function, which is defined in a way to evaluate the performance of a control system. A controller is therefore optimized only in terms of a given performance weighting.

Considering the limited bandwidth of the actuator due to the piston mirror load and the unsolved problems with the hardware controller in closed-loop (Fig. 2.16) the question arose, if a more sophisticated control approach might significantly improve the performance. A tuned controller for the specific problem should be an advantage, but also implies a specific, probably complex hardware design.

For the cost function a norm is applied to the transfer function $f(s)$ of the sys-

---

[4]stable in control theory means for any bounded input, the output is also bounded (BIBO stability)
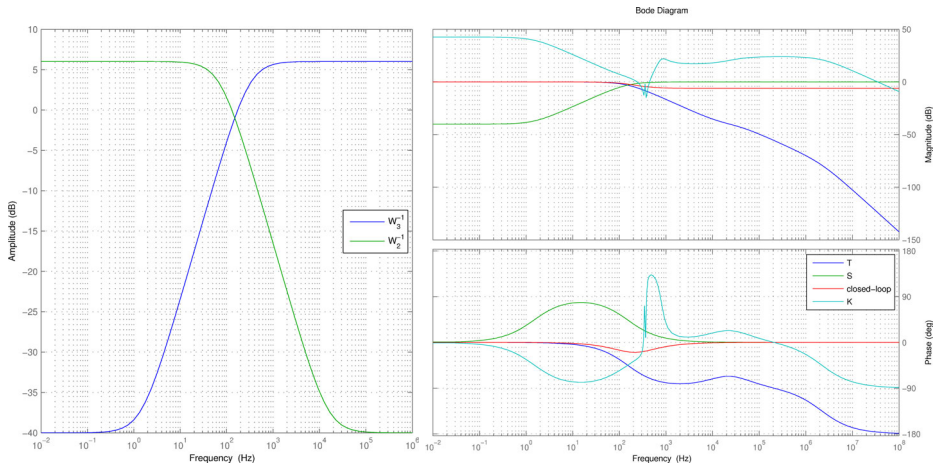
Figure 2.20: *The inverse weighting functions for application of the $\mathcal{H}_\infty$ norm are shown to the left for a desired bandwidth of 150Hz. Right: result of the optimization. The shaped controller K (turquoise line) is similar to the inversion of the system G (cf. Fig.2.17). The achieved closed-loop transfer function (red line) is nearly flat.*

tem, commonly used are norms in the Hardy-space (Skogestad & Postlethwaite 2005)

$$\|f(s)\|_2 = \sqrt{\frac{1}{2\pi} \int\limits_{-\infty}^{\infty} |f(i\omega)|^2 \, d\omega} \tag{2.15}$$

$$\|f(s)\|_\infty = \max_\omega |f(i\omega)| \tag{2.16}$$

which is referred to as $\mathcal{H}_2$ and $\mathcal{H}_\infty$ control respectively. In the following it was tried to design a $\mathcal{H}_\infty$-controller for the dynamic model of equation 2.12.

The plant P in figure 2.14 is extended with weighting transfer functions W for the application of the norm (Eqn. 2.16). The weights are commonly placed as shown in figure 2.19, allowing different classifications of the system behavior. The plant can then be written as

$$\begin{pmatrix} z_1 \\ z_2 \\ z_3 \\ v \end{pmatrix} = P \begin{pmatrix} w \\ u \end{pmatrix} = \begin{pmatrix} 0 & W_1 I \\ 0 & W_2 G \\ W_3 I & W_3 G \\ -I & -G \end{pmatrix} \begin{pmatrix} w \\ u \end{pmatrix} . \tag{2.17}$$

G is the actual physical system (Eqn. 2.12), eventually including modeling uncertainties. The entity of the controller K and the plant G is described by the

following functions. $L = GK$ is the (open) loop transfer function, the closed-loop transfer function is

$$T = \frac{GK}{1 + GK} = \frac{L}{1 + L} \, .$$ (2.18)

The inverse function is called the sensitivity function[5]

$$S = \frac{1}{1 + GK} \, .$$ (2.19)

For a good performance T has to be as close to unity as possible, as it relates the input w to the output y. But since $w = r + d$ consists of the set-point r and disturbances d, T should also reject unwanted frequencies of w, so T is as small as possible in this case. Hence T judges the robustness of the system. S in turn measures the impact of unmodeled high-frequency dynamics and measurement noise n on the residual error $e = y - r$, i.e. the control performance. As S should be as small as possible, this is a conflicting requirement, since $S + T = 1$, as easily seen from equations 2.18 and 2.19. The meaning of the weights can now be identified as (Skogestad & Postlethwaite 2005):

- W_3 weights the sensitivity function S, and when $W_3 S$ is minimized in the $\mathcal{H}_\infty$ norm, the residual control error is limited.

- W_2 weights the complementary sensitivity function T, minimizing $W_2 T$ avoids sensitivity to noise and results in robustness.

- W_1 weights the controller output $u = KSw$, so minimizing $W_3 KS$ penalizes large plant inputs and effectively limits the controller output, i.e. a gain margin.

The optimization problem can then be written as

$$\gamma = \min_{K} \|N(K)\|_\infty , \quad N = \begin{pmatrix} W_1 KS \\ W_2 T \\ W_3 S \end{pmatrix} ,$$ (2.20)

i.e. to find the controller K which minimizes the $\mathcal{H}_\infty$ norm. To the left of figure 2.20 W_2^{-1} and W_3^{-1} are shown for a desired bandwidth of 150Hz, weighting with W_1 was omitted. The evaluation of Eqn. 2.20 and the shaping of the controller K is done in MATLAB with the two-Riccati formulae (Doyle et al. 1989) and a γ-iteration technique to find the optimal value of γ, i.e. the defined cost. The

---

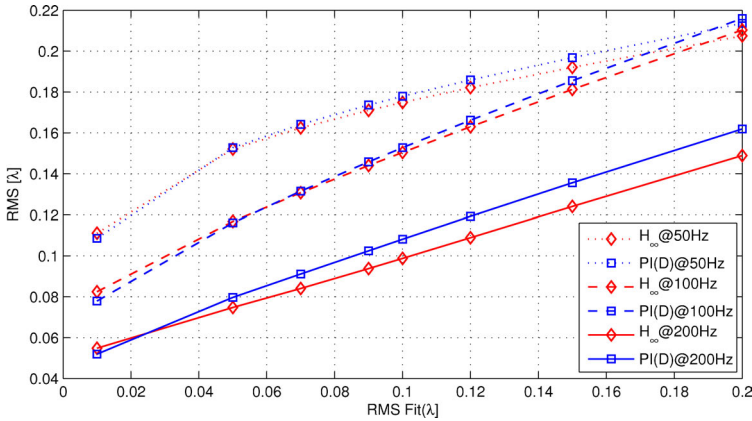[5]T is often referred to as the complementary sensitivity function

Figure 2.21: *Performance simulation of the $\mathcal{H}_\infty$ controller in comparison to the tuned PI(D). Shown is the residual OPD error (RMS) as a function of PSF fitting error for sampling rates 50, 100 and 200 Hz.*

obtained controller and the closed-loop transfer function are shown in Fig. 2.20. In direct comparison with the tuned PI(D) the optimized controller is shown in figure 2.21. Indeed a performance advantage is seen. Especially under difficult conditions with increased measurement noise $\mathcal{H}_\infty$ provides a decreased residual piston. It is clear, that the greatest improvement is achieved at 200Hz, since this sampling rate imposes control signals with higher frequencies than the resonance frequency. It might be worth to design a new hardware controller which incorporates the result, if the problems with the *Physik Instrumente* controller cannot be solved. Even if the actual achievable PI(D) performance is comparable to the tuned software controller, the improvement of up to 8–9% (at 200Hz) of the $\mathcal{H}_\infty$ approach could provide a significantly increased sky coverage of the instrument.

However, the most performance critical part of the system seems to be the piston estimation process. As indicated in figure 2.19 the noisy and disturbed inputs have to be filtered to achieve a reasonable piston estimation. This technique is discussed in the following section.

2.5 Piston estimation

There are many possibilities to reconstruct a sampled signal. The most simple is the zero-order-hold (ZOH) technique (Fig. 2.13), which implies holding the last value constant until the next measurement. The residual error of this technique is shown in figure 2.22 (red line).

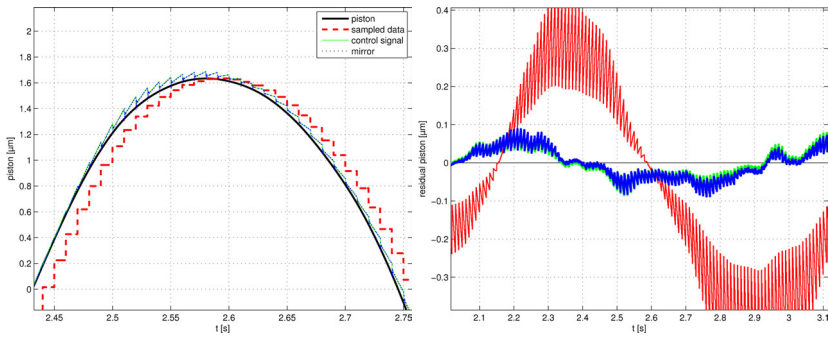The control signal and the residual piston can be improved with a simple

Figure 2.22: *A predictor approach for the undisturbed piston signal improves the control performance, the residual piston (right) is decreased. In this example the last 5 samples are extrapolated at the time $t + \tau_s$ to compensate the latency.*

predictor. After the PSF fitting algorithm the signal is resampled to a higher sampling rate (e. g. 2 kHz). By evaluating the derivative for the last n samples the trend of the piston can be extrapolated. The extrapolation also takes care of the latency by evaluating the time $t + \tau_s$. The resulting discontinuities can be compensated with a discrete (low-pass) filter. Figure 2.22 shows that this approach can improve the control performance significantly for the case of an undisturbed signal.

However, the piston prediction based on extrapolation is inappropriate for a disturbed signal, i.e. the noisy measurement of the piston with PSF fitting. The consideration of the error of the piston measurement as well as the underlying physical model leads to the formal description of the optimal estimator.

2.5.1 Kalman filtering

An improvement of the simple prediction filter algorithm can be achieved, if a priori knowledge of the system is considered. The optimal linear estimator was already developed by Kalman (1960). The Kalman filter found its first famous implementation in the navigation computer of the Apollo space program for the numerical calculation of trajectory correction. Nowadays Kalman filtering is often applied to challenging control tasks and also used in telescope engineering (Le Roux et al. 2004).

The Kalman filter is formulated in the discretised time domain. The assumption for the linear dynamical system is, that given a state x_k in the present, the

future state x_{k+1} is completely independent [6] of the past state x_{k-1}. The state space vector evolves therefore with the state transition matrix F_k

$$x_k = F_k x_{k-1} + B_k u_{k-1} + w_{k-1} \tag{2.21}$$

with u_k the control vector, B_k the control input and w_k the process noise with the covariance matrix Φ_0.

The Kalman filter is the optimal recursive estimator. The state of the system at time k is predicted with the past state $k-1$ and then updated with the measurements z_k, weighted with the measurement error v_k. The process noise w_k and the observation noise v_k are assumed to be normal distributed with the covariances Q_k and R_k. The state of the filter is the estimated system state $\hat{x}_{k|k}$ plus the error covariance $P_{k|k}$. The prediction phase of the filter is then formulated

$$\begin{aligned} \hat{x}_{k|k-1} &= F_k \hat{x}_{k-1|k-1} + B_k u_{k-1} \\ P_{k|k-1} &= F_k P_{k-1|k-1} F_k^t + Q_{k-1} \end{aligned} \tag{2.22}$$

followed by the updating phase with the measurement residual y_k:

$$\begin{aligned} y_k &= z_k - H_k \hat{x}_{k|k-1} \\ S_k &= H_k P_{k|k-1} H_k^t + R_k \\ K_k &= P_{k|k-1} H_k^t S_k^{-1} \\ \hat{x}_{k|k} &= \hat{x}_{k|k-1} + K_k y_k \\ P_{k|k} &= (I - K_k H_k) P_{k|k-1} \end{aligned} \tag{2.23}$$

In the current implementation of the filter to estimate the atmospheric piston the system is assumed to obey linear dynamics. That means that the piston state x can be described by the instantaneous piston ϵ and the first derivative, i.e. the velocity

$$x = \begin{pmatrix} \epsilon \\ \dot{\epsilon} \end{pmatrix} . \tag{2.24}$$

The state transition matrix for the time step Δt is constant

$$F(\Delta t) = \begin{pmatrix} 1 & \Delta t \\ 0 & 1 \end{pmatrix} . \tag{2.25}$$

Since the filter is formulated in the discrete time domain, the variation analysis of simulated piston sequences in section 2.2.2 was done in the time domain rather

---

[6]such a time series is called a Markov chain

then in the frequency domain. It is also important, that the variation differs not too much from the normal distribution, since the Kalman filter assumes white process noise. The covariance of the process noise can therefore be denoted with the piston acceleration σ_a, as investigated for representative atmospheric conditions. The process noise is then denoted with

$$Q = \sigma_a^2 GG^T \,, \quad G = \begin{pmatrix} \frac{\Delta t^2}{2} \\ \Delta t \end{pmatrix} \,. \tag{2.26}$$

$R_k = \sigma_{\text{fit}}^2$ is the piston fit error, dependent on the reference star magnitude and DIT. $H = (1, 0)$, since the measurement involves only ϵ. No control input is considered, so $u = 0$. With these definitions the evaluation of equations 2.22 and 2.23 provides an estimation of the piston signal, which weights the noise contributions. Figure 2.23 shows the dependence of the performance on σ_a and on the PSF fitting error σ_{fit}.

Since the Kalman filter is capable of processing any available measurements regardless of their precision, it would also be possible to incorporate piston estimates from the MCAO system. A software interface to the corresponding control system, which provides the AO correction information might improve estimates of the piston state and the variation. The current implementation of the filter allows an easy extension of the measurement inputs.

The prediction of the piston inbetween samples takes advantage of the estimated state, including the velocity $\dot{\epsilon}$. After the updating phase k of the filter (Eqn. 2.23) the actual piston is then evaluated due to the latency τ_s in the time range $t_k \leq t \leq t_{k+1}$ until the next prediction/updating phase with

$$x(t) = F(t + \tau_s)x_k \,. \tag{2.27}$$

2.5.2 Vibration filtering

Petit et al. (2004) proposed a modified Kalman filter which can handle vibration, this approach was tested also by Egner (2006). Consider the trigonometric addition theorems

$$\begin{aligned} \cos(\alpha + \tau) &= \cos(\alpha)\cos(\tau) - \sin(\alpha)\sin(\tau) \\ \cos(\alpha - \tau) &= \cos(\alpha)\cos(\tau) + \sin(\alpha)\sin(\tau) \end{aligned} \tag{2.28}$$

Cancelling $\sin(\alpha)\sin(\tau)$ gives then

$$\cos(\alpha + \tau) = 2\cos(\alpha)\cos(\tau) - \cos(\alpha - \tau) \,. \tag{2.29}$$
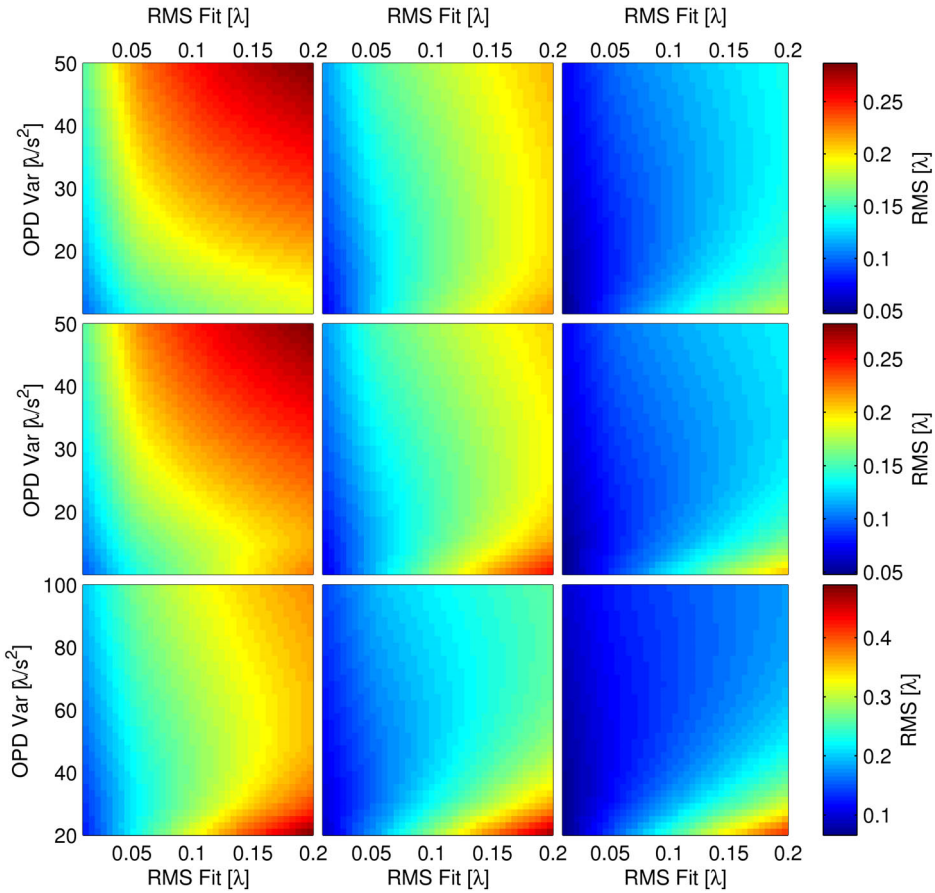
Figure 2.23: *Performance simulation of the Kalman filter. Shown is the residual OPD error (RMS) as a function of PSF fitting error and OPD variance as the parameter for the Kalman filter. From left to right for sampling rates 50, 100 and 200 Hz. From top to bottom for 0.3", 0.7" and 1.5" seeing conditions. The latency is 8 ms.*

This can be identified as a recursive formula for a general harmonic oscillation

$$\hat{A}(t) = A_0 \cos{(\omega t + \phi)} \tag{2.30}$$

as discrete time series $A(n)$ with sampling time τ, $t = n\tau$. If $A(0) = A_0 \cos{(\phi)}$ is the value at time $t = 0$ and

$$\Phi = \cos{(\omega \tau)} = \cos\left(\frac{2\pi f_{\text{vib}}}{f_{\text{sample}}}\right) \tag{2.31}$$

we get

$$A(n+1) = 2\Phi A(n) - A(n-1) . \tag{2.32}$$

51

Note that the frequency $f_{vib} = \frac{\omega}{2\pi}$ and the phase ϕ are not needed, if the constant Φ and the initial sample values $A(0)$ and $A(1)$ are known.

The state of the Kalman filter (Eqn. 2.24) is then extended with the two past vibration occurrences $A(k-1)$ and $A(k-2)$, and the new state transition matrix considers Eqn. 2.32 (Petit et al. 2004).

This approach seems only suitable for a single vibration frequency. A first test with several different frequencies without phase correlation showed, that no robust estimation of the initial amplitudes is possible any more. Hence this technique is limited to correct for the strongest contribution to the vibration power spectrum only, i.e. the low frequency vibration around 2.9Hz (Fig. 2.10). Further tests with modified state models for vibrations and atmospheric piston are in progress. A promising approach seems to be the application of additional, tuned (notch and band-pass) filters to seperate the vibration and atmospheric spectrum for the estimation.

2.5.3 Adaptive control

The measurement campaign at the LBT (cf. Sect. 2.3) included a vibration monitoring of a spot at the top of the telescope enclosure. A differential image motion monitor (DIMM, Kornilov et al. 2007) is planned to be installed at that place to steadily monitor the atmospheric seeing during an observation. As already shown the standard deviation of the piston as well as the temporal variation scale with the Fried parameter r_0 (cf. Eqn. 1.7). Additional improvement of the performance of the piston estimation could be achieved, if the actual measured r_0 value is fed into the control loop, precisely into the Kalman filter. The filter weights its prediction with the covariance of the process noise. If the DIMM communicates an expected low variation (due to a moderate seeing), the filter will be adapted to predominantly reject higher variations, because these are assumed to be mainly contributions from measurement noise. A corresponding interface is foreseen in the current implementation of the filter algorithm, so once the DIMM is installed and working – as well as the FFTS and LINC-NIRVANA – this can be tested under realistic conditions. The look-up tables to evaluate the optimal covariances as a function of r_0 are obtained from the LOST simulations of the representative C_n^2 profiles of seeings 0.3", 0.7" and 1.5" (cf. Fig. 2.23).

2.6 Discussion

The presented simulation framework allows the investigation of residual piston and with it the overall performance of the LINC-NIRVANA instrument due to

control effects and system response. It is a important supplement to the considerations of the piston error budget due to the optical system (Herbst 2005).

Together with the atmoshperic simulations of LOST, a nearly complete system model is provided, from the arising of piston between the two apertures to the actual achievable piston compensation with the piston mirror. It emerged that many correlated parameters affect the performance, the best parameter setup depends on the actual observing conditions. Simulations of assumed conditions could help to set optimized parameters: which reference star should be picked? Which band is best-suited for tracking? Which is the optimal sampling rate as a trade-off between better SNR or more samples and better reconstruction? The generation of parameter tables is an ongoing process of estimation of optimal setups for specific observation conditions. More detailed look-up tables provide a better understanding of system responses.

A satisfactory solution of OPD compensation due to vibration is not achieved yet. More measurements have to be done, as the telescope's completion is advancing. The approach to realize real-time monitoring with phase information, might provide – if feasible – the easiest way of compensation. Definitely it will help to design more efficient vibration filters and (Kalman) estimators.

Optimal control is advisable for the non-linear PZT actuator, the intrinsic disturbance rejection is crucial for the system to avoid ruined science exposures, since telescope time is expensive. The hardware design might impose additional difficulties and effort, though. Further improvement of the controller design could involve advanced modeling with uncertainties, which provides additional robustness (Chen et al. 1999). $\mathcal{H}_\infty$ already avoids problems due to uncertainties at high frequencies by the proper weighting functions. Hence the modeling is not too critical at that regime, the need for precise measurements and modeling is relaxed.

The further development of the FFTS includes tests of software and control robustness in a realistic physical system. Several techniques, such as the image analysis including the PSF fitting, the software real-time concepts and the control approach have to be reconfirmed as part of the whole, complex system, before the integration of the FFTS into the LINC-NIRVANA instrument takes place. An overview of the testbed for this first integration phase is presented in the following section.
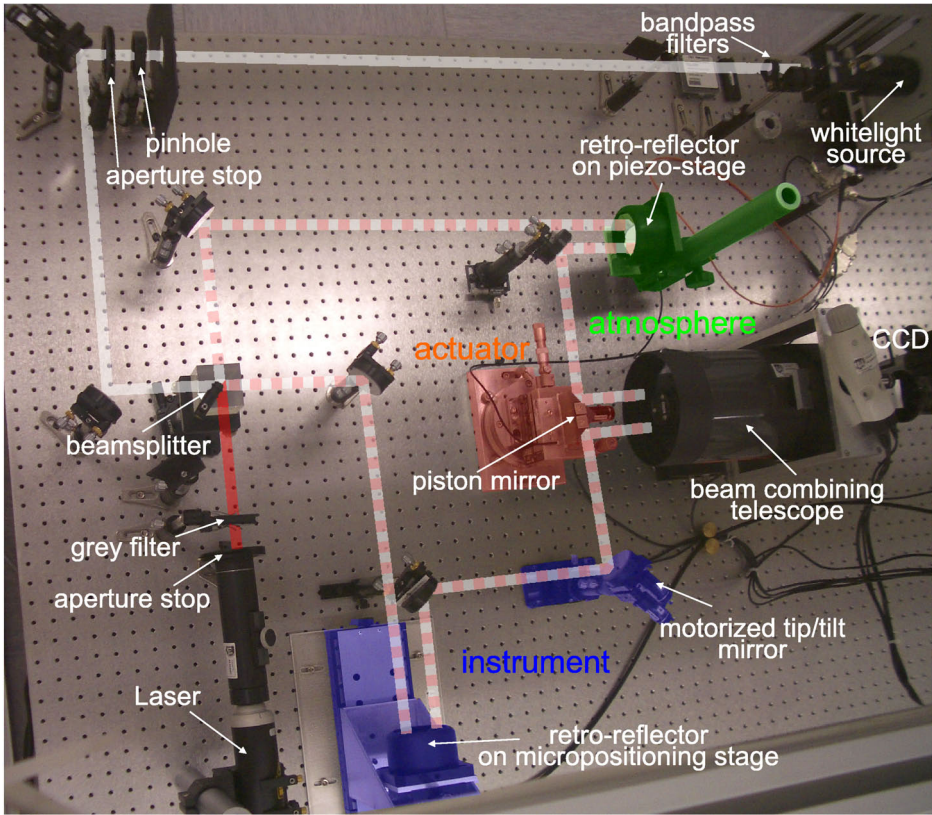
Figure 2.24: *Overview of the testbed interferometer in the laboratory.*
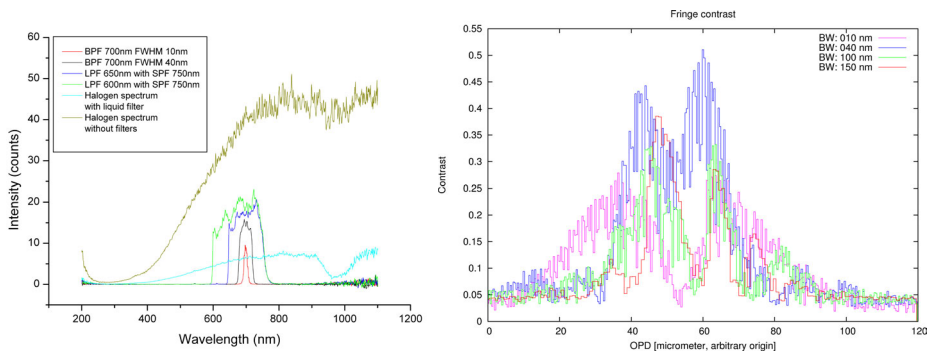

Figure 2.25: *Spectrum of the halogen lamp which is used as the white light source in the PSF simulator. Bandpass filters with different bandwidths have an impact on the number of fringes of the PSF. The fringe contrast is shown to the right, as a function of the OPD it is an indicator of the coherence length. The modulation is probably due to multiple reflections, e.g. at the beam splitter.*
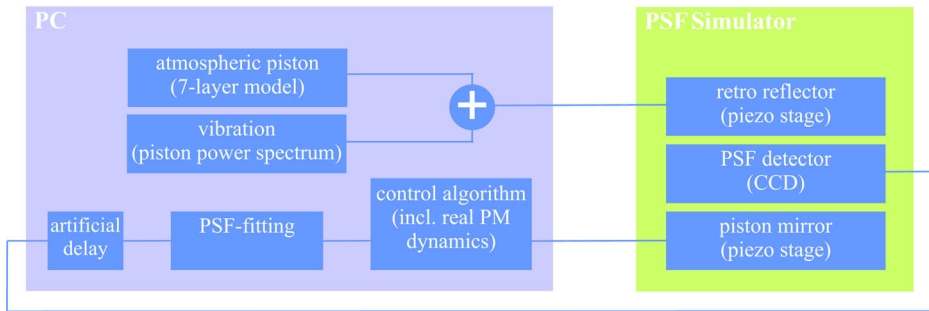
Figure 2.26: *Scheme of the PSF simulator system to simulate the FFTS performance. The distur-bances of the control signal are considered with the simulated atmospheric piston and the telescope vibration power spectrum. Additionally a realistic delay and PSF fitting noise is achieved in soft-ware. The hardware actuator and sensor are used in real-time to test the overall long-term stability of the system.*

2.7 Testbed interferometry

2.7.1 Overview

The integral components of the FFTS were reproduced on an optical bench in the laboratory. Figure 2.24 gives an overview of the setup. The light source is either a monochromatic *He-Ne* laser or a halogen lamp as white light source, several bandpass filters allow adjustments of the coherence length (Fig. 2.25). A beam splitter provides coherent beams to the two interferometric arms, after recombi-nation with a telescope a CCD delivers images with the PSF. The piston signal due to atmospheric and instrumental effects is generated with a retro-reflector on a PZT actuator. Low-frequent OPD, such as flexure effects can be induced by an additional micro positioning stage, which also allows scanning through the coherence length, e. g. to find the zeroth fringe. The piston mirror for OPD correction is also attached to a PZT, driven by a *Physik Instrumente* hardware controller (PID).

2.7.2 Simulation setup

The purpose of the testbed is to integrate the hardware and software in a system, which allows tests of the robustness of the fringe tracking concept. The current setup replicates nearly the complete hardware of the FFTS, as only the DPU is missing, and performance effects due to flexure and tracking errors of this de-vice can not be considered. The used CCD detector is slower ($\sim$ 30Hz) as the FFTS detector and has a different latency, but scaling of the system dynamics is possible (cf. Sect. 2.4.3). Piston sequences or a signal piston generated from a

specified temporal piston variation and vibrations according to the assumed vibration power spectrum can be introduced at the retro-reflector actuator. The two processes of introducing controlled OPD and the compensation in the PSF fitting loop are independent. Realistic detector conditions can be achieved by applying noise levels, exposure time variation, etc., to test the PSF fitting algorithm for arbitrary observation conditions (Fig. 2.26). The software of the system is the same as for the final FFTS, except the different hardware interfaces.

2.7.3 Outlook

After precise alignment of the setup fringes are detected as expected. First coherence length and scanning tests for the zeroth fringe determination revealed multiple reflections, which are not clearly identified yet (Fig. 2.25). The software development is in progress (cf. Figs. 1.14 and 1.15), but first piston tracking experiments are promising and confirm the consideration of sophisticated control techniques, i.e. optimal estimation of the noisy measurement, delay compensation by prediction and the optimal feedback control for the limited non-linear dynamics, which provides stability and disturbance rejection.

The testbed interferometer allows for the design and optimization of control approaches and stability tests of the software under realistic conditions, at the same time as the hardware construction and testing phase of the FFTS is initiated. This procedure will speed-up the integration process into LINC-NIRVANA and the final installation at the LBT.

Star formation in active H II regions

3.1 Theory of star formation

Many interesting infrared sources on the sky are associated with the birth of stars. Dense parts of molecular clouds collapse into proto-stars which are difficult to detect in visible light due to the surrounding material. In theories of star formation a distinction is drawn between low-mass and high-mass star formation with the border at $\sim 8 M_\odot$. Beyond this mass the radiation pressure is too high for spherical accretion. The fundamental conditions and process details differ in some important points. Several scenarios for formation processes exist, including that the high-mass star formation is supposed to be a scaled-up version of low-mass principles.

3.1.1 High-mass star formation

For massive stars ($M \gtrsim 8 M_\odot$, spectral types B3 and earlier) the processes are still not well understood due to both observational and theoretical difficulties (Krumholz 2006; Kissler-Patig et al. 2007; Brand 2007, e.g.). The frequency distribution of stellar masses at birth or the Initial Mass Function (IMF) has a broad peak at 0.6-1 $M_\odot$. In conjunction with the very short lifetimes – a 1 $M_\odot$-star lives about 2000 times longer than a 30 $M_\odot$-star – and heavy extinction during early evolution stages massive stars are very difficult to observe. High-mass stars are normally found in associations or in rich clusters so that star formation theories have to consider the influence of this surrounding. These massive star-forming clumps are detected as infrared dark clouds or as millimeter sources.

Stars with masses $\gtrsim 20\ M_\odot$ have short Kelvin-Helmholtz times

$$t_{KH} = \frac{Gm_\star^2}{RL} \tag{3.1}$$

so that the proto-star reaches the main-sequence while still accreting material from the surrounding cloud. Simple models imply that the resulting nuclear burning produces a radiation pressure large enough to prevent further accretion of material from gravity (Wolfire & Cassinelli 1987). More recent models therefore introduce non-spherical accretion via circumstellar disks (Yorke

2004). Disks concentrate the infalling gas at higher densities and act as a shield to the radiation pressure. An alternative is a scenario of merging small stars or "seeds" with an initial mass of $\sim 0.5 M_\odot$ in a dense molecular cloud. This can be achieved with collisions or spiralling in of binaries due to loss of angular momentum (Bonnell et al. 1998; Bonnell & Bate 2005). Finally the theory of competitive accretion is discussed, where the accretion rate is improved from the potential field of nearby stars (Bonnell & Bate 2006).

While lacking a robust theory massive stars play an important role in the evolution of galaxies. Their strong UV radiation ionizes the surrounding interstellar medium and forms active H II regions. During their short lifetime they induce turbulence and mixing of the ISM with stellar winds and massive outflows and ending in supernovae, which can also enrich the region with heavier elements. The environment can be destroyed by these giants so that no star formation is possible any more, but triggered (low- and high-mass) star formation is also observed (Healy et al. 2004; Zavagno et al. 2005).

3.1.2 Low-mass star formation

Theories of low-mass star formation are more evolved as the understanding of high-mass mechanisms. The accretion time is much shorter than the Kelvin-Helmholtz time $t_{acc} \ll t_{KH}$ (Eqn. 3.1), so the proto-star's luminosity is dominated by accretion.

Low-mass stars undergo a substantial evolution during the pre-main-sequence (PMS) in the Hertzsprung-Russell diagram (cf. Fig. 3.1). Lada (1987) introduced an observationally based classification (class I-III) of proto-stellar spectral energy distributions (SED) which was complemented by Andre et al. (1993) (class 0):

- class 0: The sources are not detectable or faint in the optical and NIR ($\lambda < 10\mu$), but sub-millimeter observations show significant flux. The mass of the envelope is higher than the mass of the proto-star $m_{env} \gtrsim m_\star$.

- class I: The SED shows a significant slope in the range between 2.2μ and 10μ. The evolved proto-star is surrounded by both a circumstellar envelope and a disk.

- class II: The now optical thick circumstellar disk dominates the SED in the range 2.2–10μ, the proto-star is in its pre-main-sequence. These sources are often referred to as classical T-Tauri stars (TTS), after the prototype in the constellation Taurus.
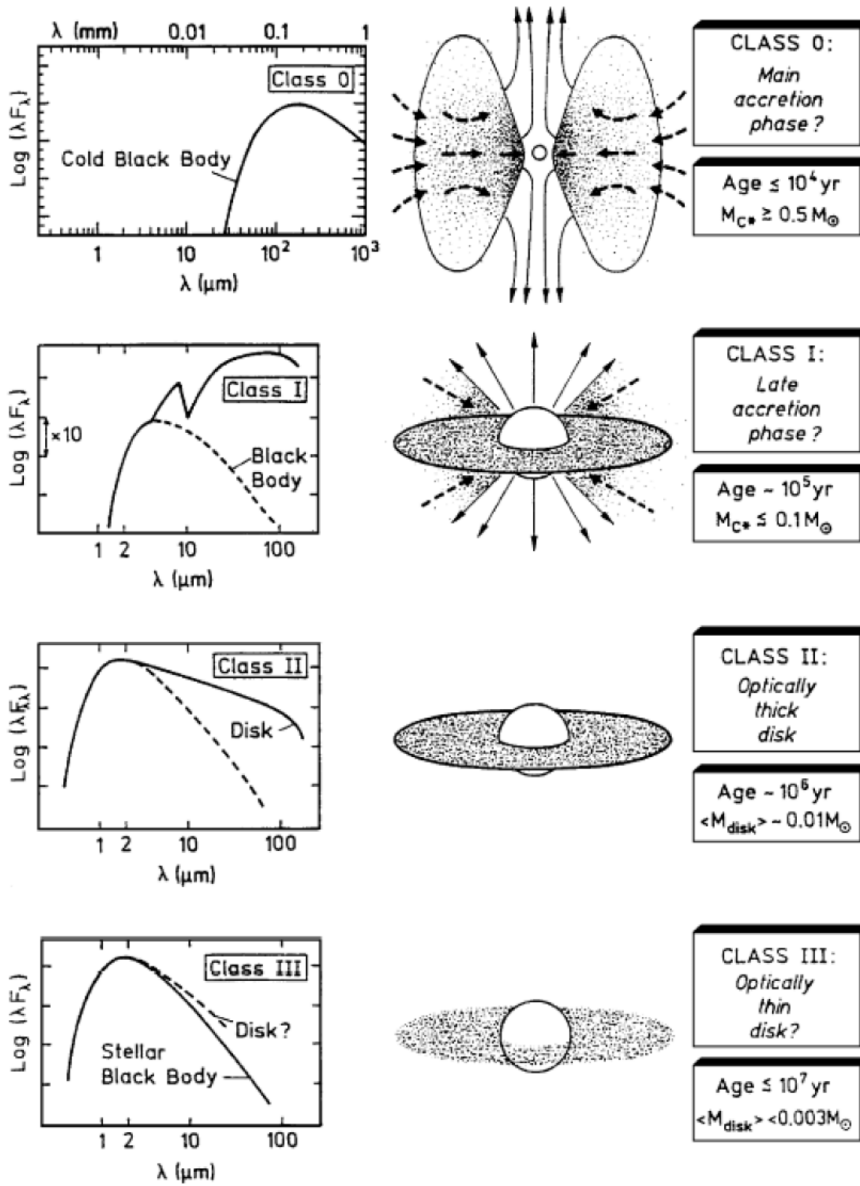
Figure 3.1: *The evolution stages of low-mass proto-stars, classes from O–III introduced by Lada (1987) and Andre et al. (1993). Left: Spectral energy distribution (SED). Middle: Disk and envelope configuration. Ages correspond to a solar-like star. (image credit: André 1994)*

- class III: The pre-main-sequence stars accrete no significant amount of matter any more, the SED is similar to a blackbody's SED. These sources are also named weak-line TTS.

The specific inclination of the disk of a source can thoroughly affect its classification. A specific configuration observed under low inclination angle may look like more than a class II proto-star, where the same system seen under high inclination would resemble a class I. With higher inclinations up to edge-on disks the central star is more and more obscured. Also flattened envelopes and cavities due to stellar outflows and jets can alter the classification.

A gravitationally bound core of an isothermal cloud collapses from hydrostatic equilibrium to a density profile $\rho \propto r^{-2}$. The rate of infall onto the star-disk system may differ from the accretion rate onto the proto-star by temporal storing of material in the disk. According to the standard theory (Shu et al. 1987) the infall rate depends on the effective sound speed by inclusion of magnetic fields and thermal pressure in the models ($c_I \gtrsim c_{sound}/2$). Other models include also turbulence and rotation. In case of a slowly-rotating, isothermal cloud with a settled core in quasi-equilibrium an inside-out collapse occurs (Terebey et al. 1984). The consideration of angular momentum – although the magnetic field can effectively cancel out angular momentum – leads to the formation of disks. The modeling of a proto-star with circumstellar envelope and disk is described in detail in chapter 5.2.

3.1.3 Circumstellar disks and planets

Disks appear to be ubiquitous in star-forming regions. The first evidence for disks around young stellar objects (YSO) were found in the Taurus dark cloud (Cohen 1983) at about 140 pc distance. The solid H_2O absorption and the CO emission of the disk provided the evidence. Later on disks were seen in IR and mm wavelength observations in both molecular and thermal emission. Most beneficial for the detections are the bright and easily seen reflection nebula, i.e. scattered light from circumstellar material illuminated from the stellar sources (Fig. 3.3). The outer regions of the disk are difficult to observe though, because the low flux and particles density.

Nowadays it is generally accepted, that the planets of our own solar system formed from gas and dust that collapsed to form the sun. No clear evidence for planet forming in disks was observed yet, but the number of detections of giant planets surrounding nearby stars is increasing steadily (at the time of the writing of this thesis 228 exoplanets are known, Butler et al. 2006; Angerhausen et al. 2007; Setiawan et al. 2008, e.g.).

3.1.4   H II-regions

Some of the brightest, most easily seen sources on the sky are associated with
H II-regions. They occur mainly in spiral arms of galaxies and in general where
star formation takes place, i.e. in regions with turbulent molecular clouds. The
luminosity is achieved by O and early B stars. If their UV radiation is signifi-
cant at energies > 13.6eV or wavelengths $\lambda < 912$Åthe hydrogen of the cloud
is ionized. By recombination with free electrons series of emission lines are ob-
servable. The Balmer series provides the prominent optical appearance of the
regions (Fig. 3.2). Typically several massive stars evolve close to each other
at the same time forming an OB association. The stellar wind of the OB stars
results in a shock front in the outer regions. The combined luminosity of the
association ionizes regions with sizes of up to hundreds of parsecs.

3.2   The Trapezium cluster

The Orion molecular clouds at a distance of about 440 parsecs[1] are the nearest
location of ongoing massive star formation. Lying in the relatively uncluttered
anti-center of the Galaxy, the Orion Nebula (M42) has been an important source
of astrophysical information since its discovery by Huygens in 1659. The vol-
ume density of the Orion Nebula Cluster (ONC) of more than 2000 stars per
cubic parsec is about 1000 times higher than a typical open cluster (McCaugh-
rean & Stauffer 1994). The so-called Trapezium is located at the very heart of
the Orion molecular cloud. The core of the ONC is known as the Trapezium
cluster, named after the constellation of four massive OB stars at its very center.
The dominant Trapezium star is θ^1 Ori C which generates most of the intense ul-
traviolet radiation field that photo-dissociates and photo-ionizes the surrounding
material.

Near-infrared (NIR) observations of the Trapezium cluster (Hillenbrand et al.
1998; Lada et al. 2000, 2004) have shown that most young stars have excess
emission in this wavelength regime. Hillenbrand et al. (1998) defined the color
excess by

$$\Delta (I_C - K) = (I_C - K)_{\text{observed}} - 0.5A_V - (I_C - K)_{\text{photosphere}} , \qquad (3.2)$$

where the first term is the observed color, the second term is the contribution
of reddening calculated from the extinction and the third term is the contribu-
tion of the underlying stellar photosphere including scattered light. An excess

---

[1]the precise value is under discussion, as measurements in a range from ∼380 to ∼500 pc are
presented (Jeffries 2007; Menten et al. 2007; Robberto 2005; Genzel et al. 1981; Genzel & Stutzki
1989)

Figure 3.2: HST ACS/WFC image of the Orion Nebula, the image is 30 arcminutes (4 parsecs) square. The colors are: F658N(H$_\alpha$) red/orange, F850LP and F776W red, F555W green and F435W blue (image credit: Robberto et al. 2005))

$\Delta(I_C - K) > 0.1$ is interpreted as the presence of circumstellar disks. According to the study by Lada et al. (2000), ~80% of the stars in the Trapezium cluster are surrounded by disks.

Currently much activity is devoted to obtain physical properties of the circumstellar dust distribution and these disks. Olczak et al. (2006) showed that encounters of stars and circumstellar disks in the Trapezium cluster are quite frequent and thus can cause a considerable contribution to the mass loss and the truncation of proplyds. Encounter-triggered planet formation might also be possible as an important supplement to triggering by super massive stars (Bally
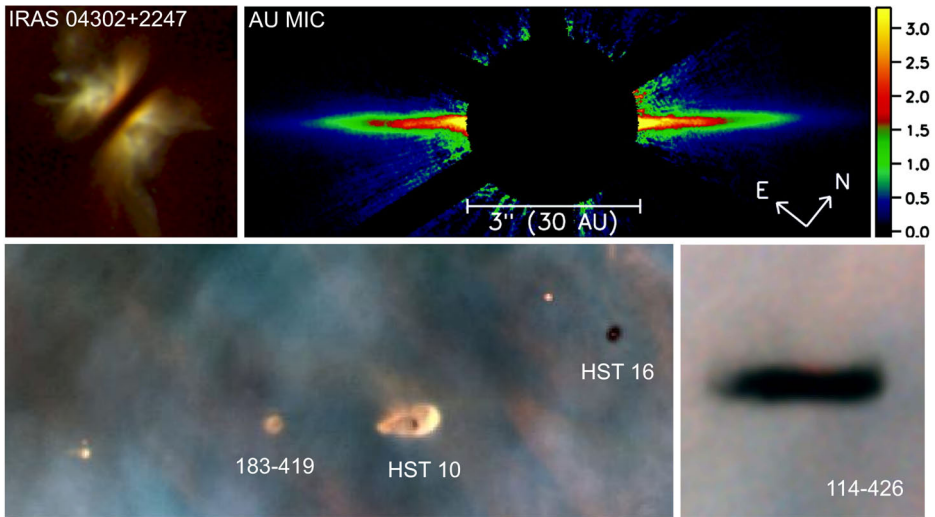
Figure 3.3: *Circumstellar disks. Upper left: Near-Infrared view of class I disk around IRAS 04302+2247. The light from the star is only seen as reflection from the surrounding nebula, the edge-on disk is visible as a dark bar. Upper right: The debris disk (class III) of AU Microscopii at 0.04" resolution, Keck II NIR image. Bottom: representative disks in Orion. HST 10 (182-413) is surrounded by the typical tear-drop IF, but also the disk is seen in silhouette. HST 16 (183-405) has a face-on disk, the central star is visible. The giant disk of 114-326 (∼1200 AU) is seen edge-on, the star is seen indirectly through reflection.*

2003; Lee & Chen 2007) and supernovae-triggering of the OB-stars (Hester & Desch 2005). The disks of the proplyds close to the Trapezium with a typical radius of 20–80 AU are not resolvable directly.

3.3 The Orion proplyds

After the successfully correction of the Hubble Space Telescope's optics in 1993 a series of brilliant optical images of the Orion nebula were taken (O'Dell & Wen 1994). The discovery of proto-planetary disks (proplyds) in this region by O'Dell et al. (1993) with the HST has provided an unprecedented opportunity to study planet-forming disks around young stars. These objects are surrounded by bright, crescent, and tear-drop shaped ionization fronts (IF) resulting from gas flow off of the disk. At greater distances and shielded from radiation, several proplyds without ionization front have been observed. They are seen in silhouette against the bright nebular background (Bally et al. 2000). The detections of silhouette disks in Orion are the largest sample of disks yet.

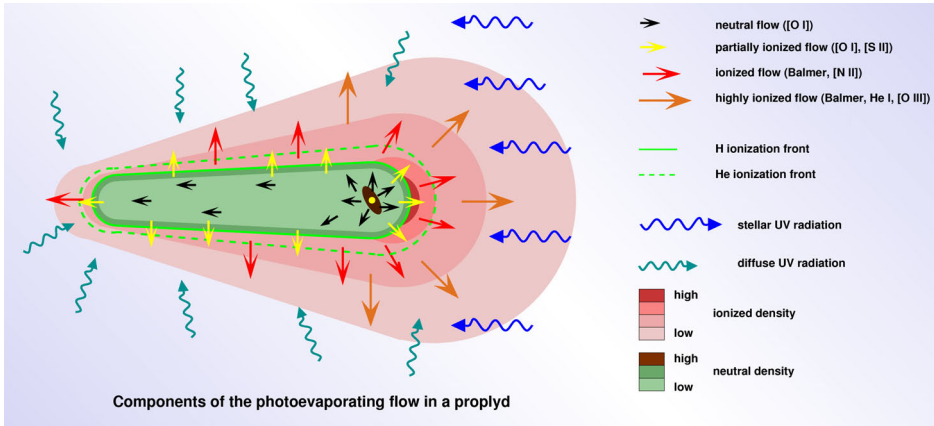The illumination of the H II-region from the Trapezium stars is helping the

Components of the photoevaporating flow in a proplyd

Figure 3.4: *Components of the photo-evaporating flow in a proplyd (image credit: Henney & O'Dell 1999).*

observer to detect disks and clearly defines edges of the disk, as opposed to reflection nebula illuminated from the central star, because of the low flux and density of particles in the outer regions (Fig. 3.3). On the other hand the impact of the Trapezium on the Orion disks is of a more destructive nature. The strong UV-radiation is removing rapidly gas and dust from the disks. The lifetimes of the disks due to the photo-evaporation could be as low as 10^5 years (Johnstone et al. 1998). Many disks may already be destroyed, others may be far enough away from θ^1 Ori C to avoid the process, but the majority of disks is strongly affected.

The typical proplyd has a mass of $0.01 M_\odot$ and a diameter of 200 AU, though the variation in size is large (50-1200 AU). In the Orion nebula the YSO 177-341, also known as HST1 is one of the best studied proplyds because of its large size and orientation (Bally et al. 1998; Henney & O'Dell 1999; Henney 2000). The very bright ionization front outshines details of its inner structure.

New insights into the nature of proplyds have been acquired through high-resolution multi-spectral imaging with HST (Bally et al. 1998), follow-up imaging, and spectroscopy at a variety of wavelengths from the ground, and intensive theoretical modeling (Johnstone et al. 1998; Störzer & Hollenbach 1999, e.g.). As a result, an irradiated disk model has been developed to account for the presently known observed features (Fig. 3.4). For proplyds within 0.3pc of the Trapezium, the mass loss caused by photo-evaporation can eventually completely erode a typical proto-stellar disk (Johnstone et al. 1998). The time scale for this disruptive process would be $10^4 - 10^5$ years, slightly less than the median age of the ONC ($3 - 10 \times 10^5$ yr Hillenbrand et al. 1998). The estimated mass

loss depends on assumptions about the opacity of grains, whereas little is known about the morphology and chemistry of the disks themselves. Since simulations suggest substantial growing of grains with time the inferred mass loss of the proplyds due to photo-evaporation may be significantly overestimated (Throop et al. 2001).

According to a model of the eroding disk mechanism (Bally 2003) first the outer parts of the disk are being destroyed. One way for disks to survive the photo-evaporation by UV-radiation is if dust grains grow to sizes with radii $\gtrsim$ 1cm. Evidence for grain growth in circumstellar disks in Orion has previously been found, the outer portions of the giant disk of 114-426 contains grains $\gtrsim 2\mu m$ (Shuping et al. 2003). The efficiency of grain growth is predicted to be highest in the center of the disk where the highest densities and temperatures are found and photo-evaporation does not operate efficiently (Throop et al. 2001).

3.4 Unsolved problems

There are several open questions concerning the Orion proplyds, such as the calculation of the mass loss rate due to photo-evaporation, which is strongly model dependent and implies severe restrictions to the proplyds age (Clarke et al. 2007). A possible scenario is that the OB association is very young and the evaporation process has just begun. Another suggestion is, that the proplyds are traveling through the UV-dominated region on a large orbit in the OMC. Therefore the disks will be exposed to the destroying UV radiation for a short time only. However, for the possibility, that the disks can survive to some extend and planets can built up an additional mechanism must be present. Grain growth in the disks is predicted by several models (Throop et al. 2001) and also supported by observational results (Shuping et al. 2003). But it remains unclear, whether the process can be fast enough to overcome the destroying influence of the surroundings. As our own solar system shows a substantial occurrence of heavy elements which are not produced by first-hand nuclear processes the question arises, wether super-nova remnants from the ionizing OB association could induce such material in truncated disks and already formed proto-planets (Fig. 3.5).

Recently there were great scientific efforts in understanding star formation and the reconstruction of the history of our own Solar System. Theories put this in context to observable star formation regions, considering evidences that the Sun formed near a massive star (Hester & Desch 2005). If OB-stars with a expanding H II-region and ionization shock front trigger low-mass star formation in a molecular cloud, several interesting questions arise: Is enough time for grain
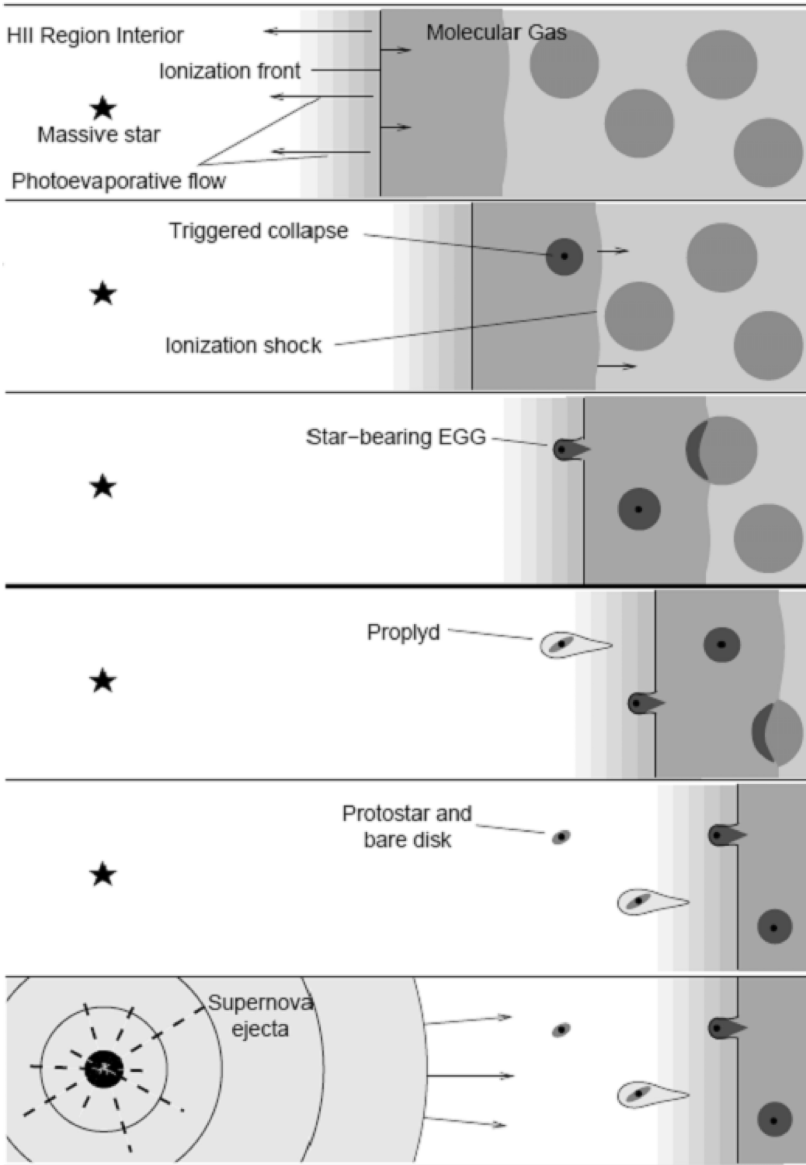
Figure 3.5: *Scenario of triggered star formation: The ionization front of high-mass stars triggers low-mass star formation. During the short lifetime of the massive stars most of the circumstellar material is photo-evaporated, but with their end as a super nova heavy elements can be induced in the disks and planet formation without further disk erosion is possible (image credit: Hester & Desch 2005).*

growth in the circumstellar disk before the UV-radiation evaporates all gas and dust? Is the (bright) proplyd phase short and planet formation possible in a truncated disk similar to the size of the Solar System? Are heavier elements later injected by supernovae of these triggering OB-stars?

Also it is known that many proplyds show the presence of high-velocity kinematic features such as large outflows and jets. Recent studies Vasconcelos et al. (2005) with integral-field spectroscopy in the optical showed e.g. for the 167-317 proplyd different kinematic components ranging from 28-33 km s^{-1} for the photo-evaporated flow to 80-120 km s^{-1} for jets, resulting in a very complex structure of a proplyd. Appart from photo-evaporation gravitational interactions can lead to disc mass loss. Olczak et al. (2006) showed that encounters of stars and circumstellar disks in the Trapezium cluster are quite frequent due to the very high stellar density in this area. This can cause a considerable contribution to the mass loss and the truncation of proplyds.

NIR imaging polarization observations

4.1 SHARP/ADONIS data

The ESO 3.6m Telescope is located on top of the 2400-m mountain La Silla (the saddle) in the southern Atacama desert. The telescope had seen first light in 1976 and was completely upgraded in 1999. ADONIS (Beuzit et al. 1994) is an adaptive optics (AO, for an overview see chapter 1.3.3) system at the 3.6m telescope and was operated between 1993 and 2002. It is the successor of COME-ON and COME-ON+, which were the first routinely used AO systems for astronomical observations. Reference wavefront sensing is achieved in the visual with two Shack-Hartmann sensors, one for bright reference stars, the other optimized for fainter stars.

SHARP II+ is a near-infrared camera (Hofmann et al. 1992) built at the Max-Planck-Institut für extraterrestrische Physik (MPE). It was specially designed to operate with ADONIS, profiting from the experience gained with the predecessors SHARP I (at the NTT) and SHARP II. SHARP II+ is based on a Rockwell NICMOS-3 array (see also Fig. 1.12) for diffraction limited imaging in the spectral range from $1.1\mu m$ to $2.45\mu m$. The $HgCdTe$ detector was originally developed for the NICMOS instrument of the Hubble Space Telescope (HST) and has to be cooled with liquid nitrogen for operation to reduce thermal noise.

Table 4.1: *Specifications of the NICMOS-3 detector of the SHARP/ADONIS instrument*

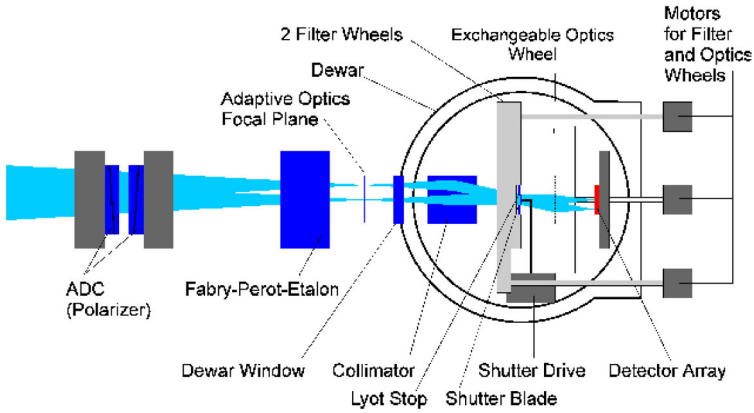|	
number of elements	256×256
	4 quadrants 128×128 each
pixel-size	$40\mu m \times 40\mu m$
FoV at 100 mas platescale	25.6"× 25.6"
FoV at 50 mas platescale	12.8"× 12.8"
FoV at 35 mas platescale	8.96"× 8.96"

Figure 4.1: *The SHARP II+ camera system*

Table 4.2: *Broadband filter central wavelength and bandwidth of SHARP II+ and of the 2MASS catalog*

filter	SHARP II+		2MASS	
	λ [μm]	bandwidth [μm]	λ [μm]	bandwidth [μm]
J	1.253	0.296	1.235	0.162
H	1.643	0.353	1.662	0.251
K_S	2.154	0.323	2.159	0.262

4.2 Polarimetry

4.2.1 Stokes parameters

Sir George Stokes introduced 1852 a set of parameters to describe polarized light, which are commonly used nowadays. A simple electromagnetic wave of a single photon can be expressed by components of the electric vector E (van de Hulst 1957)

$$
\begin{aligned}
E_x &= E_{0x} \sin(\omega t - \phi_x) \\
E_y &= E_{0y} \sin\left(\omega t - \phi_y\right)
\end{aligned}
\tag{4.1}
$$

where E_x and E_y are the amplitudes and ω the angular frequency of the transverse electromagnetic wave perpendicular to the direction of propagation. The polarization can then be classified as follows: in general the phases ϕ_x and ϕ_y are not equal and the wave is elliptically polarized. If $\phi_x \neq \phi_y$, but $E_{0x} = E_{0y}$, the wave is said to be circularly polarized and the electric vector E is rotating with constant amplitude in the x-y-plane. With respect to the direction of rotation

the wave can be classified as right-handed or left-handed circularly polarized. The wave is linearly polarized, when $\phi_x = \phi_y$ and the angle of polarization is determined by the ratio E_{0y}/E_{0x}. The Stokes parameters are defined as follows:

$$
\begin{aligned}
I &= & \left\langle E_{0x}^2 \right\rangle + \left\langle E_{0y}^2 \right\rangle \\
Q &= & \left\langle E_{0x}^2 \right\rangle - \left\langle E_{0y}^2 \right\rangle \\
U &= & 2 \left\langle E_{0x} E_{0y} \cos\left(\phi_x - \phi_y\right) \right\rangle \\
V &= & 2 \left\langle E_{0x} E_{0y} \sin\left(\phi_x - \phi_y\right) \right\rangle
\end{aligned}
\tag{4.2}
$$

The ratio

$$
\Pi_L = \frac{\sqrt{Q^2 + U^2}}{I} \tag{4.3}
$$

is called the polarization degree and

$$
\Pi_e = \frac{|V|}{I} \tag{4.4}
$$

the degree of ellipticity. The angle of linear polarization is expressed as

$$
\theta = \frac{1}{2} \arctan \frac{U}{Q} \ . \tag{4.5}
$$

In the case of astronomical observations with a wollaston prism polarized intensity images are commonly taken at the four angles I_0, I_{45}, I_{90} and I_{135}. In this case the Stokes parameters can be expressed as

$$
\begin{aligned}
I &= & I_0 + I_{90} \\
Q &= & I_0 - I_{90} \\
U &= & I_{45} - I_{135} \\
V &= & 0
\end{aligned}
\tag{4.6}
$$

Only the linear polarization is measured, so that $V = 0$. To determine also the elliptical part of the polarized light, an additional $\lambda/2$-wave plate is needed.

The definition of the Stokes parameters as noted in 4.6 is not fix in the literature and varies e.g. in the angles used, because the two independent angles are arbitrary as long as they span at least 90°. Also the direction in which the angle ϕ is counted varies (van de Hulst 1957). This means one has to carefully use the equations by comparing the definitions of different authors and using a consistent formalism.

If the coordinate system is rotated counterclockwise by an angle ϕ, only the Stokes parameters Q and U are affected. The transformation is, therefore, described by (Chandrasekhar 1950)

$$\begin{pmatrix} I' \\ Q' \\ U' \\ V' \end{pmatrix} = \begin{pmatrix} 1 & 0 & 0 & 0 \\ 0 & \cos 2\phi & \sin 2\phi & 0 \\ 0 & -\sin 2\phi & \cos 2\phi & 0 \\ 0 & 0 & 0 & 1 \end{pmatrix} \begin{pmatrix} I \\ Q \\ U \\ V \end{pmatrix}. \tag{4.7}$$

With this transformation ist is possible to calculate Q and U parameters as defined in 4.6 from polarization images at other angles. If images were taken e.g. at $0°$, $90°$ and two additional angles ϕ and $\phi + 90°$ we have a dataset I_0, I_{90}, I_ϕ and $I_{\phi+90}$ and pseudo-parameters can be written as

$$\begin{aligned} Q_0 &= I_0 - I_{90} \\ Q_\phi &= I_\phi - I_{\phi+90} \end{aligned} \tag{4.8}$$

Then we can insert the given parameters in equation 4.7, i.e. $Q' = Q_0$, $Q = Q_\phi$, $I' = I$ and since we measure only linear polarization $V' = V = 0$. Now 4.7 gives

$$\begin{aligned} Q' &= Q_\phi \cos 2\phi - U_\phi \sin 2\phi \\ U' &= Q_\phi \sin 2\phi + U_\phi \cos 2\phi \end{aligned} \tag{4.9}$$

Cancelling U_ϕ gives then

$$U' = \frac{Q_\phi - Q' \cos 2\phi}{\sin 2\phi}. \tag{4.10}$$

4.2.2 Polarization in astrophysics

Near-infrared polarimetry is a proven remedy for mapping hidden effects and structures (see, for example, Ageorges et al. 1997; Meyer et al. 2006). Monin et al. (2006) showed that polarimetry can be used to trace the relative orientation of discs in young binary systems. The polarization structure of a massive young stellar object (YSO) in OMC-1 revealed a surrounding disk/bipolar outflow system (Jiang et al. 2005). In the case of dust around a bright star, only the scattered light from the disc is expected to be polarized, the unpolarized light from the central star is suppressed by differential polarimetric imaging (PDI). Therefore this technique can improve the contrast and the detection-threshold, and it provides a possibility to map structures very close to bright stars without coronographic masks (Kuhn et al. 2001; Hales et al. 2006). Polarimetric images can also trace the sources of illumination of the reflection nebula in star forming regions (Hashimoto et al. 2007). In the following mechanisms are discussed that produce polarized light which is detectable with telescopes.
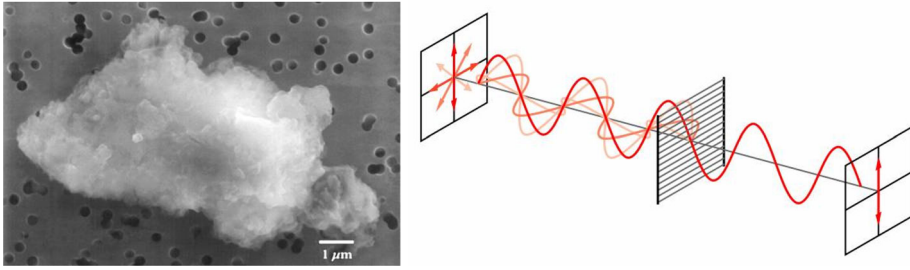
Figure 4.2: *There are multiple origins for the polarization of incident light on the detector of a telescope. Left: scattering by stellar grains. Right: wire grid polarizer in the polarimetric instrument.*
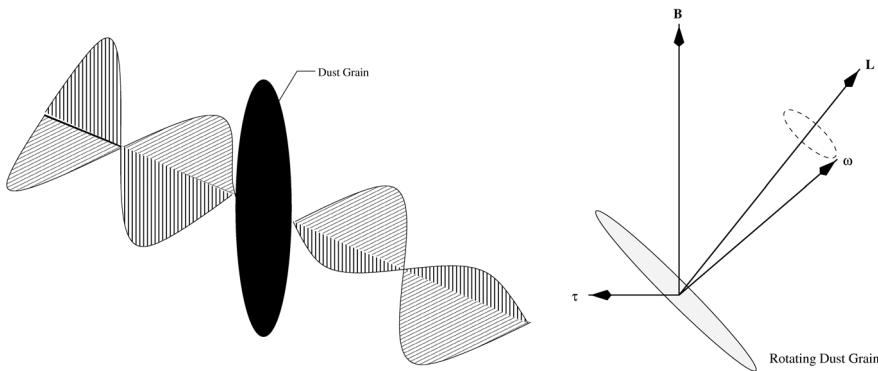

Figure 4.3: *Left: The electric vectors from unpolarized light suffer different in the extinction in the direction parallel and perpendicular to the long axis of the dust grain. For a reasonable amount of detectable polarized light the grains have to be aligned, e.g. by a magnetic field (right).*

Dichroic extinction

Polarization from dichroic or selective extinction results from the extinction of light with a preferred orientation of the electrical vector. In general the incident light on a dust grain is unpolarized with no preferred orientations. If the grain is spherical, than every wave with arbitrary electric vector will be scattered or absorbed in the same way. However, if the grain is not spherically symmetric, e.g. prolate or oblate ellipsoids, the absorption of the wave will depend on its orientation of the electric vector (Fig. 4.3). If the vector is parallel to the long axis of the grain the wave will suffer a greater extinction. In general prolate grains have no preferred orientation, so the effect will be cancelled out. An additional mechanism of grain alignment is therefore needed to produce a significant amount of

polarized light. Davis & Greenstein (1951) proposed paramagnetic relaxation in rapidly spinning grains resulting in a torque in magnetic fields (Fig. 4.3). Observations indeed showed that aligned polarization vectors are perpendicular to the galactic magnetic field.

Scattering

The intensity and polarization of scattered light depends on the size of the scattering particle and the wavelength of radiation. Precisely, the size of the scattering cross section is relevant, not the physical cross section. Also the spectral extinction is determined by the particle's physical dimensions.

As of a sufficient complex nature, the scattering of electromagnetic waves is divided in different classes. Inelastic scattering (Raman, Brillouin and Compton scattering) plays a minor role in astrophysics, because the major fraction of scattering is elastic with negligible energy transfer. Nevertheless it has been tried to use these effects as sensitive diagnostic techniques (Nussbaumer et al. 1989; Sandoval-Villalbazo & Maartens 2005, e.g.). In contrast to this, elastic scattering is a very common occurrence in astronomy. The character of scattered and polarized light is dependent on the size of the particle.

Mie scattering is the analytical solution of the Maxwell's equations for the scattering by spherical grains in general (van de Hulst 1957). If the particles are small with respect to the wavelength, the Mie solution reduces to the Rayleigh approximation. In figure 4.4 an example of the Mie solution for different wavelength is shown indicating a complex spatial and spectral structure. By moving to the Rayleigh regime with higher wavelength the scattering is becoming more isotrope. Comparisons of the single-scattering phase functions are given in chapter 5.1.3. Also scattering by aligned nonspherical grains in contrast to dichroic or differential extinction/emission occurs.

Other Origins

Polarization is present in radiation from coherent sources such as masers (Kemball 2002), providing a useful analysis technique to study magnetic fields. Another effective emitter of polarized light is a black hole (Meyer et al. 2006). Synchrotron radiation is inherently polarized and the immediately vicinity of the black hole is observed with very high degrees of polarization. The polarization of the cosmic microwave background is studied to achieve new insights in cosmology and early universe physics (Prunet 2007).
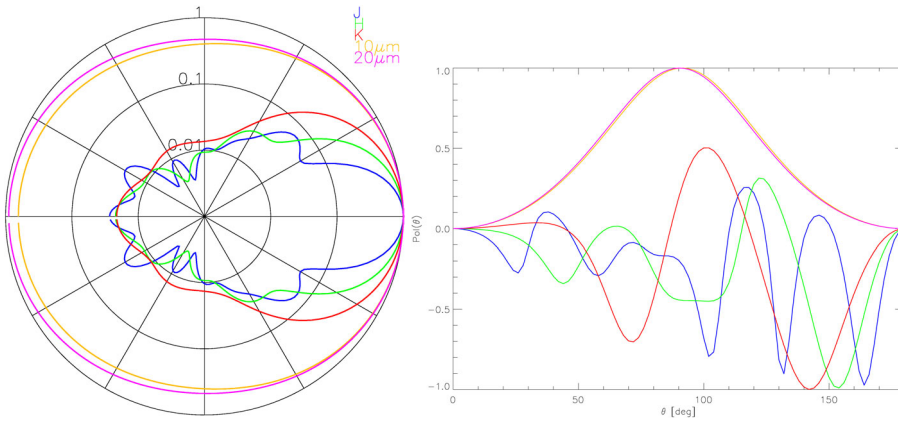
Figure 4.4: *Left: Radial plot of the Mie scattering pattern for a perfect sphere with diameter 2.2μm. The normalized magnitude is plotted logarithmic (radial) to show the side lobes of the computed Mie solutions. For greater wavelengths the scattering becomes less anisotropic and converges to Rayleigh scattering. Right: Polarization degree as function of the scattering angle. Negative values mean polarization in the plane parallel to the incident and scattered ray dominates, where positives refer to the perpendicular plane's polarization.*

Circumstellar Dust

It is very likely that due to Mie scattering in an extended, asymmetric dust shell around the proplyds, an excess in polarization can be measured. This phenomenon is also observed in a number of Galactic bipolar outflow sources. Due to the current distribution on dielectric dust grains that have circumferences comparable to the incident radiation, polarized light is scattered perpendicular to the line of sight between the radiation source and the dust grain. If the dust is evenly circular symmetrically distributed around the star, no integrated polarization is observed. If, however, this symmetry is broken in the form of an almost edge-on disk, a bipolar outflow or any other kind of non-spherical symmetric distribution, this results in a net polarization typically ranging between 10% and 30% of the integral near-infrared flux. Irrespective of whether the extended Orion Trapezium disks are illuminated from the outside (outer parts of the disks seen as silhouettes) or from the inside (inner sections of the disk) by the central star a significant amount of polarized flux can be mapped. Dependent on the size of the grains and therefore the wavelength λ_{max} of maximum scattering efficiency, higher degrees of polarization either in the K- or the J-Band will be observed. Spatially resolved polarization maps in different bands may be suitable to determine the increase (or decrease) of grain sizes towards the central source, taking into account the effects of extinction and hot dust emission. This will help to bet-

Table 4.3: *Specifications of the SHARP II+ polarizer*

substrate	Calcium Fluoride (CaF_2)
spectral range	1-9 μm
grid period	0.25 μm
transmission for $pol_\perp$ (1.5 μm)	83%
transmission for $pol_\parallel$ (1.5 μm)	3%
degree of polarization (1.5 μm)	93%

ter understand the history of the formation of the disks and gives a first insight into disk geometry and scattering mechanisms of the dust grains.

In the case of single scattering, heavily obscured stellar sources can be located using the structure of the spatial distribution of polarization position angles (e.g. Ageorges et al. 1996), even though they might not be visible in the integrated images due to extinction. Yet, if the central source is seen, a shift between the intensity peak and the polarization center as a function of wavelength will also indicate nonuniform and/or patchy extinction.

4.2.3 SHARP/ADONIS polarizer

The SHARP polarizer is a wire grid on a Calcium Fluoride substrate (Tab. 4.3). When the polarizer is rotated, a small shift of the image occurs. This has to be considered in the data reduction, if images with different polarizer settings are combined. Polarimetric calibrations require the observation of an unpolarized reference star.

It is known from ADONIS observations that the adaptive optics correction has a different response when guide stars with deviating brightnesses are used. This results in variation of the Strehl ratio and the deconvolution of extended sources with PSFs obtained from other stars than the guide star must be done carefully. In general stars with similar magnitude to the science target should be chosen as PSF calibration stars. The same should apply to polarimetric calibration stars.

4.3 NIR imaging

4.3.1 Observations

A JHK polarimetry survey of selected proplyds in the Trapezium Cluster was carried out to study dust and disk parameters in this dense star-forming region.
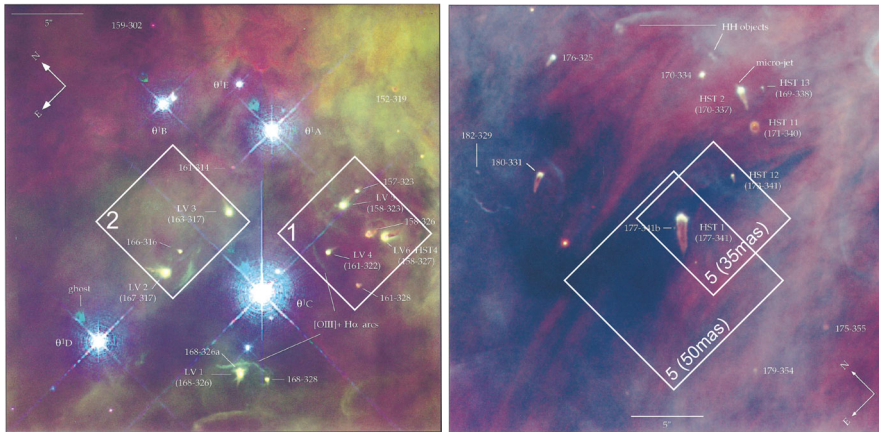
Figure 4.5: *HST optical images of the Trapezium region (red is [N II], green is H$_\alpha$, blue is [O I], Bally et al. 1998). For pointing 1, 2 and 5 of the SHARP/ADONIS observations the field of view is marked, the image to the right is centered about 25" south-east of the Trapezium.*

Disks of the proplyds close to the Trapezium that have a bright IF are so far only seen as IR excesses. With the polarimetric images the circumstellar dust distribution can be mapped and parameter ranges for the disks extracted to classify the Trapezium proplyds.

High-resolution near-infrared polarimetric images were acquired in 2001 with the ESO Adaptive Optics System ADONIS and the SHARP II+ camera at the La Silla 3.6m[1] telescope (Ageorges & Walsh 1999). The rotating wire grid polarizer provided polarization angles from 0° to 150° with a 30° increment. The sources are 10 proplyds close to the Trapezium stars, embedded in three pointings with a field-of-view (FoV) of 8.96"×8.96" and a 0.035" plate scale. Images were taken over three nights in J, H, and K bands. No occulting masks were used in these observations due to multiple sources per FoV.

A problem of observations of circumstellar material is the high dynamic range that is needed. The stellar flux will saturate the detector in most cases, before the signal-to-noise ratio (SNR) of the emission of the dust is high enough. This is commonly solved by coronographic masks, which block the central light. This technique induces some other problems though, e.g. diffraction spikes from the support structures and alignment effects (Schütz et al. 2004). The chosen detector integration time for a good SNR and dynamic range was 15 s per polarization angle and FoV. With this setup the brightest targets are slightly saturated in the frames, meaning that for the highest fluxes the detector is driven beyond
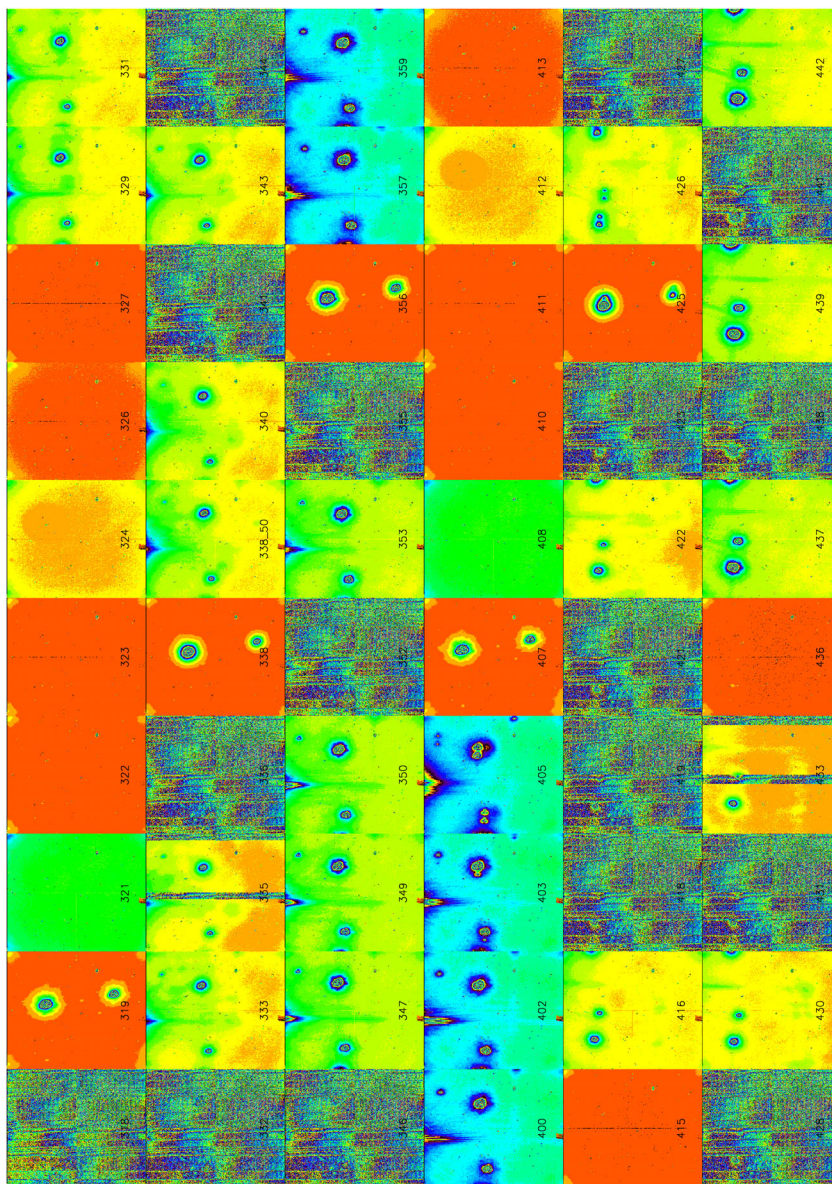
---

[1]ESO program-ID: 066.C-0219

Figure 4.6: *This excerpt from the SHARP/ADONIS imaging data set emphasizes some of the problems dealt with in the data reduction. Shown are different parts of the observation: pointing 2 with the targets (e.g. frame 329), PSF and calibration stars (319), sky frames (321 and following). There are a number of broken frames and also frames with broken regions due to problems with the camera readout electronics (355, 453). The flat-field is varying as a consequence of insufficient cooling and hot spots on the detector (324, 412). The FoV is limited and some sources are not covered in all frames (compare 347 and 437). Last but not least the AO-loop was not perfectly working and produced residual speckles or even crashed completely in particular frames (405).*
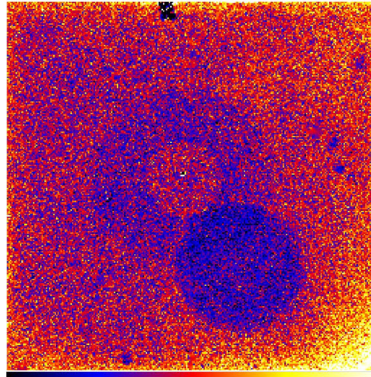
Figure 4.7: *Flat-field of the SHARP detector in J-band. The intensity of the artefacts is varying in time. The annulus shaped feature is likely due to vignetting by the optics, the off-axis spot could be a cooling problem of the detector ("hot-spot").*
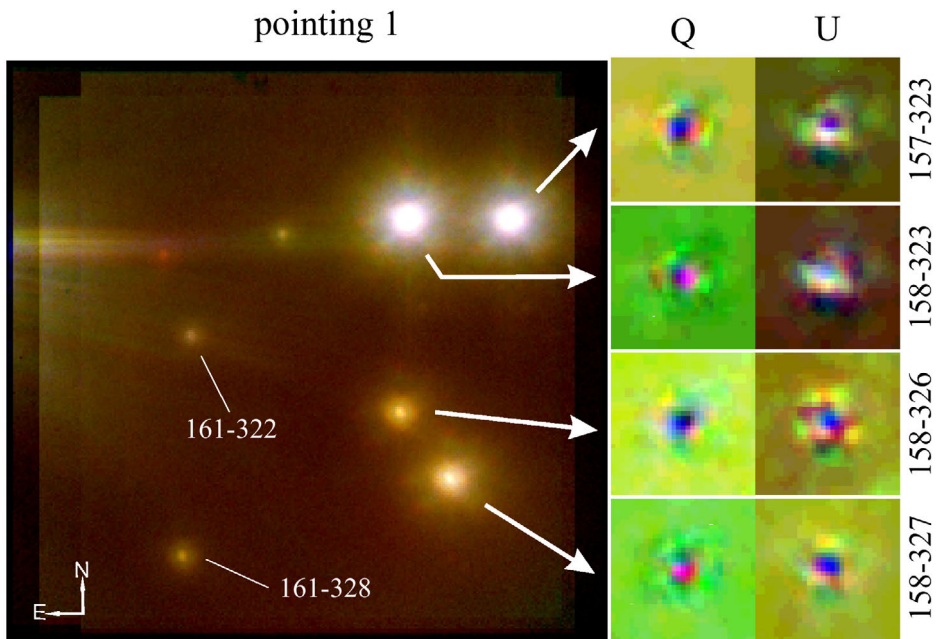
Figure 4.8: *Color composite (KHJ ≡ RGB) of pointing 1, as shown in Fig. 4.5. The FoV is 8.96"×8.96", while the Q- and U-image sizes are 2.1"×2.1". The polarimetric differential images (PDI) of most of the sources show a trefoil which is supposed to be an AO-effect, but other optic aberrations like astigmatism can occur additionally.*
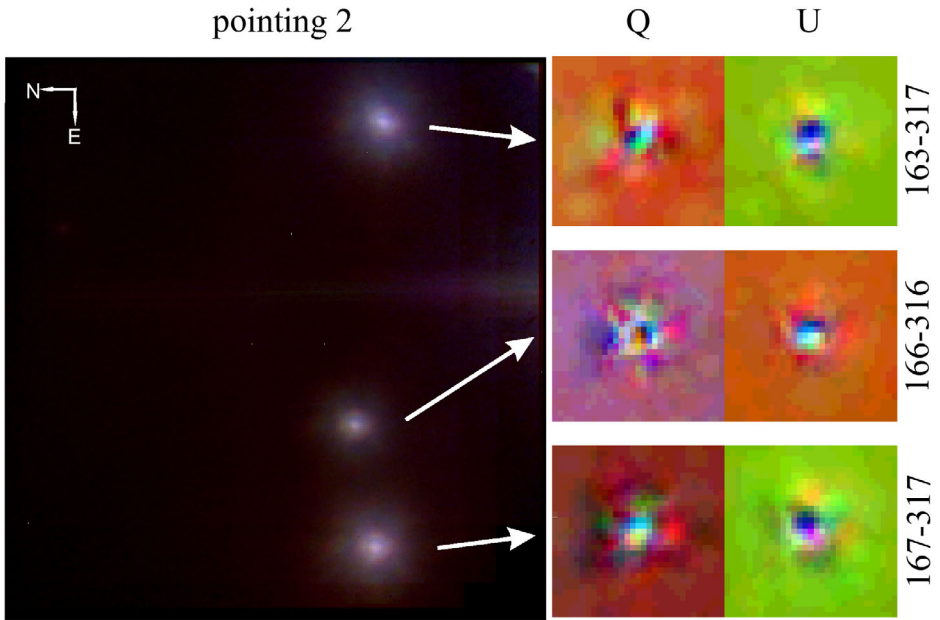
Figure 4.9: FoV of pointing 2 and Stokes images of the proplyds.
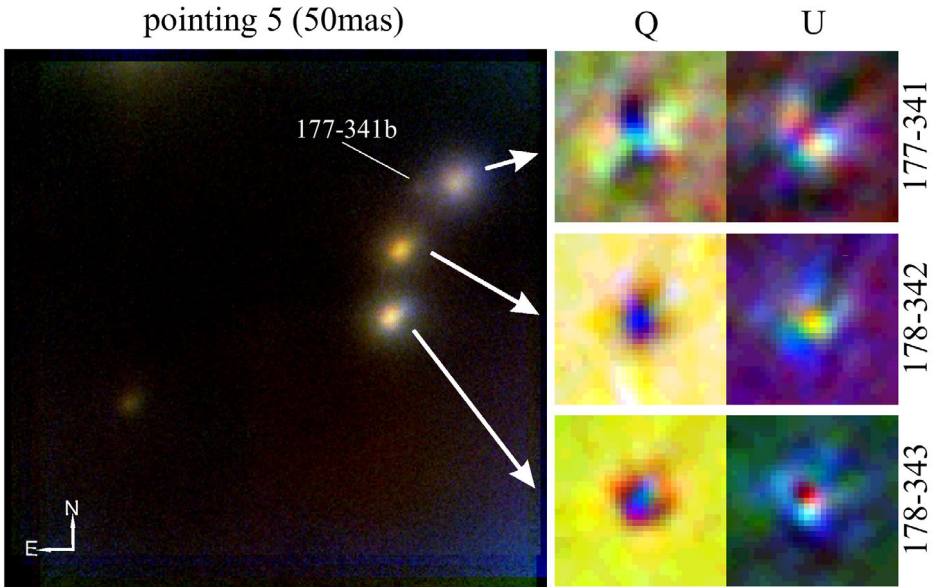
Figure 4.10: FoV of pointing 5 with 50 mas platescale (12.8"×12.8" FoV) and Stokes images of the proplyds. The proplyd 177-341 shows a butterfly pattern in all bands. Remarkable is a elongated dark feature with a position angle (P.A.) of about 135° in the U-image of 177-341.
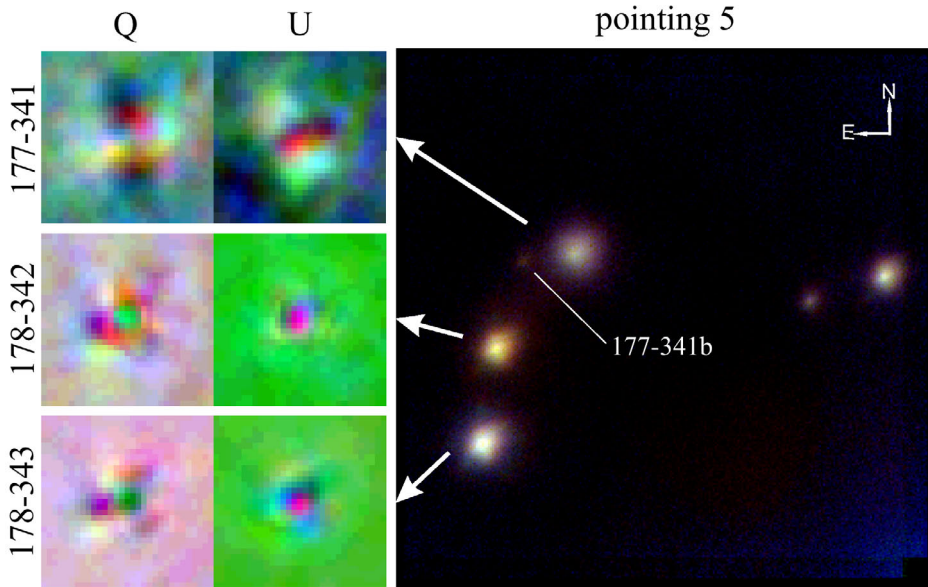
Figure 4.11: *FoV of pointing 5 with 35 mas plates scale and Stokes images of the proplyds. The sources of figure 4.10 are observed both with 50 and 35 mas platescale. This provides a cross check to the observed pattern of 177-341 and artefacts of the reduction process can be excluded as the origin.*
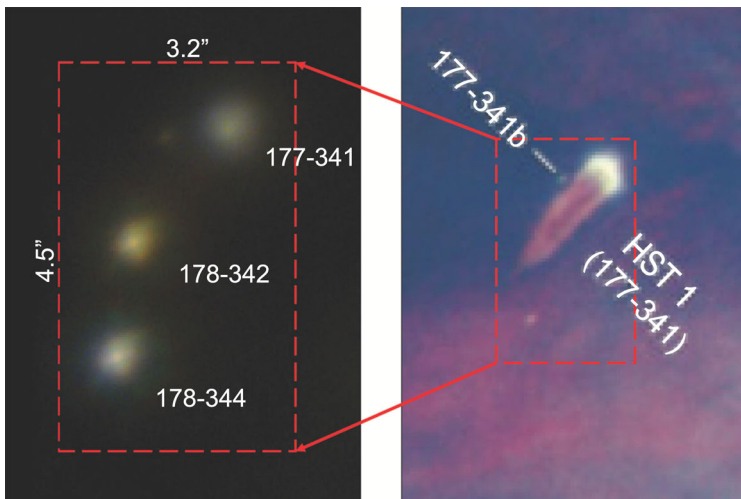

Figure 4.12: *Near-Infrared (left, KHJ ≡ RGB) image of the giant proplyd 177-341 and its neighbors in comparison to the optical HST image (right, red is [N II], green is H$_\alpha$, blue is [O I], Bally et al. 1998), north facing upwards and east to the left. The proplyd 178-342 is covered by the ionization front in the optical, but barely visible at the end of the tail.*
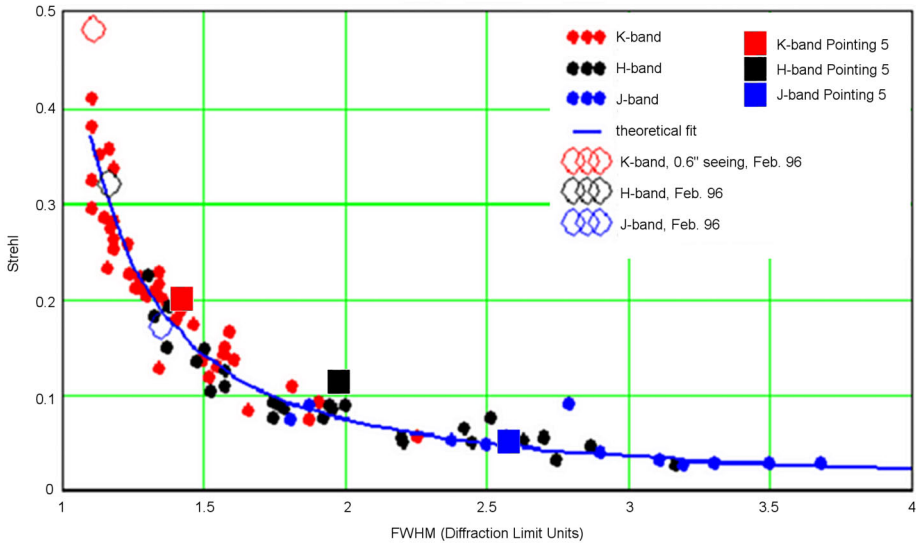
Figure 4.13: *The achieved Strehl ratio of an AO observation is a measure for the quality of the correction. Here the Strehls of the most distant FoV (pointing 5) is plotted against the FWHM of the achieved resolution in diffraction limit units. In comparison to the results from other observations a medium performance was achieved.*

its linear range. On the other hand a good SNR for the circumstellar material is achieved. The total time spent on each source was 6750 s, with several measurements per angle in different nights (375 s per source, angle, and band). θ^1 Ori C was used for wavefront sensing of the adaptive optics. The natural seeing varied from 0.5" to 1". Off-source sky for each angle and dark frames were taken, as well as frames with unpolarized reference stars. The achieved Strehl ratio in JHK was 6%, 13%, and 20% for the most distant FoV (pointing 5 with 177-341, figure 4.13). Already a Strehl value of only 0.15–0.2 allows for a spatial resolution close to the diffraction limit in deconvolved images. Higher Strehls do not add to the spatial resolution, but add to the photon concentration and SNR of the observed features.

Already the raw data (Fig. 4.6) suggests, that AO residuals are affecting the quality of the images. As discussed in chapter 1.3.3 the correction of wavefront aberrations is normally achieved by modal control, based on the Zernike modes (Eqn. 1.22). If the wavefront is obtained via a Shack-Hartmann sensor, not all modes can be corrected for with the same performance. In general the low-order modes suffer from increased phase noise (Ragazzoni & Farinato 1999). Empirically the trefoil and astigmatism modes are often dominating the AO residuals and corresponding patterns in the images may occur (Fig. 4.14). The trefoil is
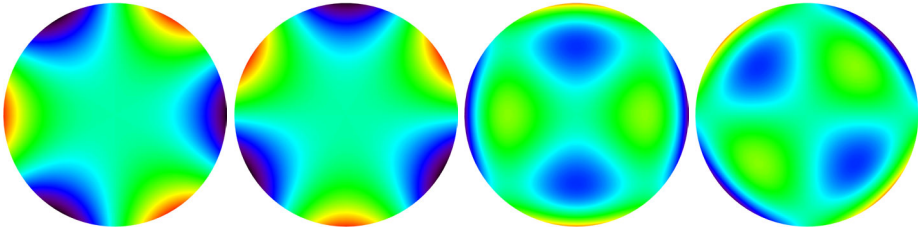
Figure 4.14: *Trefoil and astigmatism modes. These optic aberrations are problematic in AO systems. The trefoil is often over-compensated in the control-loop.*

visible in most of the polarimetric differential images (PDI) of the sample (Fig. 4.8– 4.11). An astigmatism is very similar to a PDI pattern of extended circumstellar emission (Fig. 5.11, e. g.), but a PSF residual in the case of 177-341 (Fig. 4.10 and 4.11) can be excluded by comparison with the sources in the same FoV. Although the PSF is spatially varying, the neighbors should show almost the same patterns, if dominated by PSF residuals.

Another effect of the AO correction arises, when the angular separation of the science FoV is close to the isoplanatic angle θ_0. The degradation of the PSF as a function of the field angle θ and in particular for $\theta > \theta_0$ is not completely understood. The off-axis PSF can in general be expressed as the convolution between the on-axis PSF of the guide star ($\theta = 0$) and a spatially variable kernel

$$\mathrm{PSF}(f, \theta) = \mathrm{PSF}(f, 0) \otimes K(f, \theta) \ . \tag{4.11}$$

An analytical approach for the determination of $K(f, \theta)$ can be found in Fusco et al. (2000). For an application of the theory a detailed knowledge about the turbulent layers in the atmosphere and the optical transfer function (OTF) of the telescope are necessary.

Another approach is introduced by Cresci et al. (2005) with an empirical method. Analysis of wide field AO images have shown, that the major degradation of the PSF is an increasing radial elongation towards the guide star with increasing θ. $K(f, \theta)$ can be approximated with an elliptical Gaussian with appropriate orientation. By fitting NACO data the radial and tangential kernel FWHMs (in arcsec) can be expressed as

$$\mathrm{FWHM}_r = \begin{cases} 0.107 \cdot \alpha - 0.00594 \cdot \alpha^2 & \alpha \leq 9.1 \\ 0.481 & \alpha > 9.1 \end{cases} \tag{4.12}$$

$$\mathrm{FWHM}_t = \begin{cases} 0.0871 \cdot \alpha - 0.00951 \cdot \alpha^2 & \alpha \leq 4.6 \\ 0.199 & \alpha > 4.6 \end{cases} \tag{4.13}$$
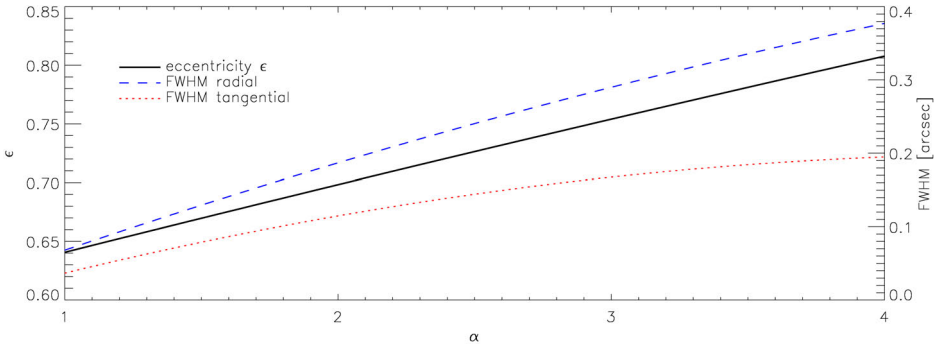
Figure 4.15: *The eccentricity of the anisoplanatic kernel as a function of field angle α, in units of isoplanatic angle. Also the FWHMs of the kernel for the radial and tangential axis are plotted.*

with $\alpha = \theta/\theta_0$. For example the kernel at an angle $\alpha = 1.5$ from the guide star would form an ellipse with eccentricity $\epsilon = 0.67$. A plot of the elongation effect is shown in figure 4.15. These effects of NACO-PSF elongation due to anisoplanatic kernels should be similar at other AO systems.

4.3.2 Data reduction

The data reduction was carried out using the DPUSER software for astronomical image analysis (T. Ott, `http://www.mpe.mpg.de/~ott/dpuser/`, see also Eckart & Duhoux 1990) and IDL routines. Due to some cooling problems of the detector some part of the data had to be sorted out by a statistical filter algorithm followed by a manual inspection. The raw images were sky-subtracted and flat field-corrected.

The non-polarized light consists mainly of the central star's light and the uncorrected AO residuals, which is the dominant noise source of ground-based AO-observations in the NIR. Polarimetric images are very sensitive to minor deviations of shift-and-add operations. Therefore this reduction step was carefully carried out and manually optimized for every single frame. A minimal number of three frames (spanning more than 90° position angle) is required to determine the linear polarization and its position angles. The redundant data set of three orthogonal polarization component pairs increases the SNR and reduces the influence of instrumental polarization. By fitting the oversampled polarization curve with a cosine function, the linear polarization angle and degree maps (Π_L) have been determined. Polarimetric differential images (PDI) can be obtained using $Q_0 = I_{0°} - I_{90°}$ (Stokes Q-parameter), $Q_{30} = I_{30°} - I_{120°}$, and $Q_{60} = I_{60°} - I_{150°}$. In the widely used notation of linear polarized light this converts to $Q = Q_0$, and

as shown in chapter 4.2.1

$$U = \frac{Q_\phi - Q \cdot \cos(2\phi)}{\sin(2\phi)} \qquad (4.14)$$

with $\phi = 30°$ or $\phi = 60°$. Π_L and θ are calculated as in equations 4.3 and 4.4. The Q- and U-parameters are used for better comparison to images obtained from Monte-Carlo simulations based on models of a YSO as discussed in chapter 5.2.

4.3.3 Photometry

As the main purpose of the Orion survey was polarimetric imaging, some trade-offs have to be dealt with in photometric measurements. The brightest sources are saturated and the detector is driven in its non-linear range. As a result PSFs of the stars are distorted. In conjunction with AO-PSF variations and temperature problems (chapter 4.3.1) the obtained photometric results are of poor quality. Hence a precise extinction correction and conversions of photometric systems was skipped. Nevertheless, in the sense of relative photometry the color-color diagram (Fig. 4.16) is suitable to classify the sources in the sample. high IR excesses and reddening relative to the other sources are observed next to 177-341 for 158-327 and 167-317. Muench et al. (2002) find high values also for 178-344 and 163-317 and, with the NTT for 158-326.

The properties of the targets are listed in table 4.4, including the IF-sizes and NIR magnitudes, J-H and H-K colors. These were photometrically calibrated with the standard star HD98161 from the 2MASS catalog. This unpolarized star was also used for polarimetric calibration.

Table 4.4: *Observed proplyds near the Trapezium stars. Only the giant proplyd 177-341 (HST 1) shows significant envelope emission in the polarimetric differential images. The table shows the distance to θ^1 Ori C, which was used as the AO guide star, and the observed JHK-magnitudes and colors (with magnitude errors ~ 0.1). The ionization front (IF) data is taken from Bally et al. (1998).*

Designation	R.A. (J2000)	DECL. (J2000)	Dist. to θ^1 Ori C	IF (opt.) Tail	Magnitude J	H	K_S	Color J-H	H-K
157-323	05 35 15.71	-05 23 22.59	11.25"	<0.7"	9.88	9.05	8.93	0.83	0.11
158-323	05 35 15.82	-05 23 22.50	9.75"	1.8–2.5"	9.73	8.83	8.53	0.91	0.3
158-326	05 35 15.83	-05 23 25.62	10.2"	0.85"	12.9	11.34	10.65	1.56	0.69
158-327	05 35 15.79	-05 23 26.61	10.53"	1.0–1.5"	11.68	10.4	9.66	1.28	0.75
163-317	05 35 16.27	-05 23 16.72	6.42"	1.6"	10.14	9.41	9.2	0.72	0.21
166-316	05 35 16.60	-05 23 16.32	7.36"	0.4"	11.4	10.47	10.2	0.93	0.27
167-317	05 35 16.73	-05 23 16.63	7.08"	0.67"×2.1"	10.37	9.41	8.94	0.96	0.47
177-341	05 35 17.67	-05 23 40.96	25.98"	0.8"×3.5"	12.44	11.83	11.53	0.61	0.3
178-342	05 35 17.76	-05 23 42.50	27.2"	. . .	12.93	11.67	11.2	1.26	0.46
178-344	05 35 17.78	-05 23 44.25	29.1"	. . .	12.083	11.28	11.1	0.8	0.17
HD98161	11 17 12.01	-38 00 51.72	. . .	. . .	6.075	6.019	5.992	0.056	0.027

4.3.4 Polarimetric Results

Some of the sources show a clearly extended structure in the NIR referring to an illuminated dust envelope. The surrounding nebula emission is not as strong and spatially varying as in the optical.

The aperture polarization of the targets is listed in table 4.5. Also the integrated polarization in two annuli are shown for comparison and classification of circumstellar material. The polarization degree values as a function of the wavelength are plotted in figure 4.17 for the aperture and the two annuli. The nebula emission in the outer annuli is polarized from 10% in K-band to 20% in J-band. This is in good agreement with a recent wide-field polarization study of the ONC in the NIR (Tamura et al. 2006). This part of circumstellar flux should be dominated by illumination of the central OB association, i.e. the polarized flux of the H II-region. The polarization in the inner annulus may be dominated by the central star and depends also on the scatting properties of the circumstellar material. The aperture polarization can be a tracer of orientations and inclinations of the disk. Although the integrated polarization degree and angle is highly affected by minor deviations in shift-and-add operations and PSF effects (see chapter 5.2) the average values give a good overview on the spectral circumstellar polarization distribution. It is evident that the slope of spectral polarization intensity is decreasing in the outer regions (Fig. 4.17).

To remove all non-polarized light from the sources orthogonal components were subtracted from each other. These images of the Stokes Q- or U-Parameters show a characteristic trefoil pattern for most of the sources (Fig. 4.8–4.11).The trefoil is a mode in the AO wavefront reconstruction that may contain residual power if the AO-loop is run under variable atmospheric conditions. However for the giant proplyd 177-341 we find significant butterfly patterns or two lobes, which is the polarization pattern expected for a circumstellar dust envelope.

The sources around 177-341 (Fig. 4.11) lie in a relatively dark region of the nebula. This is why here, we concentrate in particular on the field of the proplyds around 177-341. The NIR-image in Fig. 4.12 shows quite a different view on the proplyds morphology than the known optical images (Bally et al. 1998). First of all in the NIR-images the bright ionization front, which covers inner structures of the proplyds in the optical is not visible. This reveals for example a previously unknown source behind the tail of the proplyd 177-341 (Fig. 4.12, left). If the new source is a proplyd it would be named 178-342, following the designation system introduced by O'Dell & Wen (1994). In this scheme the catalog number refers to the position of the source. It was introduced because of the great number of findings in this region in many different surveys. The first three digits indicate the right ascension (E2000) with an precision of
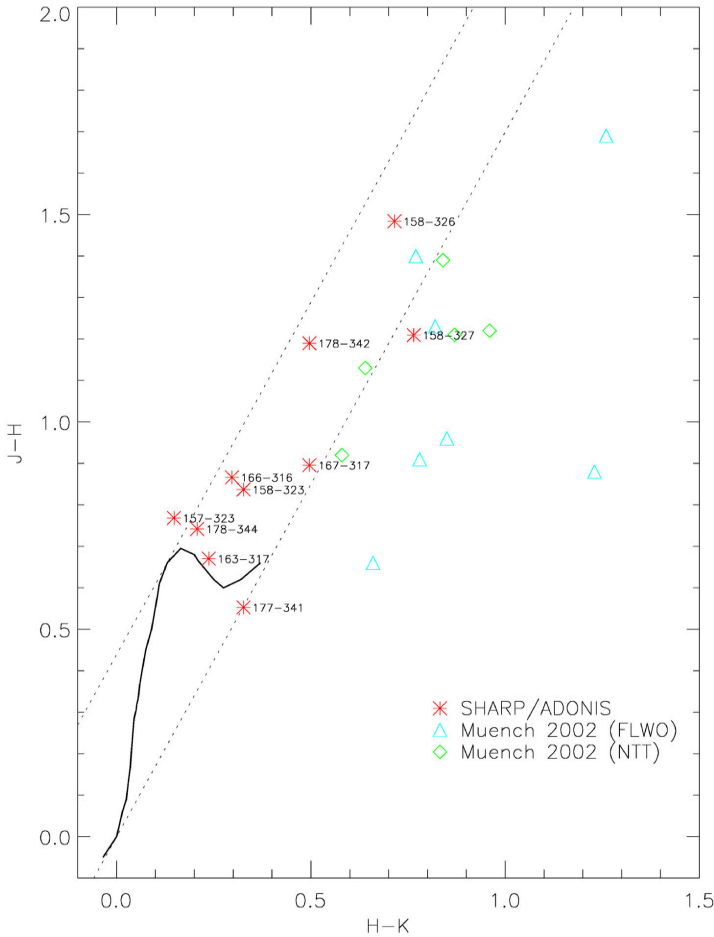
Figure 4.16: *Color-color diagram of the observed proplyds. For comparison the data of Muench et al. (2002) is plotted. Two different telescopes were used with slightly different photometric systems (FLWO and NTT). Data for intrinsic colors of the main-sequence (solid curve) taken from Bessell & Brett (1988), reddening lines are also shown (dashed lines)*

0.1^s and the second three digits to the declination with $1''$ precision. An offset of $5^h35^m00^s$ and $-5°20'00''$ respectively has to be added to these numbers to get the position on the sky.

The observed JHK-colors differ from the neighbor 177-341, 178-342 seems redder (J-H and H-K colors are listed in Tab. 4.4). This is maybe due to extinction by the overlying ionization front.

Table 4.5: *The integrated polarization of the observed proplyds and surrounding reflection nebula in an aperture of 0.1", in an annulus of 0.3"-0.5" and 0.7"-1.0" respectively. The inner region is usually dominated by alignment and subtraction residuals (Hales et al. 2006). The annulus of 0.3"-0.5" refers to the circumstellar dust, which is illuminated by the central star. The outer annulus should merely contain polarized light from the surrounding reflecting nebula where the source of illumination is unknown. At least in the case of the nebula region around 177-341 θ^1C Ori is most likely the dominant source due to the aligned vectors perpendicular to the direction of the Trapezium star (see fig. 4.18)*

Designation	Filter	Aperture 0.1 "				Annulus 0.3"-0.5"				Annulus 0.7"- 1.0"			
		Pol.[%]		Ang.[°]		Pol.[%]		Ang.[°]		Pol.[%]		Ang.[°]	
157-323	J	18.11	±0.70	35.5	±1.0	14.38	±0.25	45.5	±0.3	14.89	±0.37	38.7	±0.8
	H	4.76	±0.26	84.4	±5.0	6.41	±1.96	22.7	±0.2	11.95	±0.68	26.0	±1.0
	K_S	3.71	±1.91	62.1	±4.7	2.77	±0.64	-67.2	±29.6	11.25	±0.71	-56.7	±0.9
158-323	J	19.61	±2.09	21.0	±2.1	13.33	±1.65	44.6	±0.3	12.11	±0.77	40.3	±0.5
	H	3.58	±0.18	61.3	±2.7	5.33	±2.22	20.8	±1.8	9.30	±0.63	23.3	±0.4
	K_S	4.12	±1.22	24.4	±6.0	2.72	±0.92	-60.4	±31.4	10.31	±0.37	-51.5	±0.6
158-326	J	45.32	±4.52	35.9	±2.1	32.53	±0.71	29.9	±0.7	46.87	±1.53	29.4	±0.1
	H	9.12	±2.50	89.2	±1.6	9.26	±1.31	29.9	±0.6	20.06	±0.74	29.1	±0.1
	K_S	3.08	±1.17	-76.4	±10.5	2.61	±0.46	42.2	±7.4	4.30	±0.61	17.6	±2.0
158-327	J	19.14	±3.42	32.8	±0.4	17.27	±0.93	40.9	±1.1	18.24	±0.85	35.0	±0.2
	H	6.94	±1.69	-78.4	±3.4	7.95	±1.25	34.0	±0.8	11.69	±0.21	33.7	±0.3
	K_S	3.07	±1.84	-40.2	±16.0	3.76	±0.42	58.1	±7.4	1.93	±0.22	-88.7	±2.3
163-317	J	24.77	±2.72	34.9	±1.5	9.92	±0.44	59.5	±2.9	13.23	±1.65	71.0	±0.3
	H	2.89	±1.66	-29.5	±23.1	6.41	±1.91	68.3	±4.3	12.57	±0.87	-87.3	±0.3
	K_S	3.96	±1.61	-79.1	±5.5	5.10	±0.98	29.9	±1.0	3.12	±0.43	-24.8	±21.0
166-316	J	25.50	±1.58	44.3	±1.3	14.28	±1.95	54.8	±1.7	9.75	±1.33	77.5	±0.5
	H	3.00	±0.94	36.2	±8.2	7.46	±0.71	69.5	±2.8	5.88	±0.29	76.4	±1.1
	K_S	5.35	±2.07	-56.6	±33.3	2.22	±1.09	82.4	±9.8	4.09	±0.34	-44.2	±35.1

167-317	J	23.94	±1.38	30.8	±1.7	11.70	±1.25	38.5	±1.0	15.28	±2.48	11.9	±2.3
	H	5.86	±1.48	-10.8	±1.5	7.84	±2.30	56.8	±3.0	13.34	±6.57	21.4	±6.4
	K$_S$	1.14	±0.75	85.6	±11.5	5.09	±0.45	68.4	±2.9	8.26	±6.54	19.1	±9.6
177-341	J	5.54	±1.72	-17.0	±4.5	9.68	±1.64	-6.1	±3.8	20.38	±2.59	-3.6	±0.9
	H	1.64	±0.96	36.5	±4.1	10.27	±0.80	27.3	±1.7	19.90	±2.02	17.4	±0.5
	K$_S$	3.42	±0.20	30.3	±0.3	0.80	±1.06	-46.3	±33.0	11.14	±0.70	-58.0	±0.4
178-342	J	17.12	±3.77	50.7	±0.6	20.48	±2.03	15.4	±1.6	25.18	±2.87	7.5	±0.2
	H	6.30	±2.07	-41.3	±35.5	11.02	±3.93	16.2	±4.8	23.94	±1.99	6.4	±0.6
	K$_S$	11.11	±3.19	63.5	±4.4	0.36	±1.14	87.5	±30.6	3.14	±1.08	-48.2	±34.2
178-343	J	11.08	±0.91	59.2	±4.3	17.64	±2.59	25.8	±1.6	23.57	±1.01	15.4	±0.5
	H	11.94	±3.99	-46.3	±0.4	11.94	±3.03	23.5	±4.2	24.00	±3.99	8.3	±0.6
	K$_S$	10.14	±3.25	87.2	±0.5	2.35	±0.73	-39.6	±25.6	8.27	±1.35	-62.6	±0.6
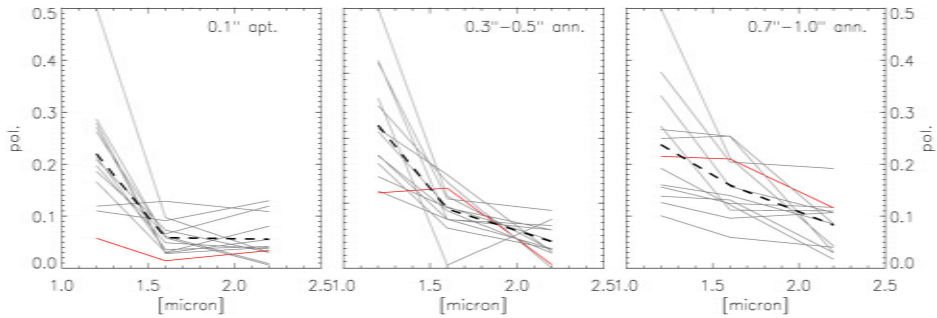
Figure 4.17: *Spectral distribution of polarization for J-, H-, and K-bands. In an aperture of 0.1"
the light of the central star the scattering by foreground material dominates. In an annulus close
to the star the polarization is higher due to the circumstellar envelope and disk. The outer annulus
is dominated by the reflection nebula and is highly polarized. The dashed line is the average
polarization spectrum, the dotted line is 177-341.*

In figure 4.18 the polarization vectors patterns of 177-341 are shown. Close
to the central source in the dust envelope a centrosymmetric pattern is visible in
relative low polarization of the order of 5-10%. The reflection nebula in the outer
regions of the proplyd shows an uniformly oriented polarization pattern with the
same direction in all bands. This is almost perpendicular to the direction of θ^1
Ori C which is most likely the source of illumination of this part of the nebula.

4.4 Polarimetric Differential Imaging

The subtraction of two orthogonal polarized images effectively improves the
contrast by removing unpolarized light, which outshines structures near bright
sources (cf. Eqns. 4.6). The method of Polarimetric Differential Imaging (PDI)
was first described by Kuhn et al. (2001), but its interpretation in the context
of young stellar source is still not well understood. The face-on disk around
HD169142 produces the peculiar pattern in PDI. Apai et al. (2004) detected
the same pattern for TW Hya and Huélamo et al. (2005) found an interesting
variation of the pattern for Elias 2-29. The famous Becklin-Neugebauer object
(BN), which was one of the first great findings in NIR imaging astrophysics,
also shows an interesting PDI (Jiang et al. 2005). On the other hand it must be
stated that the detection of a polarimetric pattern is more or less serendipitous.
Kuhn et al. (2001) had an 1:10 and Huélamo et al. (2005) a 3:11 ratio of de-
tections to non-detections. A sample of 4 promising targets of Schütz (2005)
revealed no findings and as a conclusion it was stated that PDI should not work
for sources without a prominent NIR excess. Sources with an excess should be
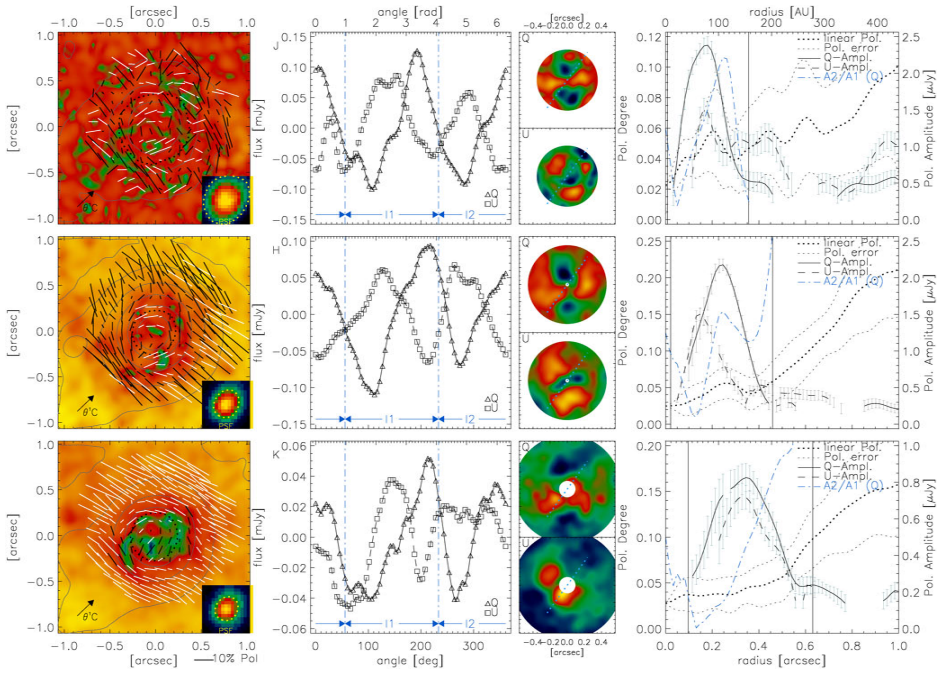
Figure 4.18: *The polarization vector maps of 177-341 show a significant pattern. Left: Polarization degree images with intensity contours (logarithmic, dotted line is 50%) in J-, H- and K-band (from top to bottom), the vector length is proportional to the degree of polarization. The reflection nebula shows an uniformly oriented polarization vectors pattern, which is almost perpendicular to the direction of $\theta^1 C$ Ori (indicated by the arrow in the lower left corner). For comparison the PSF (with dotted 50% contour line) is plotted at the same scale in the lower right corner. Right: Radial polarization profile, the linear polarization degree is increasing with the distance to the central source. The amplitude of the cosine-fit of the Q- and U-profiles (along the P.A.) over the radius is also plotted, which clearly defines the extent of the polarization pattern. The ranges are plotted with vertical lines. Middle: Stokes-Q-profile against the angle in Jansky: 5 degree bins in the Q-component against the rotation angle in the range determined with the radial plot to the right and shown in the two Stokes Q/U-doughnut-plots ($0°$-angle facing to the west, rotation counterclockwise). A slightly greater amplitude in the range of about $50°$-$230°$ (interval I1) of the Q-profile is visible in all bands. The ratio of the fitted amplitudes in I1 and I2 (A1, A2) are also plotted as a function of the radius to the right in linear range from 0 to 2.*

Table 4.6: *There are only few targets successfully detected with the PDI technique so far. References: (1) Kuhn et al. (2001), (2) Hales et al. (2006), (3) Apai et al. (2004), (4) Huélamo et al. (2007), (5) Jiang et al. (2005)*

Ref.	Telescope	Diam.	Instrument	Band(s)	Detect.
(1)	UKIRT	3.8m	IRPOL/IRCAM	H	HD169142
(2)	UKIRT	3.8m	IRPOL2/UIST	HK	HD169142, TW Hya
(3)	VLT	8.2m	NACO	K_S	TW Hya
(4)	VLT	8.2m	NACO	HK_S	Elia 2-29
(5)	Subaru	8.2m	CIAO	HK	BN
	3.6m	3.6m	SHARP/ADONIS	JHK	177-341

Table 4.7: *Parameters of the sources of known positive PDI detections (ref. Tab. 4.6). The values for age, mass and inclination θ are of great uncertainty due to modeling assumptions and lacking observations (discussions of the values can be found in the PDI-references and in Boogert et al. (2000); Bally et al. (2005); Dent et al. (2006); Setiawan et al. (2008)).*

Designation	Spectral type	J [mag]	H [mag]	K [mag]	Dist. [pc]	θ [deg]	Mass [$M_\odot$]	Age [Myr]
HD169142	B9Ve	7.31	6.91	6.41	145	0-30	2	10
TW Hya	K8Ve	8.22	7.56	7.30	54	7	0.7	9.0
Elia 2-29	K3-4	16.79	11.05	7.54	160	∼ 0	1	< 0.4
BN	B	12.5	8.8	5.0	450	85?	7-20	1
177-341	K6	12.44	11.83	11.53	450	75	1-2	

in a pre-main-sequence state for good detectability in PDI. An overview of the successful detection with PDI is given in table 4.6, while table 4.7 lists some parameters of the sources.

At this stage it not predictable wether a source, even with a confirmed circumstellar disk, is detectable in PDI. A classification of the already known PDI sources is difficult. There is a wide spectrum in mass (1-20 $M_\odot$) and ages (0.4-10 Myrs). The proto-stellar stage is not known for all sources, but should in general be a transition from Class I to Class II. Elia 2-29 is classified as an early Class I source, where TW Hya is likely a late proto-stellar system. A massive planet (∼10 Jupiter masses) named TW Hya b was recently found in the debris disk (Setiawan et al. 2008).

Circumstellar accretion disks mark optically thick regions of the reflection nebula where the polarization patterns clearly depart from centrosymmetry. The vectors in these regions show usually low amplitudes of polarization of about 10% due to multiple scattering (Bastien & Menard 1988). In the aperture of 0.35" for J-band to 0.5" for K-band the centrosymmetric pattern is visible to the left in figure 4.18. A region of shortened and aligned vectors is not clearly
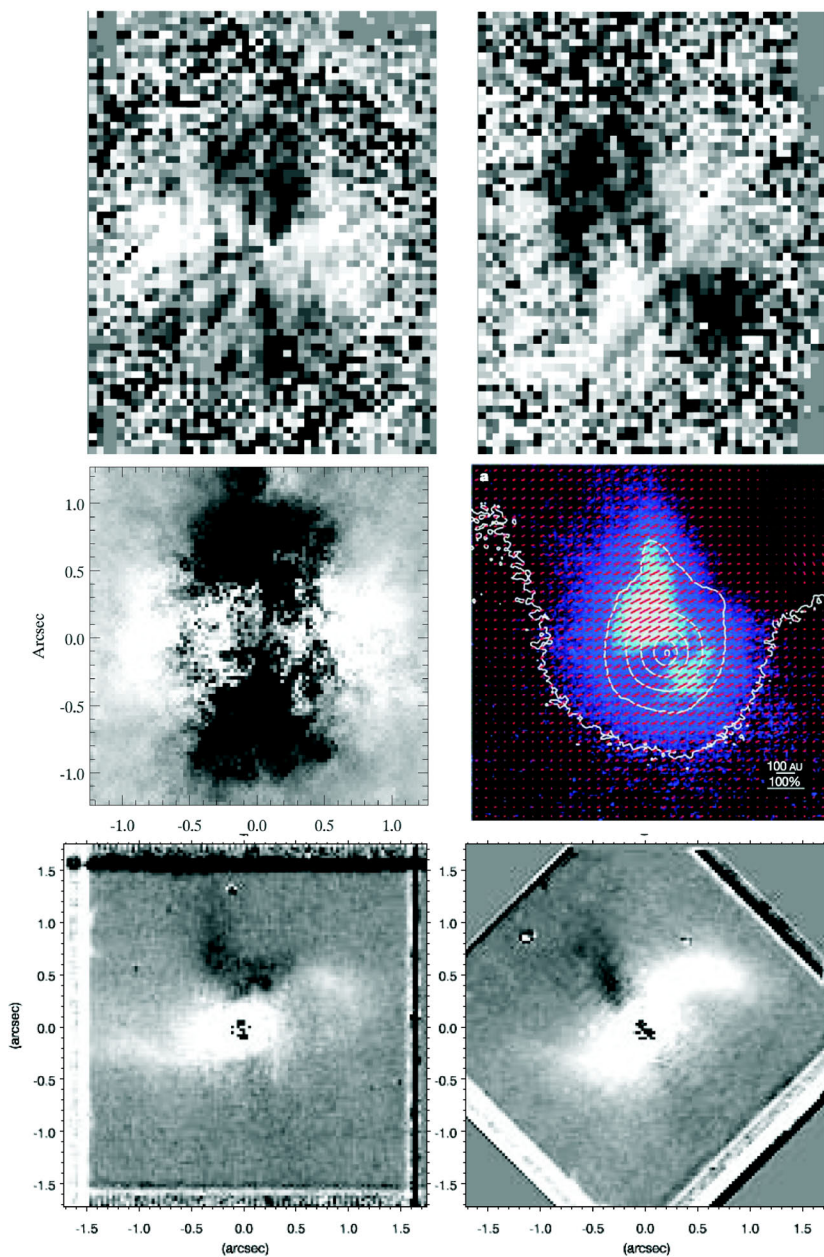
Figure 4.19: *The PDI method was successfully applied on few targets so far. Top: Stokes Q- and U-images of HD169142 with face-on disk (Kuhn et al. 2001; Hales et al. 2006), mid: Q-image of TW Hya, also with face-on disk (Apai et al. 2004) and of BN Ori (Jiang et al. 2005), bottom: Huélamo et al. (2005) found an interesting pattern in Q and U around Elias 2-29.*

resolvable in this view.

The outer regions show higher polarization and a aligned pattern from the illuminated reflection nebula from θ^1 Ori C. The extent of the polarization pattern around 177-341 is determined in the radial plots to the right of figure 4.18 as follows: The fraction of polarized light as a function of the distance from the star shows a plateau of low polarization of the circumstellar envelope and is increasing for higher radii due to the nebula polarization. For a perfect centrosymmetry the profiles along the position angle[2] of the Q- and U-images should resemble a cosine. The amplitude of the cosine fitted to the Q- and U-profiles as a function of the distance then clearly defines the extent. The maximum radius is increasing from J- to K-band and a small plateau around the maximum extent is visible in all bands.

A closer look on the spatial proportions gives the examination of the profile of the Q- and U-images by adding 5-degree-bins over the determined radial range. These Q-profiles show the characteristic cosine or W-curve for a dust envelope (Fig. 4.18, middle). In our data the profiles are not symmetric around zero as they should, this is equivalent to an offset in polarized flux and is related to effects of the PSFs. After convolving simulated polarization images with the PSF of the observations a shifting of the profiles can be seen (cf. Chapt. 5.3.2). Therefore it was tried to shift the profiles of the convolved images of the data and simulations to be symmetric around zero to achieve a result closer to the actual centrosymmetric polarization pattern (cf. Chapt. 6.2).

There is a noticeable modulation of the amplitudes of the profiles which can constrain disk parameters if we consider the optically thick accretion disks. In regions where the disk lies in front of the illuminating source the amplitude should be attenuated. To investigate and classify these effects, Monte Carlo simulations were used. In the following chapter the details of the simulation and the results are discussed, the application to 177-341 is presented in chapter 6.

---

[2]the position angle (P.A.) on the sky is counted counterclockwise from north direction

Monte Carlo radiative transfer simulations

5.1 Dust grains

The composition, physical properties and the size distribution of the interstellar dust particles have been extensively studied in the last decades. A model is needed for the interpretation and prediction of extinction and infrared emission, hence with the availability of IR observations the focus moved from stellar sources to extended objects such as reflective nebula. The modeling also could give insights in the origin and evolution of interstellar grains and help to understand circumstellar disk and planet formation.

5.1.1 Model of Mathis, Rumpl and Nordsieck (MRN)

Mathis et al. (1977) proposed a truncated power law for the size distribution between minimum grain size $a_- = 0.005\mu m$ and maximum $a_+ = 0.25\mu m$

$$n(a) \propto a^{-3.5} \ . \tag{5.1}$$

This is based on observation over the wavelength range 0.11–$1\mu m$ and fitting the extinction curve of the diffuse interstellar medium. As particle types uncoated graphite and silicates were considered. Because the distribution contains merely small particles, the observed wavelength dependence of linear polarization is not well reproduced. The wavelength of maximum polarization for stellar sources is related to the ratio of total to selective extinction $R_V = A(V)/E(B-V)$ (Serkowski et al. 1975)

$$R_V = 5.5\lambda_{\max} \tag{5.2}$$

and is located around $0.545\mu m$ for the median value $R_V = 3.1$. In the MRN model the polarization maximum is shifted to the UV-regime.
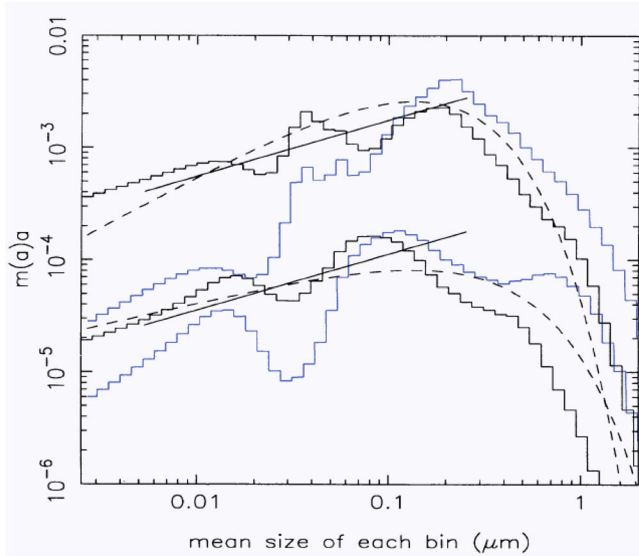
Figure 5.1: *Comparison of the dust size distribution of MRN and KMH. The solid line is the truncated power law of MRN with maximum grain sizes $a_+ = 0.25\mu m$. The upper histograms are KMH distributions for silicate and the lower for graphite (scaled down by a factor 10). Black histograms are for the diffuse cloud extinction $R_V = 3.1$, blue is for dense clouds with $R_V = 5.3$. The dashed curves are PED fits to the extinction curve for $R_V = 3.1$ (Kim et al. 1994, modified).*

5.1.2 Model of Kim, Martin and Hendry (KMH)

The basic problem of fitting a size distribution to the stellar extinction curve is the great number of unknowns and few observables. Mathis et al. (1977) handled this by assuming a smooth power law and the truncation of the grain size range. Kim et al. (1994) used the maximum entropy method (MEM) which leads to smooth solutions and also considered varying extinction curves in different regions on the sky. Local variations in the interstellar extinction curve are parameterized with the ratio of total to selective extinction $R_V \equiv A(V)/E(B-V)$. In dense molecular clouds values up to 5.1 for R_V are measured. While the standard KMH deals with the diffuse interstellar medium ($R_V = 3.1$), the alternative (here denoted as KMH_{DC}) is calculated for a dense cloud region with $R_V = 5.3$. This KMH_{DC} distribution differs from the normal as shown in Fig. 5.1. The composition of the grains is the same as in the MRN model: silicates and graphites. The MEM fitting approach results in some important differences to MRN though: in the intermediate grain size regime of 0.02–0.2μm the distribution has more structure than a simple power law. In the KMH_{DC} distribution the relative number of small particles $< 0.1\mu m$ is strongly reduced, and the amount of larger particles

shows a moderate increase.

5.1.3 Phase functions

The phase function is the dimensionless and normalized scattering function, such that the integral over 4π steradians equals 4π. The Rayleigh phase function for the scattering of unpolarized light is

$$P_R(\mu) = \frac{3}{4}\left(1 + \mu^2\right) \tag{5.3}$$

with $\mu = \cos\theta$. This describes scattering in the Rayleigh regime, meaning the regime where the size parameter

$$a = 2\pi\frac{r}{\lambda} \tag{5.4}$$

is significantly less than one. That is, if the size r of the particles is small compared to the wavelength λ. With increasing particle sizes Mie scattering becomes relevant and the phase function is commonly approximated by (Henyey & Greenstein 1941)

$$P_{HG}(\mu, g) = \frac{1 - g^2}{\left(1 + g^2 - 2g\mu\right)^{1.5}} \ , \tag{5.5}$$

where g is the asymmetry parameter, i.e. the mean cosine of the scattering angle by integration over the complete phase function

$$g =< \mu >= \frac{1}{4\pi}\int\limits_{-1}^{1}\int\limits_{0}^{2\pi} d\phi d\mu \mu P_{HG}(\mu, g) \ . \tag{5.6}$$

The greater g the stronger the forward scattering and $g \approx 0$ for $a \ll 1$. A shortcoming of this phase function is, that it converges not to the Rayleigh phase function with $< \mu > \to 0$. This was corrected by Cornette & Shanks (1992) by modifying equation 5.5 to

$$P_{CS}(\mu, g) = 1.5\frac{1 - g^2}{2 + g^2}\frac{1 + \mu^2}{\left(1 + g^2 - 2g\mu\right)^{1.5}} \ . \tag{5.7}$$

In figure 5.2 the different phase functions are compared to the computed Mie scattering for the grain population KMH. In this work both the pre-computed Mie scattering for the standard models MRN and KMH and the analytical phase
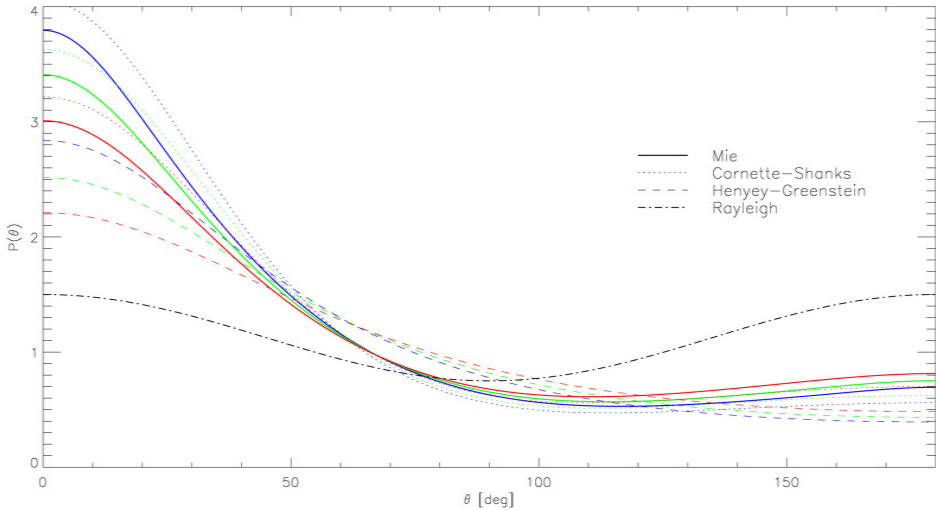
Figure 5.2: *Comparison of the phase functions with computed Mie scattering for KMH in J- (blue curve), H- (green) and K-band (red) (Whitney & Wolff 2002).*

function from Cornette & Shanks (1992) are used. In the models the latter resembles larger grains in the disk's region with appropriate parameters.

The two grain size distributions differ also in the scattering properties. The main difference from KMH to MRN is, that for grain sizes $> 0.2\mu m$ and wavelength $> 1\mu m$ the scattering is less isotropic and the albedo is markedly increased towards longer wavelength. In the wavelength range of 0.1–1.0μ the scattering parameters (g, ω) are quiet similar for both models at $R_V = 3.1$.

5.2 Collapsing envelopes

The standard models for low-mass star-formation (compare to chapter 3.1.2) include a slowly rotating, isothermal dense molecular cloud which collapses. The material with high angular momentum forms the circumstellar disk while the one with lower angular momentum falls directly into the proto-star. A common model of an infalling and rotating proto-stellar cloud is that described by Terebey et al. (1984), often referred to as TSC-model. Within the infalling region the effects of rotation dominate over magnetic effects and initial motion prior to the collapse. The initial state is an equilibrium from a slowly rotating isothermal sphere with a $\propto r^{-2}$ density profile in the inner region. Self-gravity is compensated by thermal pressure (Chandrasekhar 1939). The density profile of the collapsing envelope is then given by (not considering magnetic effects and

assuming isothermal gas over a range of density scales)

$$\rho = \frac{\dot{M}_{env}}{4\pi} \left(\frac{GM_\star}{R_c^3}\right)^{-\frac{1}{2}} \left(\frac{r}{r_c}\right)^{-\frac{3}{2}} \left(1 + \frac{\mu}{\mu_0}\right)^{-\frac{1}{2}} \left(\frac{\mu}{\mu_0} + \frac{2\mu_0^2 R_c}{r}\right)^{-1} \tag{5.8}$$

with the envelope mass infall rate $\dot{M}_{env}$, R_c the centrifugal radius, $\mu = \cos\theta$ and μ_0 the cosine angle of the streamline. The streamline is the direction, from which particles are infalling as $r \to \infty$ and is given by (Ulrich 1976)

$$\mu_0^3 + \mu_0\left(\frac{r}{R_c} - 1\right) - \mu\frac{r}{R_c} = 0 \ . \tag{5.9}$$

These describe parabolic orbits of the particles falling towards the central object. Considering the distribution of angular momentum a fraction of the mass

$$\frac{M_\star}{M(R)} \approx 1.5 \left(\frac{r_\star}{r_d}\right)^{\frac{1}{3}} \tag{5.10}$$

falls directly onto a proto-star of radius $r_\star < r_d$. The rest will accumulate in a disk. The density in the equatorial regions is enhanced over the poles due to the influence of rotation. This results in a flattened envelope and a density distribution as shown in Fig. 5.3.

   The configuration includes both a circumstellar envelope and a disk, to cover all proto-stellar classes shown in Fig. 3.1. An accretion disk density distribution is chosen according to the model of Shakura & Syunyaev (1973). Whitney et al. (2003b) implemented a disk height (h) correlation according to hydrostatic structure calculations (D'Alessio et al. 1998)

$$\rho = \rho_0 \left[1 - \sqrt{\frac{R_\star}{x}}\right]\left(\frac{R_\star}{x}\right)^\alpha \exp\left\{-\frac{1}{2}\left(\frac{z}{h(x)}\right)^2\right\} \tag{5.11}$$

$$h(x) = h_0 \left(\frac{x}{R_\star}\right)^\beta \tag{5.12}$$

with exponents $\beta = 1.25$ and $\alpha = 2.25$, and x is the radial coordinate in the disk's mid plane and z the perpendicular coordinate.

   The modeling of bipolar cavities would include an exclusion of an outflow region from the density calculation of equations 5.8 and 5.11. Instead a constant density depending on outflow velocity and mass loss is applied. The shape of the cavities varies in the literature from cylindrical to parabolic, since both features appear to be evident in observations (Reipurth et al. 2000). The opening angles are supposed to increase with evolution (Whitney et al. 2003a) and should show
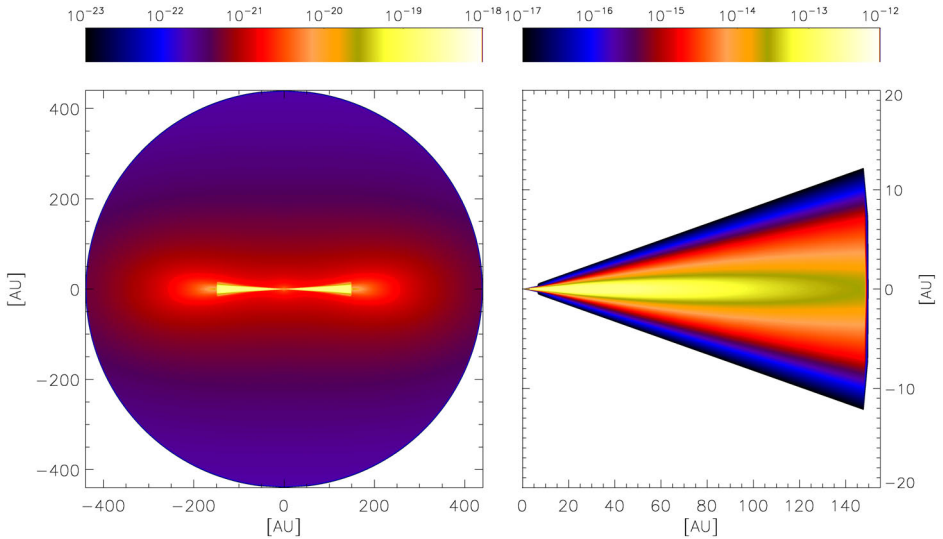
Figure 5.3: *Density distribution used in the MC-model. To the left the density of the flattened TSC-envelope (Eqn. 5.8) plus a flared disk (Eqn. 5.11). The density in g cm^{-3} is plotted logarithmic. To the right the same, but spatial scaling and density range is chosen to show the flared disk only.*

a substantial impact on the polarization images in later stages (class II–class III). In this work a detailed modeling of cavities is skipped as it is focused on early stages I–II.

As mentioned in Whitney & Hartmann (1993) an infalling envelope can easily produce the specific polarization pattern of reflection nebulae which are often interpreted as scattering from a disk. As a consequence in the case of 177-341 a highly inclined disk as suggested by the optical images (Fig. 6.6) is expected, although we see a nearly centrosymmetric pattern in the polarimetric images. The critical parameter for reproducing the pattern is the mass infall rate in the TSC-model. As the envelope size is limited to about 300AU in our images (Fig. 4.18) the centrifugal radius is determined to 150AU in the model.

5.3 3D radiation transfer code

There are two main processes for producing NIR/optical polarization as discussed in chapter 4.2.2: (i) scattering and (ii) differential absorption by non-spherical dust grains with the short axis primarily aligned along the local magnetic field, referred to as dichroic extinction (Bastien & Menard 1988). In the case of a circumstellar envelope and disk the first is the more relevant one. Al-

though magnetic fields could not be neglected in regions of star formation the interesting centrosymmetric patterns can only be produced by scattering of the light emitted by the central source. For the interpretation of the complex polarization data a 3D radiation transfer code is used, based on the Monte Carlo (MC) method (Whitney & Hartmann 1992, 1993). The code is called Ho-Chunk[1] and provides several tools for different modeling applications including star formation with proto-stellar geometries. In this work a flavour called Ho-Chunk ttsscat is used, referring to scattering and polarization in a T Tauri like configuration. The Monte Carlo type code[2] makes use of random numbers as inputs for physical processes. This is commonly used if the calculation of an exact solution is analytically impossible, e.g. in statistical processes.

The code is well-tested and many important effects are considered physically correct in the simulations:

- anisotropic scattering properties of dust

- wavelength regimes from optical to near-infrared

- polarization

- multiple scattering

- individual dust properties for different regions

These features allow to design convenient tools for the analysis and interpretation of near-infrared polarimetric images.

The dependency of polarization intensity on the wavelength refers to the effective grain size in the dust envelope which scatter and polarize the emission from the central star (Elsasser & Staude 1978). The polarization spectrum and peak polarization depend also strongly on the albedo ω, the opacity κ and the asymmetry parameter g of the grains. The latter defines the relation between forward scattering and isotropic scattering. For the grain size distribution and parameters the models from Mathis et al. (1977), hereafter MRN and Kim et al. (1994), KMH are adopted. Table 5.1 gives an overview of the differences between the two commonly used models in the NIR. In MRN grain sizes are limited to $0.25\mu m$, which is small compared to the wavelength of NIR-light, so the albedo and opacity drop for increasing wavelength. The KMH-model use

---

[1]named after a tribe of native Americans

[2]the name is a reference to a casino in Monaco and the games of pure chance. The basic concept was developed from 1945 on with the beginning of the new era of fast computers by Ulam, Fermi, von Neumann, Metropolis and others (Metropolis & Ulam 1949; Metropolis et al. 1953). It played an important role in the Manhattan Project.

Table 5.1: *Dust properties of the standard models MRN and KMH. While KMH deals with the diffuse interstellar medium (R_V = 3.1), KMH_{DC} is modeled for dense clouds with peculiar extinction R_V = 5.3 (data from Kim et al. (1994) and Whitney et al. (1997)). The scattering properties of the dust are defined by the opacity κ, the albedo ω, the asymmetry parameter g and the maximum polarization for the scattering angle of $90°$. Unit of κ is $[cm^2 g^{-1}]$.*

	MRN			KMH			KMH_{DC}		
	J	H	K	J	H	K	J	H	K
κ	65	38	20	63	38	22	48	33	22
ω	0.42	0.33	0.21	0.46	0.42	0.36	0.60	0.56	0.50
g	0.16	0.06	0.03	0.32	0.29	0.25	0.34	0.31	0.27
P_{max}	0.81	0.91	0.94	0.58	0.59	0.60	0.58	0.59	0.60

grain parameters obtained from fits to the interstellar extinction law. Mathis & Wallenhorst (1981) stated that (i) an increasing R_V implies a increasing size of particles and (ii) λ_{max}, the wavelength of maximum polarization, is larger for regions with R_V larger than the average 3.1. The peculiar extinction of θ^1 Ori C is specified with R_V = 5.5. As a result from the fit to the modified extinction curve in KMH_{DC}, the R_V = 5.3 distribution contains significantly fewer small- and intermediate-sized particles and a modest increase in larger sizes (Kim et al. 1994). This implies both a higher albedo and slightly greater g and therefore an increased forward scattering. The extinction is less at short wavelengths and flattened towards higher wavelengths. Also a modified model with different grain properties for the disks region only was tested. If grain growth in the disk is achieved, the scattering properties here should differ from the envelope. Calculations from Pendleton et al. (1990) for large grains with a ~4 times higher opacity and higher albedo are adopted, but also a wavelength dependency was implemented, so that the scattering in K-band is increased. With high opacities and hence high degree of multiple scattering, photons could be reprocessed by the disk more easily. Therefore more photons would be available in the outer regions of the envelope, so the scattering toward the observer could be enhanced.

5.3.1 Framework

The original FORTRAN code was embedded in a simulation framework based on IDL routines. With this framework a powerful tool is available to classify disk and dust signatures in the simulated images under varying parameter setups and observation conditions. It provides specifications of ranges and intervals for all parameters for a series of simulations and a quasi-parallelization of the code, as the simulation is run simultaneously for J-,H- and K-band on SMP machines. All

Table 5.2: Model variations in terms of proto-stellar classes (Whitney et al. 2003a).

Class	Envelope infall rate [$M_\odot$ yr^{-1}]	Envelope mass [$M_\odot$]	Disk mass [$M_\odot$]	Disk outer radius [AU]
0	1×10^{-4}	3.73	0.01	10
late 0	1×10^{-5}	0.37	0.01	50
I	5×10^{-6}	0.19	0.01	200
late I	1×10^{-6}	0.037	0.01	300
II	0	1×10^{-4}	0.01	300
III	0	2×10^{-5}	2×10^{-8}	300

post-processing on the images are done in IDL, so that one specific simulation run can be varied in the configuration of the applied noise level, convolution with arbitrary PSFs, rotation of the disk's P.A. with respect to the Stokes coordinate system (Eqn. 4.7). The Stokes images and the calculated Π_L and θ (Eqns. 4.3, 4.5) are stored in the astronomer's standard FITS-format with all simulation and post-processing parameters in the header.

In the simulations presented in the following the parameters for the envelope and the disk are chosen as determined from the data in the previous chapter and listed in table 5.3. This includes the envelope and disk size, where the inclination and P.A. of the disk were varied to identify corresponding signatures in the images. The mass infall rate and with it the density of the envelope was probed with a wide range of 10^{-9}–10^{-6} $M_\odot y^{-1}$ to vary the visible extent of the polarization pattern. The low value of 10^{-9} gives the best results for the average radius of 0.48". Such low infall rates would refer to a low-mass proto-star in the transition between being a late Class I (embedded in envelopes) and Class II (with T Tauri disks) object as listed in table 5.2.

5.3.2 Convolution

The optical degradation due to atmospheric seeing and telescope restrictions of a ground-based observation has a great impact on the quality of the results. Particular the linear polarization with a certain preference angle is easily affected by asymmetric distortions of the beam. Thus, the simulated images are convolved with the PSFs from observational data to be able to compare the results.

As an example, a long distance from the science target to the wavefront reference star results in elongated PSFs for the observations, if adaptive optics are used. This is discussed in detail in chapter 4.3.1. The convolution with such PSFs causes a change in the polarization properties. In the following a qualita-

Table 5.3: *Parameters used in Monte Carlo simulation. The spatial dimensions a derived from the observational data as described in chapter 4.4. This includes the proportions of the PDI-patterns for the envelope dimensions and the details of the Q-profiles for the disk parameters (Fig. 4.18).*

Parameter	Value
Number of photons	10.000.000
Stellar radius R_S	$1.5R_\odot$
Disk mass M	$0.1M_\odot$
Outer disk radius	150AU
Inner disk radius	$4R_S$
Inclination angle	$75°$
Position angle	$144°$
Scale height of disk h	$0.001R_S$
Inner envelope radius	$10R_S$
Outer envelope radius	150AU
Mass infall rate for envelope	$1 \cdot 10^{-9} M_\odot y^{-1}$

tive overview of the effects of PSF convolution on PDI is presented.

A model with a circumstellar envelope as in equation 5.8 combined with a moderate size, low-mass disk (Eqn. 5.11) shows a nearly centrosymmetric pattern in simulated, unconvolved Stokes Q and U images. At the telescope (convolved) polarization intensity images ($I_0 \cdots I_{135}$) are acquired and then PDI are generated per subtraction. In the same manner first the simulated intensity images are convolved and then the subtraction takes place. If this is accomplished with elongated PSFs, the changes in the shape of the intensity images differ in the individual angles. For clarification one could think about using Fourier transformation of the images. The convolution of the Fourier transform is achieved by multiplication, according to the convolution theorem

$$\mathcal{F}\{f(x) \otimes g(x)\} = \mathcal{F}\{f\}(v) \cdot \mathcal{F}\{g\}(v). \tag{5.13}$$

Matching frequencies of PSF and intensity image should therefore be emphasized. In other words the elliptical beam smears the polarized flux – which is ideally isotrope in an aperture – in a preferred direction. The differences in Q and U produce then the false polarization, visible mainly in the intersection of high-flux circumstellar emission and low-flux surrounding. If the aperture would be big enough, the integrated flux will be the same, as it is only shifted by the beam. But in the maps the distribution of linear polarization and the angle as determined in equations 4.3 and 4.5 vary with PSF properties. For an overview an empirical elongation law as a function of field angle α (Eqn. 4.13) was applied to
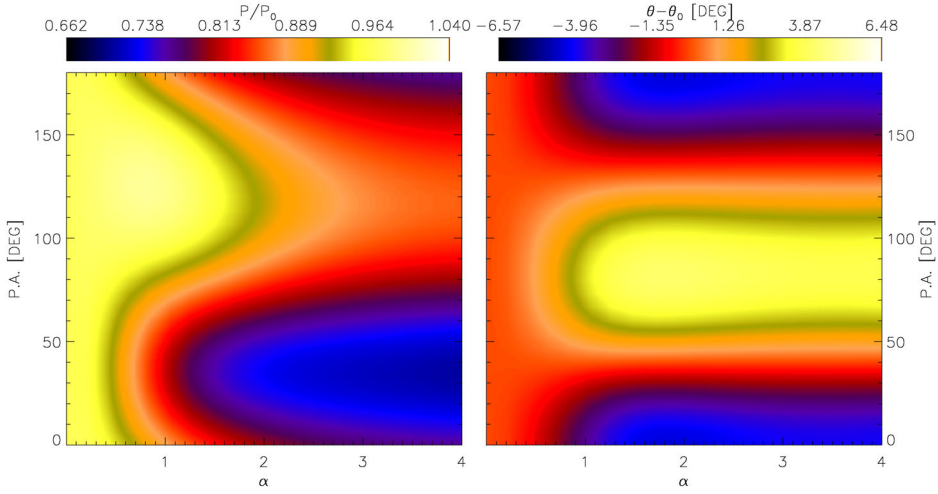
Figure 5.4: *Effects of convolution with elongated PSFs on simulated polarization images as function of field angle and position angle of PSF kernel. The basis PSF is a symmetric Gaussian with 0.35" FWHM. The kernel for elongation is determined as in equation 4.13 as a function of field angle α in units of isoplanatic angle. The resulting elongated PSF is also rotated. A simulation of a circumstellar envelope and a small, low-mass disk with a nearly centrosymmetric pattern is convolved with these PSFs and shows a modulation in aperture (1") polarization intensity (left, in units of basis PSF polarization) and angle (right).*
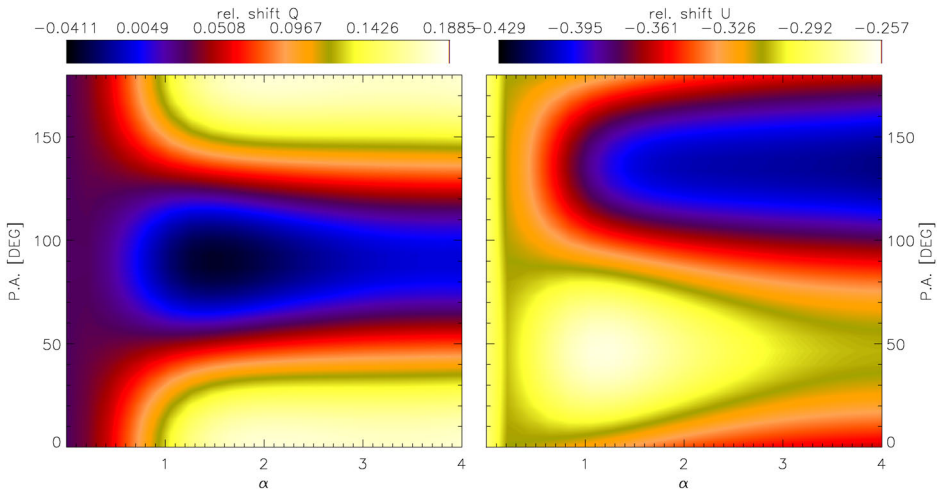
Figure 5.5: *Effects of convolution with elongated PSFs on the centrosymmetric pattern. The simulation parameters, basis PSF and elongation kernel are the same as in Fig. 5.4. The mean value of the Stokes Q and U images for a pure centrosymmetric pattern is zero. If the images are convolved with elongated PSFs, a shift of the mean value can be observed, preferably in the angles of the underlying polarization images ($Q = I_0 - I_{90}$, $U = I_{45} - I_{135}$)*

107
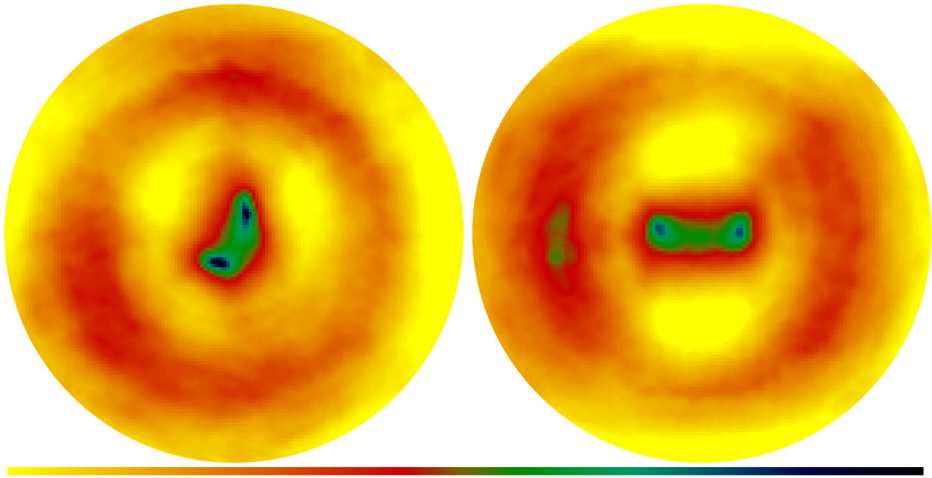
Figure 5.6: *Effects of elongated PSFs on the polarization degree images. Low polarization spots refer to multiple scattering in the disk. The P.A. of the disk should be identified by the orientation of the spots. For specific model configurations a convolution with elongated PSFs results in false spots, these are rather oriented in the direction of elongation.*

generate PSFs from rotational symmetry to strong elongation with eccentricity ~ 0.8. These were also rotated over a range of 0°–180°. The effects on polarization properties are shown in Fig. 5.4 for an example configuration. The actual quantities are dependent on the model and noise level applied to the images, as well as on the specific base PSF, which is modulated by the elongation kernel. A change in the polarization degree and angle is equivalent with an offset of the centrosymmetric butterfly pattern. In figure 5.5 the corresponding shift in the Q and U profiles along the position angle is plotted, which is strongly connected to the change in polarization properties (Fig. 5.4).

Another effect of elongated PSF convolution is shown in Fig. 5.6. As expected low polarization in the disk region is usually represented in polarization degree images with dark spots. For disks with a diameter smaller than about 150 AU the convolved polarization degree images can show a peculiar behavior: in an investigation of two models with disks at a P.A. of 90° and identical disk parameters except scale height the spots are oriented in different ways. In the case of a flat, more dense disk the spots are oriented in the right way at P.A. ~ 90°. The other disk is less dense and produces an orientation of the spots which is comparable to the direction of the PSF elongation. This effect was reproduced several times with different simulations, but no restrictions could be derived other than the small disk diameter and a moderate density. But even in these cases the effect is unpredictable, sometimes just a blurred dark spot arises.

However, it seems to be related to the ratio of the disk density to the envelope density distribution, which in turn is related to the flattening of the envelope due to rotation and mass infall rate. The effect can also be interpreted as differential changes to the Q and U images. The different amplification of angular features by the convolution results in regions along the angle of elongation where the ratio of Q to U parameters is distorted and the polarization is decreased.

5.4 PDI analysis techniques

In the following possibilities to analyse PDI observations are presented. The techniques were developed on the base of detailed examinations of simulated images. By variation of the configuration of the disk and envelope and the SNR, as well as the convolution with real observation PSFs the robustness of the analysis was tested.

5.4.1 Grain sizes

The peculiar spectral dependency of the PDI pattern of 177-341 (Fig. 4.18) could refer to grain growth in circumstellar regions. Grain growth should be most efficient in the mid plane of the disk, where the density is highest (Fig. 5.3). Larger grains should result in improved forward scattering and increased albedos at greater wavelength (chapter 5.1.2). Therefore it was tried to reproduce the spectral PDI pattern extent by testing the different grain models in the simulations and additionally model even larger grains in the disk plane. The results are shown in figures 5.7 and the spectral extent in figure 5.8. As expected is the MRN distribution with the truncated grain sizes less efficient at longer wavelength, resulting in a reversed spectral dependency. Similarly KMH is too efficient at producing polarization in J-band, because of the high amount of small grains. KMH_{DC} shows increased scattering towards longer wavelength and an increased optical depth. The combination with large grains in the disk results in a moderate additional increase in K-band, but the spectral extent is far from reproducing the observed strong increase from J- to K-band (Fig.5.8).
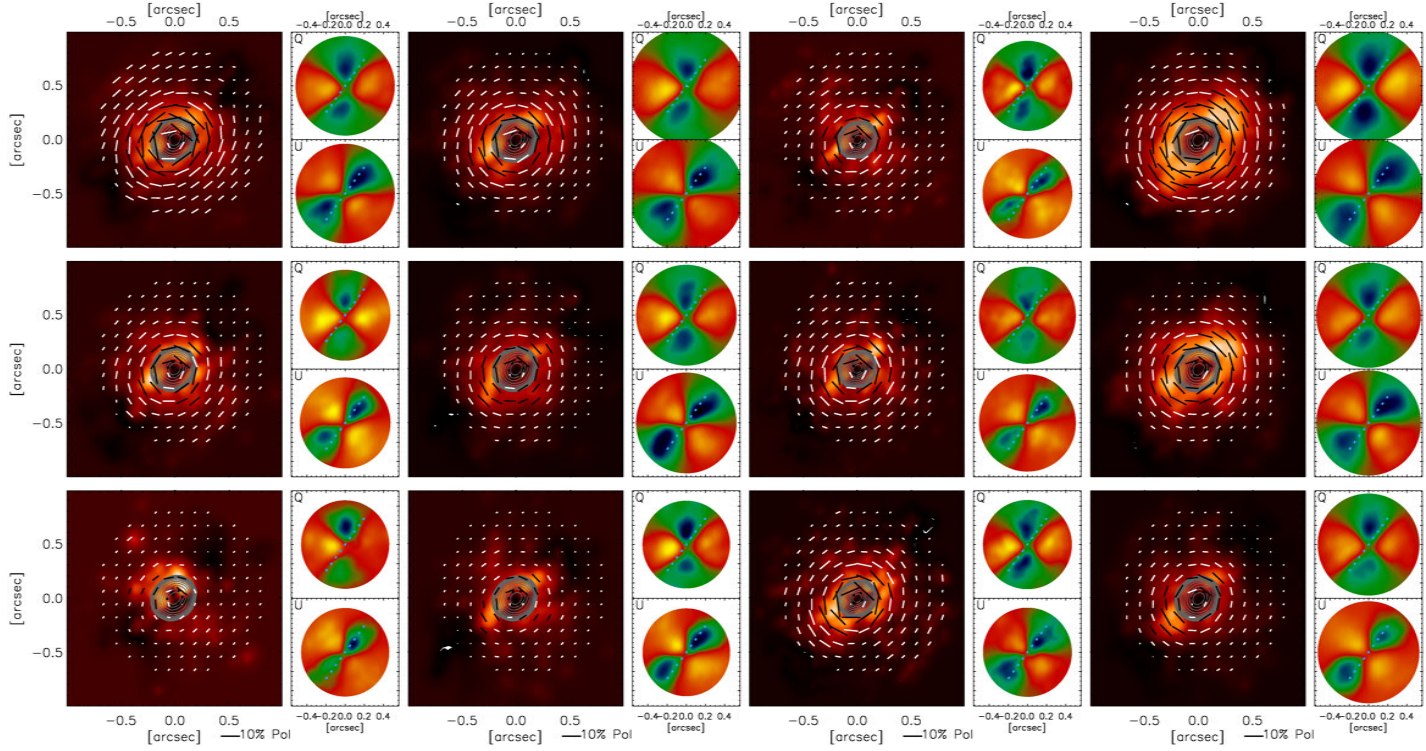
Figure 5.7: *Comparison of the different grain models used in the simulations. From left to right: MRN, KMH, KMH$_{DC}$ and KMH$_{DC}$+ large grains in the disk region (each in J-, H- and K-band form top to bottom). The polarization vectors and the extent of the Q- and U-patterns are shown, determined as described in Fig. 4.18. The images have been convolved with the PSF of the observations. The aligned vectors in the outer regions are an effect of the elongated PSF.*
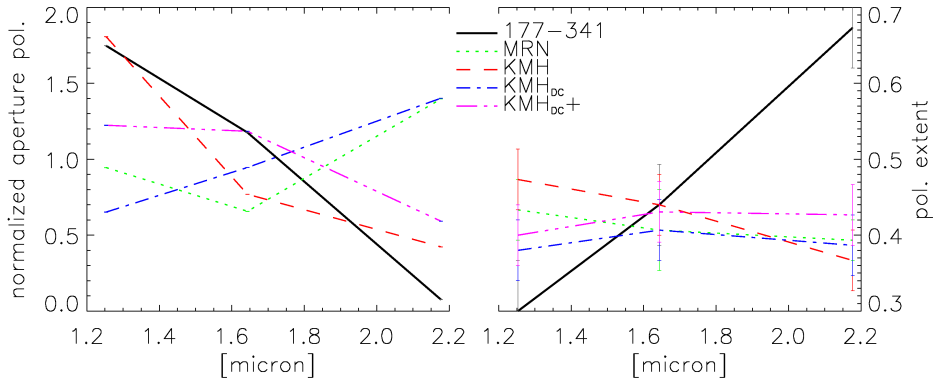
Figure 5.8: *Results from Simulations with different grain models in comparison to the observational data. The polarization extent in arcsec as a function of wavelength is shown (determined as in Fig. 4.18). The standard models MRN and KMH show a reversed spectral dependency. KMH_{DC} for a dense cloud is flattened, but shows no increasing extent with wavelength. If large grains are put into the disks region of the model a moderate increasing extent can be reproduced ($KMH_{DC}+$).*

5.4.2 Diameter

The envelope size is determined from radial amplitude fits of the centrosymmetric polarization pattern as described in chapter 4.3.4 and in Fig. 4.18. The size of the disk, which can be difficult to see in convolved images, can be derived from the polarization degree images. The polarization is low due to multiple scattering in the optical thick disk, resulting in regions of shortened polarization vectors. In figure 5.9 the polarization degree image is shown, which corresponds to the length of the vectors in a vectors map. The disk is easily seen against the high polarization of the envelope. The principle is comparable to the silhouette disks detected by HST in the bright H II-region (cf. Fig. 3.3). The contrast and with it the detectability depends on the amount of envelope polarization, which is related to the density distribution, the TSC infall rate and the opacities. On the other hand lower polarization in the disk is connected with a high density and mass of the disk.

As shown in section 5.3.2, the PSF can produce false dark regions in the images. To obtain reliable signatures of the disk it is probably advisable to deconvolve the observation images beforehand.

5.4.3 Position angle and inclination

There is a noticeable modulation of the amplitudes of the profiles which can constrain disk parameters. In regions where the disk lies in front of the illuminating
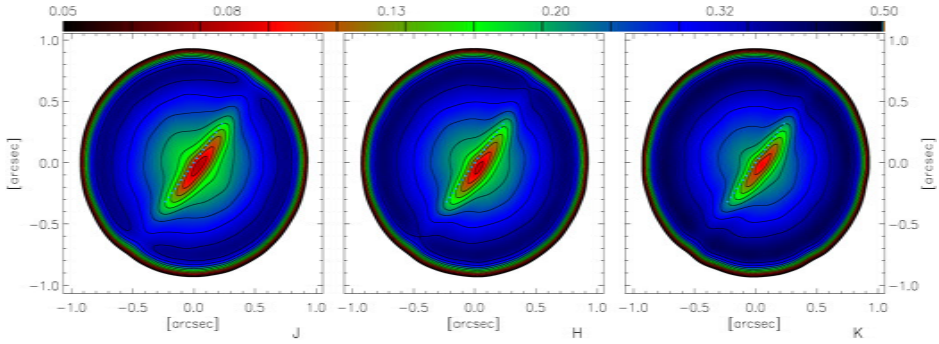
Figure 5.9: *Polarization degree images for a MC simulation with a disk inclination of 75° and diameter of 100 AU. The region of the disk shows low polarization and is easily seen against the high polarization of the envelope.*

source from the observers point of view the amplitude should be attenuated. The same applies, where the disk blocks the propagation of the central light to outer regions of the envelope. This can be associated with the amplitude modulation (AM) technique used for communication and signal transmission (Fig. 5.10). The envelope scattering is the carrier signal, i.e. a cosine with fixed phase in the Q- and U-profiles. Since there is no reference amplitude and there are only two cycle periods (see Fig. 4.18), only the ratio between the two can be determined as the modulation signal. For an investigation of these effects amplitudes ratio maps were generated, which are defined in polar coordinates as follows: For every position angle and radius (r_0, ϕ_0) the Q-profile over a range from (r ,$\phi_0 - 90°$) to (r, $\phi_0 + 90°$) is fitted with a function $f(\phi) = A_0 + A\cos(2\phi - \phi_Q)$ with free amplitude A and amplitude offset A_0, but fixed phase offset $\phi_Q = 0°$ and $\phi_U = 45°$ respectively. The best-fitting amplitude is divided by the one of the remaining 180° (for clarification see Fig. 4.18, middle: dash-dotted lines). The cosine-fitting incorporates the model of the fixed carrier signal amplitude. The individual fitting over the radius r allows arbitrary radial density and polarization profiles for the envelope, but rotational asymmetries like flattened envelopes are not considered. The result has an advantage over the pure Q-/U-profiles, since the attenuation of the signal is determined over the whole position angle and the SNR is increased under the assumption of centrosymmetric envelope profiles. In principle also the achievable spatial resolution is enhanced by the high sensitivity of the signal to modulations. The results are shown in figures 5.11–5.13 for models with a flat and a flared disk, respectively. The behavior of the maps for the unconvolved images is as expected and can separate the disk signal from the envelope signal to some extent. However, if the images are convolved with
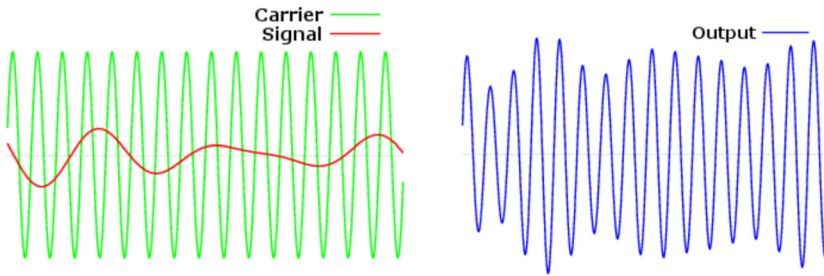
Figure 5.10: *The working principle of amplitude modulation: a carrier signal with fixed frequency and amplitude is modulated by the wanted signal. At the receiver the signals can be split again with the knowledge of the carriers characterizations.*

elongated PSFs the Q- and U-maps perform differently, depending on the P.A. of the disk. For a P.A. of 90° (a horizontal line indicates the disk plane) the Q-map is distorted, because of the low amplitude of the carrier in the region of the modulation by the disk (Fig. 5.13, left panel, e. g.). The same applies for a P.A. of ~ 135° and the U-map. With low amplitude signal PSF elongation effects become dominant.

A ratio map of a flat disk gives also an indicator for the inclination angle. In this case the disk silhouette forms an ellipse with semi-major axis a (the disk radius) and semi-minor axis b, so the inclination is given by $\xi = \arccos(b/a)$. As the radial extent of the modulation in the amplitudes ratio map refers to b, the inclination can be evaluated. If the radius a can be determined and a flat disk is assumed, the shape of the ellipse is set and the minimum inclination angle is given by $\xi = \arccos(b/a)$. Considering the height of the (flared) disk, this value is increased. This can be seen in figure 5.13, where the flared disk produces a greater radial extent of the modulation as the flat disk for the same inclination. As a result a possible inclination range can be derived, which depends on the height of the disk. This is discussed in chapter 6.4 for the observations.

5.4.4 Discussion

As shown in figure 4.18 an increasing pattern size is observed from J- to K-band. To exclude angular resolution effects the PSFs from calibration stars, extracted PSFs from the FoV (Chapt. 6.3) and the diffraction limit of the telescope are compared in Fig. 5.14. Also the achieved Strehl ratio is considered. A higher Stehl ratio means a better PSF and, therefore, being closer to the optimum in angular resolution for the convolved images (cf. Chapt. 1.3.2).

Considering grain sizes alone in the simple modeling can not explain the pe-
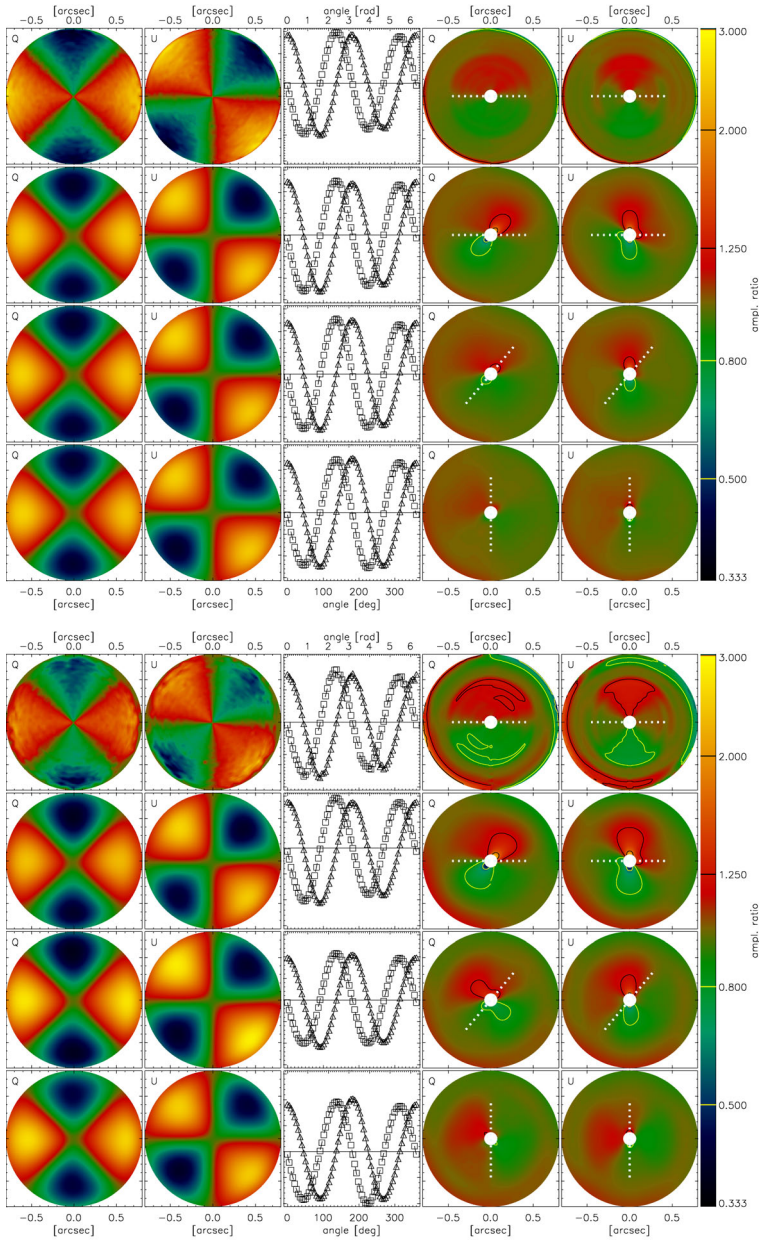
Figure 5.11: *Monte Carlo simulations of circumstellar envelope and disk. Top panel from left to right: Q-image, U-image, Q- and U- profile, Q-amplitudes ratio map and U-amplitudes ratio map in H-band.The disk is dense and flat ($M = 0.1 M_\odot$, $h = 0.001 R_S$). The inclination is $\xi = 10°$. From top to bottom: unconvolved images with P.A.= 0° for the disk, images convolved with elongated PSF, P.A.= 0° and convolved images with P.A.= 50°. Bottom panel: the same for a dense and flared disk ($M = 0.1 M_\odot$, $h = 0.01 R_S$). The profiles and maps show no significant modulation in the nearly edge-on configuration.*
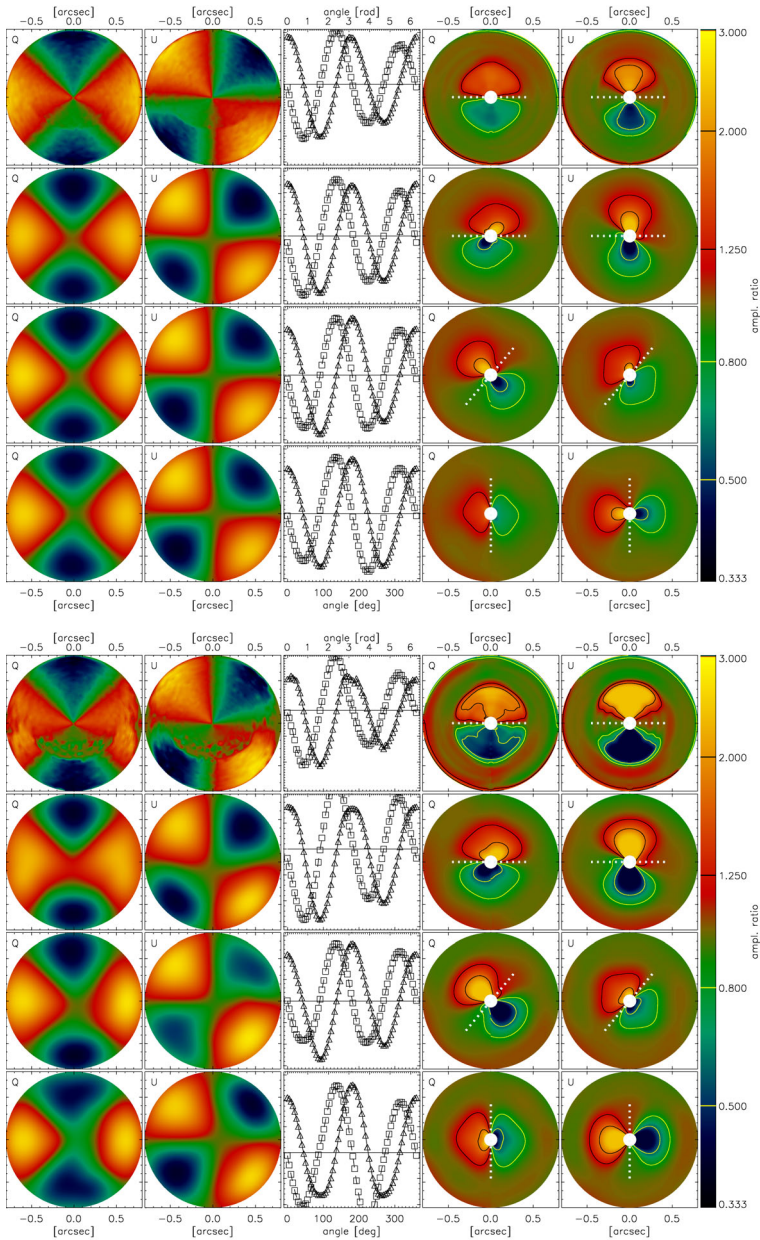
Figure 5.12: *Same as figure 5.11, but for $\xi = 45°$. The effects of the disk on the envelope signal is strong as the amplitude of the profile is attenuated where the disk lies in front. In the maps the P.A. is clearly seen and the radial extent of the modulation refers to the inclination angle.*
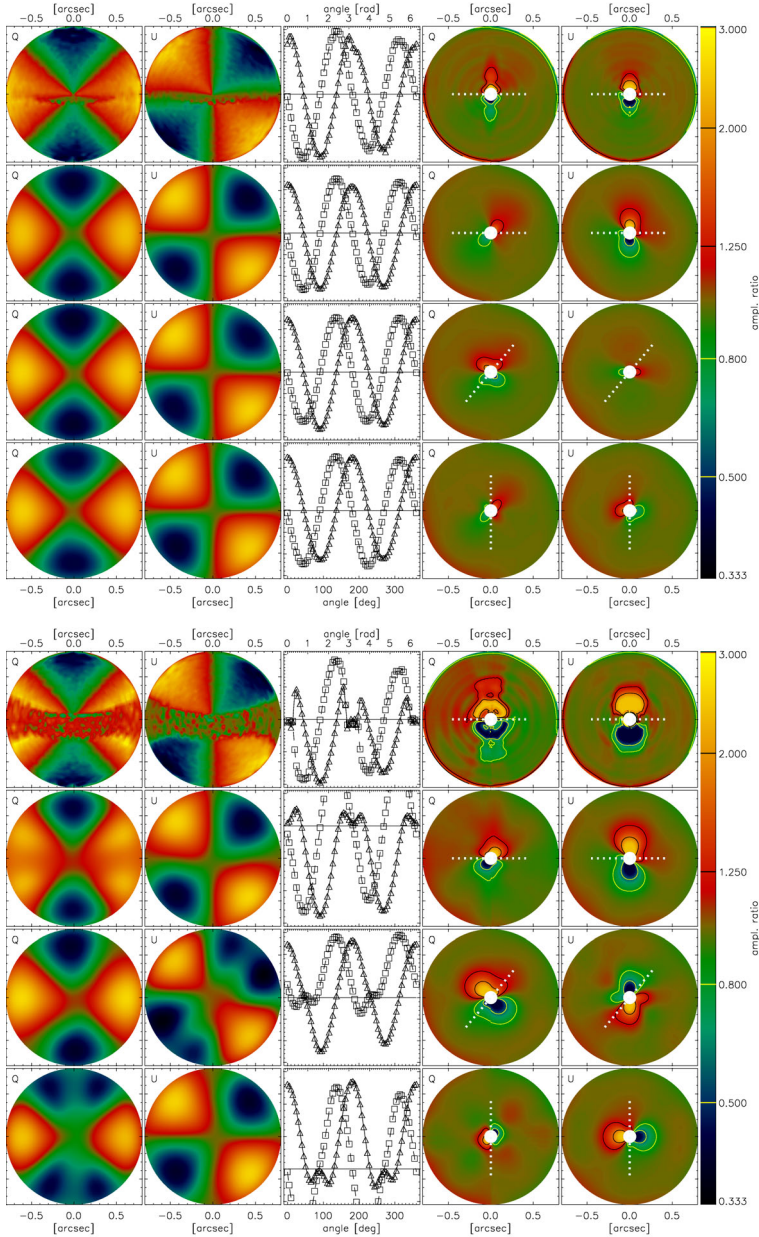
Figure 5.13: *Same as figure 5.11, but for $\xi = 80°$. Nearly seen edge-on, the disk modulation is still seen in the envelope signal. For the flat disk (top panel) the extent of the modulation refers to the inclination, as the height of the disk is negligible against the minor axis of the ellipse in projection. The extent of the highly flared disk (bottom panel) is dominated by the disk height.*
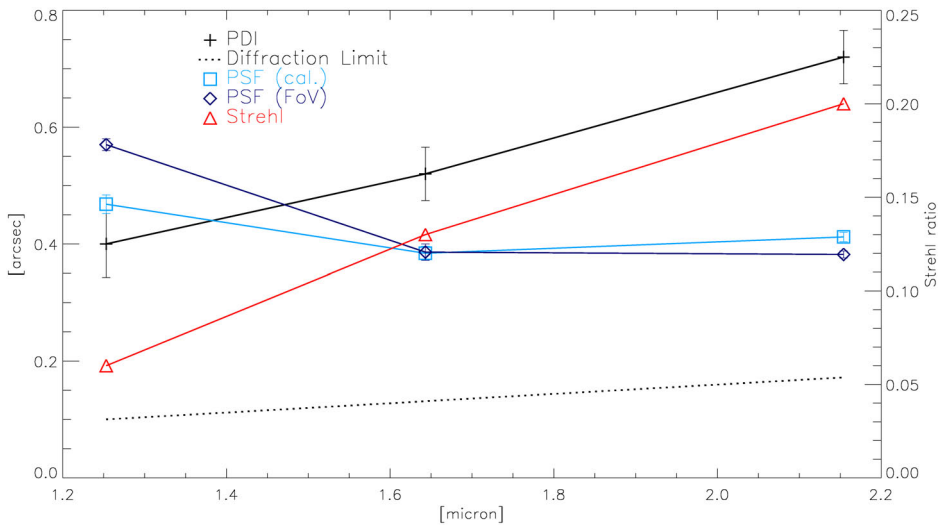
Figure 5.14: *The angular size of the PDI pattern as a function of wavelength in comparison to the diffraction limit of the telescope (dotted line). Also the FWHM of the PSFs are shown, both the PSFs of the calibration stars and the PSFs which have been extracted from the FoV (see chapter 6.3). This shows that the extent of the pattern is not resolution limited and no PSF effect.*

culiar spectral polarization behavior observed. Tests with freely modified scattering parameters (Tab. 5.1) suggest, that an reversed spectral opacity, meaning a lower opacity in J compared to K, can produce the observed spectral patterns. To justify this and to find a physical legitimation to this, advanced modeling is needed, including probably a different grain size distribution as an alternative to MRN and KMH. Also it could be worth to include the surrounding of the proto-star in the modeling, especially the opacity behavior in the intersection of the outer envelope and the nebula material. Finally the disk model could be improved, as the outer edge is artificially truncated (cf. Fig. 5.3) and this might affect the scattering in this region. Hughes et al. (2008) recently showed discrepancies between the extent of dust continuum emission and molecular gas emission, suggesting a different shape for the edge of the disk. An alternative disk model with a tapered edge agrees better with observations than the commonly used truncated power-law model.

Another problem of the comparison to simulation images is due to the Monte Carlo nature of the code. The extent of the circumstellar pattern is dependent on the number of photons used. When the number of photons is too high, even outer regions of the envelope will scatter significant amounts of light, although the probability is low. The detection of such light on the real detector is in turn related to the DIT. The boundary is also determined by the noise level or the

luminosity of the surrounding nebula - which is even varying both spatially and spectrally. A good agreement in the model with 10^7 photons is found, which means, that a simulation run in J-, H- and K-band will take about 50–60 minutes on a four CPU Xeon 3.06 GHz machine with quasi-parallelization. With a high number of parameters with wide possible ranges it was not possible to do a systematic fitting over all parameters e.g. with a χ^2 test. Particularly the varying surrounding nebula and features in the observations, which could be interpreted as multiple outflows are difficult to model. If the basic model is not well chosen, a systematic fitting might succeed due to the high number of free simulation parameters, but the physical insights may be doubtful. Therefore here I concentrated on properties, that can be extracted from simulated images of general models reliably and lead to geometrical parameters of the disk-envelope configuration.

The polarization degree maps and the introduced amplitude ratio maps are considered as tools to highly increase the detectability of disk signatures. Where optical imaging fails due to the bright IF and disks might not be seen clearly in pure IR imaging due to SNR and spatial resolution, polarimetric differential imaging in conjunction with the analyse tools seems advantageous. But these techniques work only, if

- the target is a proto-star in the transition between Class I and II. That is, if the envelope is clearly seen in the PDI and the mass infall rate for the TSC-model is still high enough.

- the disk is yet dense enough for a reasonable high fraction of multiple scattering and therefore low polarization

- the disk is inclined in a range of about 10°–80°. In the extremal cases edge-on and face-on there is no asymmetric damping of polarization amplitudes.

Most circumstellar disks that are resolved in the NIR are seen edge-on or face-on, as this configurations are easily seen in pure imaging observations or coronagraphy (McCabe & Stapelfeldt 2007). In this sense the proposed technique is a good supplement to the common observation techniques of IR astronomers.

Probing the giant proplyd 177-341

6.1 Overview

The proplyd 177-341 is sometimes also referred to as HST1 and is located about 25" south-east from the ionizing star θ^1 C. It lies in a relative dark region of the nebula and has a peculiar shaped IF. Because of its brightness, size and symmetric shape it is one of the best studied sources in Orion. In the following some important results are summarized.

Henney & O'Dell (1999) fitted emission line profiles obtained by high-resolution spectroscopy to photo-evaporating flow models (cf. Fig. 3.4) and find e.g. for the inclination angle of the disk a range of 75°-85°[1]. The mass loss rate is determined to $9.4 \times 10^{-7} M_\odot yr^{-1}$.

Robberto et al. (2002) modeled the SED for a photo-ionized proplyd and found that the disk emission is bright in the mid-infrared and comparable to the central star. They propose a highly inclined disk configuration for 177-341. The proplyd was imaged at 10.1μm with the MAX instrument on the 3.8m UKIRT telescope (Fig. 6.1). The diffraction limit of 0.7" was obtained in these observations.

Bally et al. (2000) interpreted HST [O III]-images of 177-341 as a disk seen in silhouette against the bright IF. They propose a P.A. of 105° although the silhouette suggests a P.A. of about 135° to 145° because of the compact source about 0.5" east of this proplyd which is likely to be an ultra compact Herbig-Haro object (177-341b in Fig. 4.12). The HST data of Bally et al. (2000) is shown in figure 6.2. Additionally, it was tried to emphasize the silhouette of the disk with a special filtering technique. The images were subtracted by a Gaussian-smoothed version of itself to attenuate extended emission. As a result, edges are better seen. In this view the disk is more evident in all filters and the P.A. range of 135° to 145° is confirmed, although an estimation is difficult with the limited resolution and varying IF.

---

[1]the inclination in the context of cricumstellar disks is defined as the angle between the disk's plane and the observer's image plane, which means that a face-on seen disk has an inclination angle of 0° and an edge-on disk 90°
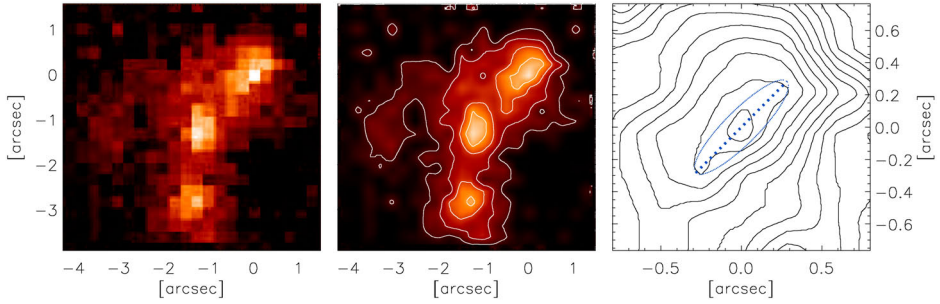
Figure 6.1: *Mid-IR (10μm) image of 177-341 and its neighbors. From left to right: raw image (Henney & O'Dell 1999), smoothed image (0.3"-Gaussian) with linear contours and zoomed contours only with the proposed disk configuration. The elongation of the contours suggest a P.A. of the disk of ≈ 138°, considering the emission of the disk at 10.1μm. However, it is not clear which part of the emission is from the disk and which is from scattering of the envelope dust. It seems that there is more emission in the north-east, which could be an evidence of inclination.*
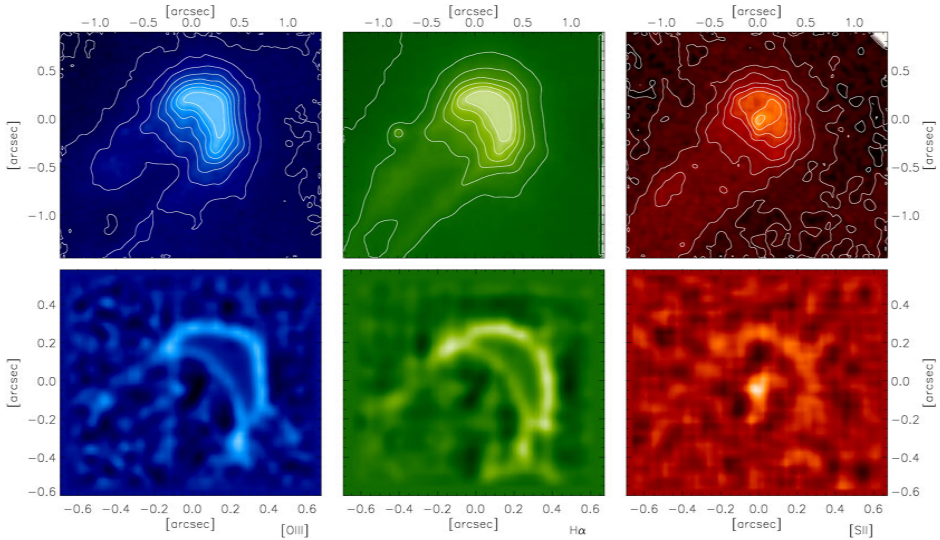
Figure 6.2: *HST optical images (Bally et al. 1998, 2000) of 177-341 through the filters f502N ([O III], blue), f656N (H α, green) and f673N ([S II], red). The images to the bottom have been subtracted by a Gaussian-smoothed version of itself, which enhances the local contrast and attenuates extended emission. A possible disk orientation can be identified. There is also some indication of an outflow, which Bally et al. (2000) claimed to end in the compact (HH-)object 177-341b 0.8" east of the center (best seen in the H α-image). However, the silhouette disk and the outflow seen in the optical images suggest a P.A. of 130°–150°.*
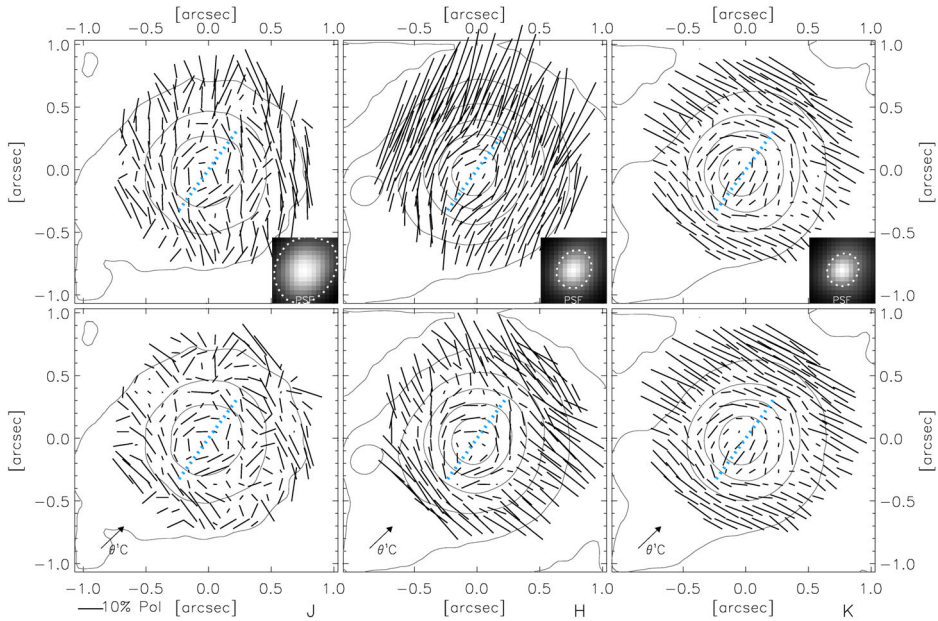
Figure 6.3: *In the top panels (JHK from left to right) the polarization vectors pattern is shown, after polarimetric calibration of the data. Because the PSF-elongation was shown to affect the alignment of vector by inducing an effective polarization offset as discussed in chapter 5.3.2, the Q- and U-images were shifted to be symmetric around zero in the centrosymmetric part of the pattern. The result to the bottom shows the expected vector behavior of the centrosymmetric part of the star/envelope and the aligned vectors in region illuminated by θ^1 C Ori.*

Vicente & Alves (2005) performed a deep analysis on the HST data and determined the disks size from the IF diameter. Models of the photo-evaporation process predict a dependency of the diameter on the disk size. The extent of the IF is also determined of the spectral power of the UV radiation. For a distance of 0.01-0.3 pc to θ^1 Ori C the FUV (far-ultraviolet) photons dominate the dissociation process and the disk radius is typically $r_d \gtrsim r_{IF}$ (Johnstone et al. 1998; Störzer & Hollenbach 1999). In the case of 177-341 the diameter of the IF is ~0.8" or 350 AU.

6.2 PSF effects

The polarization vector patterns of 177-341 shown in figure 4.18 were not only polarimetrically calibrated with an unpolarized standard star. An additional calibration based on the centrosymmetry of the pattern around the central star was applied.

As shown in chapter 5.3.2 asymmetric PSFs can induce offsets in polarization angle and degree by effectively shifting polarized flux from the central part – where the flux is high – to the outer part with a preference forced by the shape of the PSF. To minimize these effects it was tried to shift back the Q- and U-profiles to be symmetric around zero. The range for the determination of the offset is chosen as shown in the right panels of figure 4.18. Only the centrosymmetric part is considered, in which a significant amplitude in the profiles is visible. The average offset is then subtracted from the Q- and U-images, which affects the calculation of Π_L and θ, but not the PDI-images. The resulting vector maps are shown in figure 6.3. For J- and K-band the changes are not strong. Note that this calibration does not correct for the integrated polarized flux, which is decreased by the PSF smoothing. A slight correction of vector alignment is seen away from the preferred direction of the PSF to θ^1 C Ori. In the case of the H-band a big change is seen, though. The alignment of the outer vectors is changed by more than $90°$. The flux in the outer region with no centrosymmetric part seems to suffer from a significant offset in polarization. It must be stated, that the total flux here is very low, so that minor offsets or calibration errors have a great impact in these region. The back-shifting based on the centrosymmetric part removes this offset. Due to the low and varying flux in the nebula the calibration from unpolarized stars is difficult and minor residual offsets can be left in the data in addition to the mentioned PSF effects. It seems that a constant offset over the FoV is effectively compensated, when the centrosymmetry in the high-flux part is considered. This technique can therefore be seen as a bootstrap calibration for removing PSF- and constant calibration residuals. This has an impact on the pattern of the surrounding reflection nebula, which is highly polarized, but the total flux is low. The relative changes in the region of centrosymmetry are irrelevant due to the higher flux, the analysis of the individual Q- and U-images in this study is not affected.

6.3 Deconvolution

The polarization maps and in particular the polarization degree maps are very sensitive to disturbances like residual speckles. The maps shown in figure 4.18 to the left are therefore very noisy and show artefacts of the uncorrected PDI images. Deconvolution of the individual polarization intensity images $I_0 \cdots I_{150}$ seems necessary to produce reliable maps.

PSFs of the observation are obtained from calibration stars before and after the polarization frames. But these stars differ in magnitude from the real target and the seeing changes continuously so the PSFs will be different. Also, the
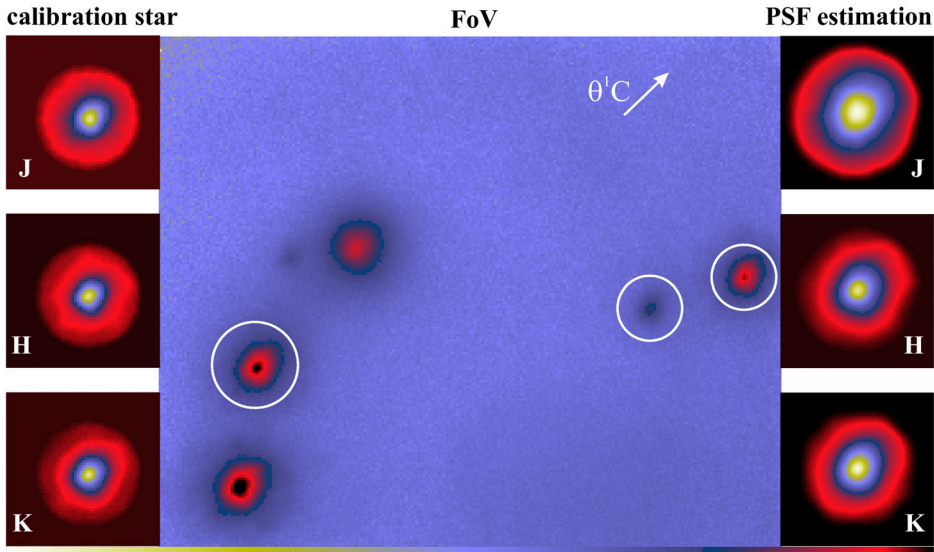
Figure 6.4: *PSF estimation from the FoV of pointing 5. To the left the PSF from the calibration star is shown. These refer to the purely atmospheric PSFs, as the frames are taken immediately before and after the science frames (middle). With StarFinder it was tried to estimate the real PSFs from the field. The chosen point sources are encircled in the FoV and the resulting estimates are shown to the right. The elongation towards θ^1 C is clearly seen and the PSFs are slightly broader in comparison to the calibration star due to the great field angle.*

position of the calibration star relative to the target leads to a different elongation angle of the PSF, since this angle points always towards the guide star θ^1 Ori C. In the case of pointing 5 containing 177-341 this effect should be significant due to the relatively high angular distance. Since there are some sources in the observed field that are nearly point-sources, it was tried to estimate PSFs with the StarFinder program (Diolaiti et al. 2000). This software package written in IDL is specifically designed for the analysis of AO images and the extraction of the PSF directly from the frame and can be found at `http://www.bo.astro.it/~giangi/StarFinder/`.

The stars chosen for PSF extraction and the resulting PSFs in comparison to the calibration PSF are shown in figure 6.4. The proplyd 178-343 is slightly saturated and was not considered. The extracted PSFs are significantly broader in J band and slightly broader in H and K. This is in agreement with the Strehl ratio measurements for this FoV (Fig. 4.13). The direction of elongation is different, as the calibration star is located with an offset of a few arcsec to the east of the FoV with the science target. Taking into account the real elongation is of great importance for the polarimetric results, as discussed for simulations in

chapter 5.3.2. The variation in broadness of the PSFs is considered to be not as important for the results. With ADONIS the diffraction limit spatial resolution is already achieved at Strehls $\gtrsim 0.15$.

For the deconvolution estimation the Lucy-Richardson algorithm (Lucy 1974) with several thousand iterations[2] as provided by DPUSER was used. For the differential images two approaches were tested. It was tried to deconvolve the individual $I_0^{\mathrm{obs}} \cdots I_{150}^{\mathrm{obs}}$ as well as the observed differential images Q^{obs} and U^{obs}. This should be equivalent, as the convolution operator is distributive

$$\mathrm{PSF} \otimes I_0 - \mathrm{PSF} \otimes I_{90} \quad = \quad \mathrm{PSF} \otimes (I_0 - I_{90}) = \mathrm{PSF} \otimes Q \qquad (6.1)$$

$$= \quad Q^{\mathrm{obs}} = I_0^{\mathrm{obs}} - I_{90}^{\mathrm{obs}} \qquad (6.2)$$

The convolution of the Q images yield results of much worse quality though, as no features are visible in the different bands. This is interpreted as the effect of measurement and alignment noise. In an observation, the PSF convolution is described more precisely by

$$(\mathrm{PSF} \otimes I) + \epsilon_I = I^{\mathrm{obs}} \qquad (6.3)$$

with the noise ϵ. For an intensity image this should be dominated by detector readout, photon or thermal noise. In case of a subtracted image

$$(\mathrm{PSF} \otimes Q) + \epsilon_Q = Q^{\mathrm{obs}} \qquad (6.4)$$

the noise ϵ_Q partly consists of $\sqrt{2}\epsilon_I$ from statistical error propagation, but additional alignment errors contribute significantly to the total error, so that $\epsilon_Q \gg \epsilon_I$. As in case of a wire polarizer the image is shifted a few pixels depending on grid alignment, even after carefully shifting the images back with sub-pixel precision a residual error remains. The deconvolution estimation now strongly depends on the signal to noise ratio and also on the shape of the noise, i.e. the frequency spectrum of the Fourier transform. Deconvolution algorithms normally apply filters, such as the Wiener filter, to suppress high frequencies. But even with iterative algorithms like Lucy-Richardson a higher ϵ will significantly degrade the estimated Q image. Therefore the deconvolution was applied on the I images with the PSFs obtained from the field.

For the beam reconstruction the deconvolved intensity images were convolved with a Gaussian of 0.25" FWHM, before the polarization degree images are generated. The diffraction limit at K-band is 0.15" for the 3.6m telescope (Eqn. 1.15), but under moderate seeing conditions and low Strehl ratios as

---

[2]for a comparison of different deconvolution techniques see Schödel (2004), e.g.
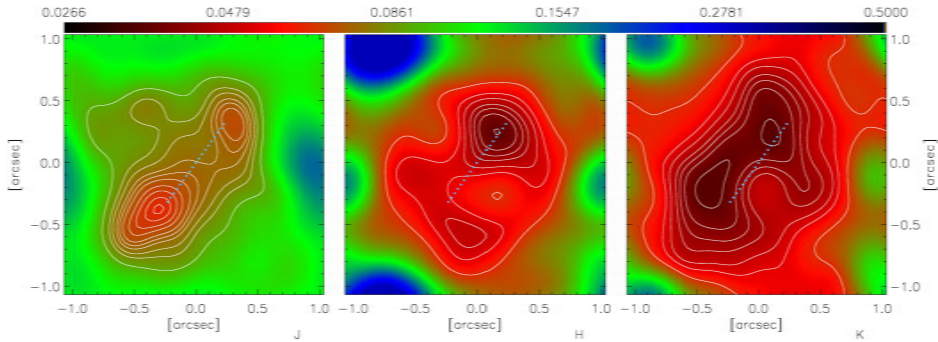
Figure 6.5: *Polarization degree images of 177-341 in J-, H- and K-band (from left to right). As the polarization degree is very sensitive to PSF-effects, the polarization images were deconvolved before. The PSFs estimated from point sources in the observed field were used for the deconvolution. The polarization degree images are then smoothed with a Gaussian of 0.16" -0.3" FWHM. An elongated region of low polarization can be identified in all bands. This confirms the proposed disk P.A. (blue dotted line). There is also some evidence for an outflow, as higher polarization is visible in a line perpendicular to the disk.*

given for these observations (cf. Sect. 4.3.1) an empirical limit for the achieved resolution is 1.5–2 diffraction limit units (Bonaccini et al. 1997). Without this smoothing the deconvolved images are also dominated by high frequency noise features, that are enhanced progressively with the number of iterations (Lantéri et al. 1999). The algorithm converges fastest at the brightest source structures (Lucy 1974). Therefore choosing a too small number of iterations results in images of undefined resolution and quality. Experiences with the algorithm (Ott et al. 1999) suggest 10^3 iterations for the case of a single star dominating a single circumstellar structure.

The results shown in figure 6.5 fit perfectly in the model of this giant pro-plyds and the attenuation of polarization in the dense regions of the disk. However, it should be noted that the elongation of the PSFs in direction of θ^1 C (P.A. $\sim 134°$) could be responsible for the elongated dark spot in the polarization maps (P.A. $\sim 144°$). The analysis of PSF convolved images of simulations shows, that dark spots can be reproduced in the direction of elongation regardless the P.A. of the disk, as discussed in chapter 5.3.2. But the extent of the region of 300AU clearly exceeds the PSF dimensions at least in K-band. Nevertheless it was tried to eliminate the elongation effects as much as possible at the deconvolution of the individual frames and the determined P.A. is consistent with other tests as discussed in the following chapter.
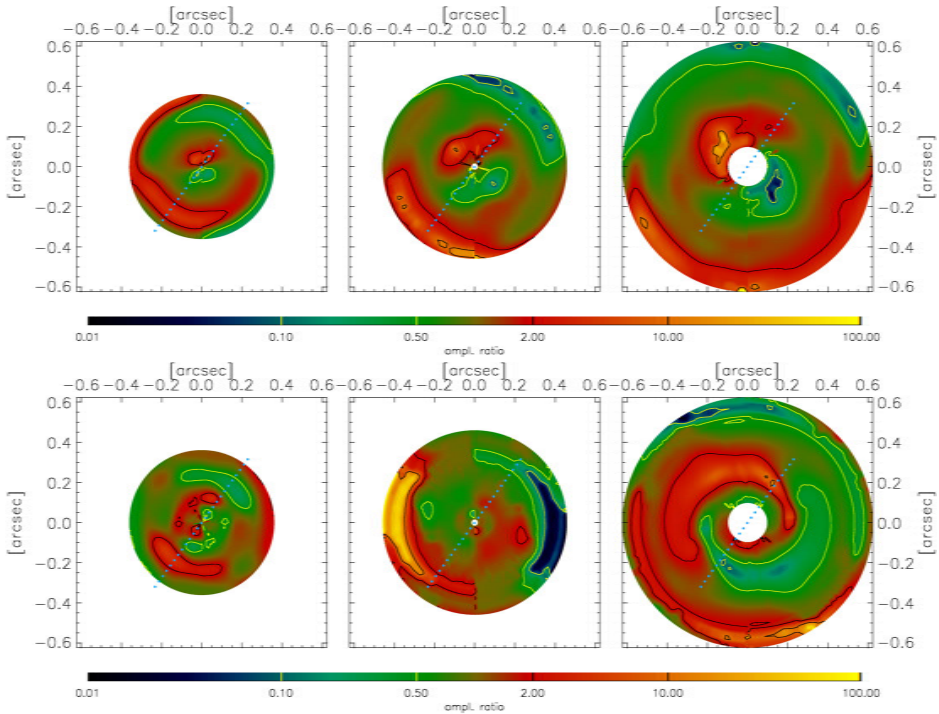
Figure 6.6: *Plot of the test of the inclination of the disk: the amplitudes of the polarization profile (cf. Fig. 4.18) are attenuated due to the multiple scattering in the disk. If the disk is inclined, the amplitude of the part with the disk in front is more affected. Therefore the ratio of the amplitudes ("in front" divided by "behind") is minimal. Here the maps of the amplitudes ratio in J- H- and K-band (from left to right) is shown in an annulus determined from the radial profiles for Q (top) and U (bottom). The position angle for the disk can be located around 144° and is marked with the blue dotted line. The high ratios in the outer regions visible in H-band are likely due to alignment errors and asymmetry noise contributions.*

6.4 Polarization ratio maps

A closer look at the Q and U profiles in figure 4.18 reveals a modulation in the amplitudes. This modulation is also dependent on the radial range or annulus used for the profile.

In figure 6.6 the maps of the ratio of the amplitude as a function of P.A. and radius are plotted. The generation of this data is described in chapter 5.4.3. These maps can emphasize disk parameters even under distortion by elliptic PSFs.

In this view spots of extremal ratios are found along the proposed P.A. of the disk ($\sim$144°). The maximum values are located to the north-east and the minimum to the south-west. The spots are clearly seen in H- and K-band with
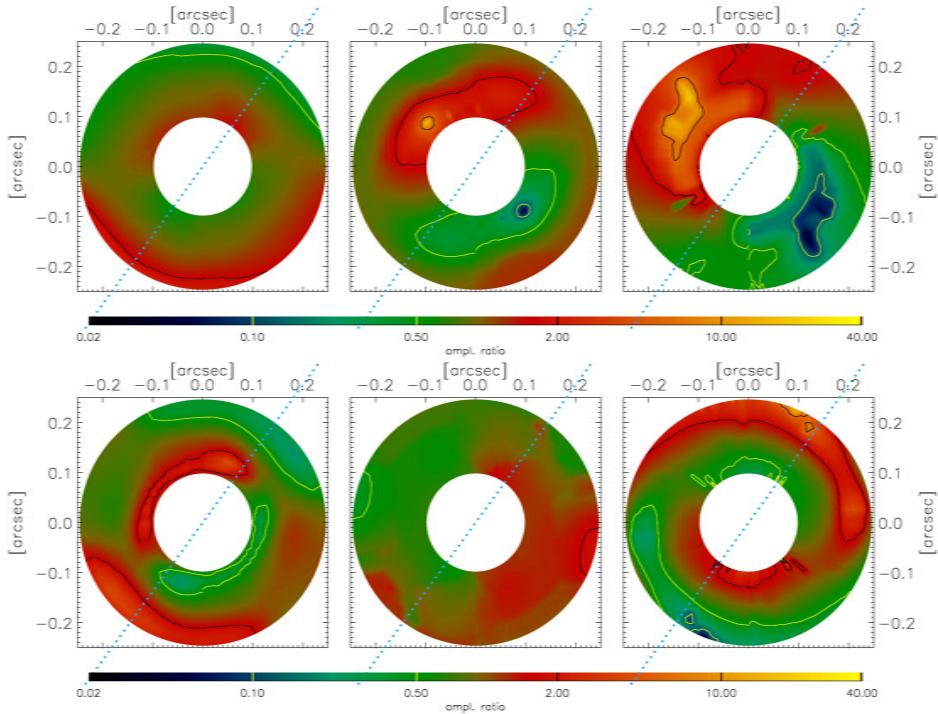
Figure 6.7: *Same as figure 6.6, but in an annulus of 0.1"–0.25". In this radial range the amplitude signal is high, at least in H- and K-band. The radius of the minimum spots ratio can be determined to ~0.12" in Q. The U-ratios show no significant modulation in this range.*

nearly the same radial distance to the center. The high ratios in the outer region in H-band is due to noise and possible alignment errors, as the polarization amplitude here is very low. The ranges in this plot are chosen include all significant centrosymmetric polarization, according to figure 4.18. For reliable tests of the amplitude ratios the amplitudes have to be reasonably high. The ranges plotted in figure 6.7 are therefore chosen to include only the strong polarization amplitudes.

The elongation of the PSFs with a P.A. of ~134° justifys the consideration of the Q-ratio maps. As shown in section 5.4.3 the disk plane should be located in a region with high amplitude of the carrier signal, so the Q-map is preferred. This is confirmed by the evidence of stronger tidal-like features in the U-maps, which apparently are artefacts of the convolution (cf. Figs. 5.11–5.13).

If the interpretation of polarization attenuation by the dense disk is correct, an inclination of the disk is implicated. If a flared disk or disk of great scale height were seen purely edge-on, which is probable according to the optical
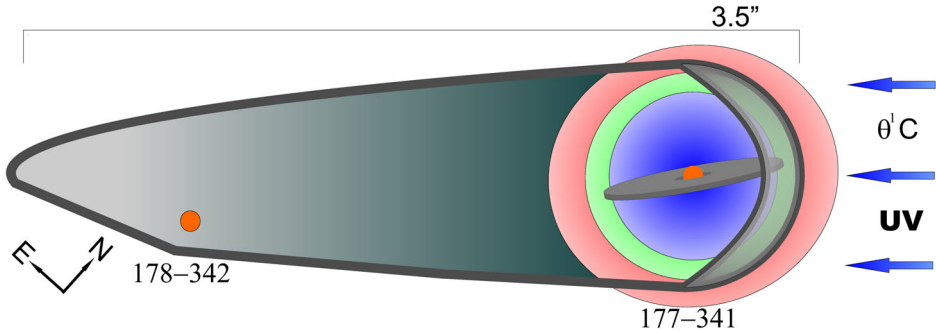
Figure 6.8: *Schematic overview of our model and results for the proplyds 177-341 and 178-342. 177-341 has an inclined disk and an illuminated dust envelope. The diameter, inclination and P.A. of the disk is drawn according to the MC simulation results. The size of the dust envelope is obtained from the polarimetric differential images (Fig. 4.18) and is comparable to the diameter of the ionization fronts head in the optical (Fig. 4.12, right). 178-342 has no resolvable dust distribution, as the images in Fig. 4.18 show.*

images, the Q and U amplitudes should be evenly attenuated in opposed regions and the ratio is not affected. With this result the disk is constrained to lie in front of the central star to the south west, which means a positive inclination angle[3].

The radial distance of the spots constrains the inclination angle even further. If one thinks about an inclined disk in projection as an ellipse, the radial distance of the spots represents the semi-minor axis. However, in this relation the height of the disk is not considered: the model is consistent only for flat, optical thick disks. If a radius of $a = 0.35''$ and a flat disk is assumed, the shape of the ellipse is set and the minimum inclination angle is given by $\xi = \arccos(b/a) \approx 70°$. When considering the height of the (flared) disk, this value is increased. This can be seen in figure 5.13, where the flared disk produces a greater extent as the flat disk for the same inclination. This results in an estimated possible inclination range of about $75°$–$85°$, as the disk has to be inclined according to the signature in the ratio maps. The values of maximum ratios increase from J- to K-band. This can be interpreted as a stronger relative attenuation of the disk at higher wavelength. Since the polarization is lower in K-band the total attenuation might be constant.

6.5 Conclusion

Polarized emission maps of the circumstellar dust distribution of the giant proplyd 177-341 were presented and a complex morphology including both a cir-

---

[3]depending on the definition of the inclination angle in relation to the P.A.

cumstellar envelope and an accretion disk were found.

The size of the disk was estimated with the diameter of the IF and confirmed in the polarization degree images. We extracted the inclination of the disk from a detailed study of the polarization profiles in the Stokes images. For the P.A. of the disk we presented evidence of part of the disk seen in silhouette in the optical images and we find matching position angles in the polarization amplitudes ratio (Fig. 6.6) and in the polarization degree images due to multiple scattering in the disk.

When considering the constraints on the disk and envelope configuration from previous observations as discussed in section 6.1 a good agreement of the parameters with the polarimetric analysis is found. With the obtained values for the envelope size and the size, P.A. and inclination of the disk the simulations show similar polarization images. The position angle of the disk relative to the source of UV radiation ($\Delta \approx 10°$) is probably the reason for the peculiar shape and size of the IF of 177-341. The diameter of the disk is still very big, suggesting a very young proto-star in accretion phase, or a less efficient disk eroding by the UV under this small hitting angle. A schematic view summarizing the results of the envelope and disk configuration is given in figure 6.8.

The fitting of the profile along the position angle takes advantage of the slightest modulation in polarization by considering a whole 180°-segment. With this technique a high spatial resolution is achieved by evaluation of the impact of small spatial structures (the disk) in the signal of larger structures (the scattering in the envelope). This is an great example of how polarimetry can substantially improve the limits imposed by the sensitivity and spatial resolution of an instrument.

The same applies for the deconvolution. It was shown, that PSF effects can strongly affect the polarimetric results. A carefully conducted deconvolution significantly reduces the false polarization signatures due to distorted PSFs. In the 4m-class data it was shown, that the technique of ground based differential polarimetric imaging is suitable to map the dust emission very close to the central star (here about 0.1"). This is the case for the largest and brightest proplyds in the Trapezium. In future observations this technique in conjunction with increased achievable resolution could map even substructures of circumstellar disks of the proplyds. For example the PEPSI spectrograph at the LBT (Fig. 1.7) will provide polarimeters at each telescope to observe the two Stokes parameters Q and U at the same time. The proplyds 158-326 and 166-316 are best-suited candidates to be observed with 8m-class telescopes, as these show extended emission and a modulated trefoil pattern in the polarimetric differential images. The application of new technology AO systems such as MCAO (cf. Sect. 1.5.1) will significantly

reduce PSF degradation effects across the FoV and help to improve the quality of polarimetric imaging observations.

The comparison of different dust models for the grain size distribution and scattering properties around 177-341 showed no clear results. The models for dense clouds with high R_V give better results for the peculiar spectral polarization dependence. The increasing polarization pattern extent from J- to K-band may be a hint to grain growth in the disk as a simple model with large grains in the disk region indicates. But another mechanism must be present to account for the observed features. In the simple model the surrounding nebula contribution to polarized emission is missing. With low opacities in K-band, the light from the central star could be forward-scattered in the outer regions of the envelope. In these regions the TSC-density is low, but the nebular density might become relevant.

For the modeling, outflows and cavities were ignored, although at least some evidence for the presence of such features is given by the optical images (Fig. 6.2). Also polarization features like a higher polarization line in the polarization degree images (Fig. 6.5) and some spots in the amplitudes ratio maps (Fig. 6.6) could be interpreted as an outflow, resulting in a very complex morphology of the proplyd. Nevertheless the simple model is well-suited to derive disk parameters and it can be adapted to observed features in future surveys.

Abbreviations

2MASS	Two Micron All Sky Survey
ACS	advanced camera for surveys (HST)
ADC	atmospheric dispersion compensator
ADONIS	Adaptive Optics Near Infrared System (3.6m)
AM	amplitude modulation
AO	Adaptive Optics
AU	astronomical unit
BIBO	bounded input, bounded output stability
BN	Becklin-Neugebauer object
CfAO	Center for Adaptive Optics
CIAO	Coronographic Imager with Adaptive Optics (Subaru)
CONICA	Coudée Near Infrared Camera
CTIO	Cerro Tololo Inter-American Observatory
DIMM	Differential Image Motion Monitor
DIT	detector integration time
DM	deformable mirror
DPU	detector positioning unit
E-ELT	European Extremely Large Telescope
ESO	European Southern Observatory
FFTS	Fringe and Flexure Tracking System
FIR	far-infrared
FLWO	Fred Lawrence Whipple Observatory
FoV	field of view
FPA	focal plane array
FWHM	full width at half maximum
FWTM	full width at tenth maximum
GMT	Giant Magellan Telescope
GWS	ground-layer wavefront sensor
HAWAII	HgCdTe Astronomical Wide Area Infrared Imager
HgCdTe	mercury cadmium telluride (semiconductor)
HH	Herbig-Haro object
HST	Hubble Space Telescope
IAC	Instituto de Astrofisica de Canarias
IDL	Interactive Data Language (software)

IF	ionization front
IMF	Initial Mass Function
IR	infrared
IRPOL	Infra-Red Polarimetry facility (UKIRT)
ISM	interstellar medium
KMH	Kim, Martin & Hendry (grain size distribution)
LBT	Large Binocular Telescope
LGS	Laser Guide Star
LINC	LBT Interferometric Camera
LOST	Layer-oriented simulation tool
LTI	linear time-invariant dynamical system
LUT	look-up table
mas	milli-arcsecond
MAX	Mid infrared Array eXpandible (UKIRT)
MC	Monte Carlo (simulation)
MCAO	Multi-Conjugate Adaptive Optics
MEM	maximum entropy method
MHWS	mid/high-layer wavefront sensor
MIR	mid-infrared
MPE	Max-Planck-Institut für extraterrestrische Physik, Garching
MPfIR	Max-Planck-Institut für Radioastronomie, Bonn
MPIA	Max-Planck-Institut für Astronomie, Heidelberg
MRN	Mathis, Rumpl & Nordsieck (grain size distribution)
NACO	NAOS-CONICA (VLT)
NAOS	Nasmyth Adaptive Optics
NICMOS	Near-Infrared Camera and Multi-Object Spectrometer
NIR	near-infrared
NIRVANA	Near-IR Visible Adaptive Interferometer for Astronomy (LBT)
NOAO	National Optical Astronomy Observatory
NTT	New Technology Telescope
ONC	Orion Nebula Cluster
OPD	optical path difference
OTF	optical transfer function
P.A.	position angle
PDI	polarimetric differential image
PED	power law with exponential decay
PEM	prediction error method
PEPSI	Potsdam Echelle Polarimetric and Spectroscopic Instrument
PID	proportional-integral-derivative

PMS	premain-sequence
proplyd	proto-planetary disk
PSD	power-spectral densitiy
PSF	point spread function
PTV	peak-to-valley
PZT	lead (Pb) zirconate titanate, a piezoelectric ceramic
RMS	root mean square
SCIDAR	scintillation detection and ranging
SED	spectral energy distribution
SHARP	System for High-Angular-Resolution Pictures (3.6m)
SMP	symmetric multiprocessing
SNR	signal-to-noise ratio
TMT	Thirty-Meter Telescope
TSC	Terebey, Shu & Cassen (model of collapsing envelopes)
TTS	(classical) T-Tauri star
UIST	United Kingdom Infrared Telescope Imaging Spectrometer (UKIRT)
UKIRT	United Kingdom Infrared Telescope
VLT	Very Large Telescope
WFC	wide field camera (HST)
WFPC2	wide field and planetary camera 2 (HST)
WFS	wavefront sensor
YSO	young stellar object
ZOH	zero-order-hold

Bibliography

Ageorges, N., Eckart, A., Hofmann, R., & Stecklum, B. 1996, *Near-Infrared Two Dimensional Speckle Polarimetric Imaging*, in Astronomical Society of the Pacific Conference Series, Vol. 97, Polarimetry of the Interstellar Medium, ed. W. G. Roberge & D. C. B. Whittet, 85–+

Ageorges, N., Eckart, A., Monin, J.-L., & Menard, F. 1997, *New multiple young stellar objects discovered by near-infrared speckle imaging.*, A&A, 326, 632

Ageorges, N. & Walsh, J. R. 1999, *Acquisition and analysis of adaptive optics imaging polarimetry data*, A&AS, 138, 163

André, P. 1994, *Observations of protostars and protostellar stages*, in The Cold Universe, ed. T. Montmerle, C. J. Lada, I. F. Mirabel, & J. Tran Thanh van, 179–+

Andre, P., Ward-Thompson, D., & Barsony, M. 1993, *Submillimeter continuum observations of Rho Ophiuchi A - The candidate protostar VLA 1623 and prestellar clumps*, ApJ, 406, 122

Angerhausen, D., Krabbe, A., & Iserlohe, C. 2007, *Phase-differential NIR integral field spectroscopy of HD209458b*, in Astronomical Society of the Pacific Conference Series, Vol. 366, Transiting Extrapolar Planets Workshop, ed. C. Afonso, D. Weldrake, & T. Henning, 262–+

Apai, D., Pascucci, I., Brandner, W., Henning, T., Lenzen, R., Potter, D. E., Lagrange, A.-M., & Rousset, G. 2004, *NACO polarimetric differential imaging of TW Hya. A sharp look at the closest T Tauri disk*, A&A, 415, 671

Arcidiacono, C. 2005, *MCAO simulations*, Tech. Rep. LN-INAFA-FDR-AO-003, MPIA, Heidelberg, Germany

Arcidiacono, C., Diolaiti, E., Tordi, M., Ragazzoni, R., Farinato, J., Vernet, E., & Marchetti, E. 2004, *Layer-Oriented Simulation Tool*, Appl. Opt., 43, 4288

Avila, R., Vernin, J., & Sánchez, L. J. 2001, *Atmospheric turbulence and wind profiles monitoring with generalized scidar*, A&A, 369, 364

Babcock, H. W. 1953, *The Possibility of Compensating Astronomical Seeing*, PASP, 65, 229

Bally, J. 2003, *Star and Planet Formation Near OB Stars (Invited Review)*, in ASP Conf. Ser. 287: Galactic Star Formation Across the Stellar Mass Spectrum, ed. J. M. De Buizer & N. S. van der Bliek, 263–274

Bally, J., Cunningham, N., Moeckel, N., & Smith, N. 2005, *Nearby regions of massive star formation*, in IAU Symposium, Vol. 227, Massive Star Birth: A Crossroads of Astrophysics, ed. R. Cesaroni, M. Felli, E. Churchwell, & M. Walmsley, 12–22

Bally, J., O'Dell, C. R., & McCaughrean, M. J. 2000, *Disks, Microjets, Windblown Bubbles, and Outflows in the Orion Nebula*, AJ, 119, 2919

Bally, J., Sutherland, R. S., Devine, D., & Johnstone, D. 1998, *Externally Illuminated Young Stellar Environments in the Orion Nebula: Hubble Space Telescope Planetary Camera and Ultraviolet Observations*, AJ, 116, 293

Bastien, P. & Menard, F. 1988, *On the interpretation of polarization maps of young stellar objects*, ApJ, 326, 334

Bertram, T. 2007a, *Cophasing LINC-NIRVANA and Molecular gas in low-luminosity QSO host and cluster galaxies*, PhD thesis, Mathematisch-Naturwissenschaftliche Fakultät der Universität zu Köln, Germany. IX + 174 pp. (2007)

—. 2007b, *FFTS Software*, Tech. Rep. LN-KOELN-SWDR-ICS-001, PH1, Cologne, Germany

Bertram, T., Arcidiacono, C., Straubmeier, C., Rost, S., Wang, Y., & Eckart, A. 2006, *The LINC-NIRVANA fringe and flexure tracker: image analysis concept and fringe tracking performance estimate*, in Presented at the Society of Photo-Optical Instrumentation Engineers (SPIE) Conference, Vol. 6268, Advances in Stellar Interferometry. Edited by Monnier, John D.; Schöller, Markus; Danchi, William C.. Proceedings of the SPIE, Volume 6268, pp. 62683P (2006).

Bessell, M. S. & Brett, J. M. 1988, *JHKLM photometry - Standard systems, passbands, and intrinsic colors*, PASP, 100, 1134

Beuzit, J.-L., Hubin, N., Gendron, E., Demailly, L., Gigan, P., Lacombe, F., Chazallet, F., Rabaud, D., & Rousset, G. 1994, *ADONIS: a user-friendly*

adaptive optics system for the ESO 3.6-m telescope, in Presented at the Society of Photo-Optical Instrumentation Engineers (SPIE) Conference, Vol. 2201, Proc. SPIE Vol. 2201, p. 955-961, Adaptive Optics in Astronomy, Mark A. Ealey; Fritz Merkle; Eds., ed. M. A. Ealey & F. Merkle, 955–961

Bonaccini, D., Prieto, E., Corporon, P., Christou, J. C., Le Mignan, D., Prado, P. D., Gredel, R., & Hubin, N. N. 1997, *Performance of the ESO AO system, ADONIS, at the La Silla 3.6-m telescope [3126-78]*, in Presented at the Society of Photo-Optical Instrumentation Engineers (SPIE) Conference, Vol. 3126, Proc. SPIE Vol. 3126, Adaptive Optics and Applications, Robert K. Tyson and Robert Q. Fugate, Eds., p.589, ed. R. K. Tyson & R. Q. Fugate, 589–+

Bonnell, I. A. & Bate, M. R. 2005, *Binary systems and stellar mergers in massive star formation*, MNRAS, 362, 915

—. 2006, *Star formation through gravitational collapse and competitive accretion*, MNRAS, 370, 488

Bonnell, I. A., Bate, M. R., & Zinnecker, H. 1998, *On the formation of massive stars*, MNRAS, 298, 93

Boogert, A. C. A., Tielens, A. G. G. M., Ceccarelli, C., Boonman, A. M. S., van Dishoeck, E. F., Keane, J. V., Whittet, D. C. B., & de Graauw, T. 2000, *Infrared observations of hot gas and cold ice toward the low mass protostar Elias 29*, A&A, 360, 683

Brand, J. 2007, *Massive star formation in the Galaxy*, Memorie della Societa Astronomica Italiana, 78, 665

Brix, M. & Naranjo, V. 2008, *LBT Vibration Measurements, Influence of Actuators/Telescope modes on the vibration behavior*, Tech. Rep. LN-MPIA-TN-MECH-010, MPIA, Heidelberg, Germany

Butler, R. P., Wright, J. T., Marcy, G. W., Fischer, D. A., Vogt, S. S., Tinney, C. G., Jones, H. R. A., Carter, B. D., Johnson, J. A., McCarthy, C., & Penny, A. J. 2006, *Catalog of Nearby Exoplanets*, ApJ, 646, 505

Caccia, J. L., Azouit, M., & Vernin, J. 1987, *Wind and C(N)-squared profiling by single-star scintillation analysis*, Appl. Opt., 26, 1288

Chandrasekhar, S. 1939, An introduction to the study of stellar structure (Chicago, Ill., The University of Chicago press [1939])

—. 1950, Radiative transfer. (Oxford, Clarendon Press, 1950.)

Chen, B. M., Lee, T. H., Hang, C. C., Guo, Y., & Weerasooriya, S. 1999, *An H^∞ almost disturbance decoupling robust controller design for a piezoelectric bimorph actuator with hysteresis*, IEEE Trans. Contr. Syst. Technol., 40, 160

Clarke, C. J., Harper-Clark, E., & Lodato, G. 2007, *The response of self-gravitating protostellar discs to slow reduction in cooling time-scale: the fragmentation boundary revisited*, MNRAS, 381, 1543

Cohen, M. 1983, *HL Tauri and its circumstellar disk*, ApJ, 270, L69

Cornette, W. M. & Shanks, J. G. 1992, *Physically reasonable analytic expression for the single-scattering phase function*, Appl. Opt., 31, 3152

Cox, A. N., ed. 1999, Allen's Astrophysical Quantities (AIP press), 262

Cresci, G., Davies, R. I., Baker, A. J., & Lehnert, M. D. 2005, *Accounting for the anisoplanatic point spread function in deep wide-field adaptive optics images*, A&A, 438, 757

D'Alessio, P., Canto, J., Calvet, N., & Lizano, S. 1998, *Accretion Disks around Young Objects. I. The Detailed Vertical Structure*, ApJ, 500, 411

Davis, L. J. & Greenstein, J. L. 1951, *The Polarization of Starlight by Aligned Dust Grains.*, ApJ, 114, 206

Dent, W. R. F., Torrelles, J. M., Osorio, M., Calvet, N., & Anglada, G. 2006, *The circumstellar disc around the Herbig AeBe star HD169142*, MNRAS, 365, 1283

Diolaiti, E., Bendinelli, O., Bonaccini, D., Close, L., Currie, D., & Parmeggiani, G. 2000, *Analysis of isoplanatic high resolution stellar fields by the StarFinder code*, A&AS, 147, 335

Dormand, J. & Prince, P. 1980, *A family of embedded Runge-Kutta formulae*, Journal of Computational and Applied Mathematics, 19

Doyle, J. C., Glover, K., Khargonekar, P., & Francis, B. 1989, *State-space solutions to standard H_2 and H_∞ control problems*, IEEE Transactions on Automatic Control, 34, 831

Eckart, A. & Duhoux, P. R. M. 1990, *Infrared Speckle Reduction Software at the MPE*, in ASP Conf. Ser. 14: Astrophysics with Infrared Arrays, ed. R. Elston, 336–+

Egner, S. 2006, *Multi-Conjugate Adaptive Optics for LINC-NIRVANA – Laboratory tests of a Ground-Layer Adaptive Optics System and Vertical Turbulence Measurements at Mt. Graham*, PhD thesis, Ruperto-Carola University of Heidelberg, Germany

Egner, S. E., Masciadri, E., & McKenna, D. 2007, *Generalized SCIDAR Measurements at Mount Graham*, PASP, 119, 669

Elsasser, H. & Staude, H. J. 1978, *On the Polarization of Young Stellar Objects*, A&A, 70, L3+

Fried, D. L. 1965, *Statistics of a Geometric Representation of Wavefront Distortion*, Journal of the Optical Society of America (1917-1983), 55, 1427

—. 1966, *Optical resolution through a randomly inhomogeneous medium for very long and very short exposures,*, J. Opt. Soc. Am., 56, 1372

—. 1977, *Least-square fitting a wave-front distortion estimate to an array of phase-difference measurements*, Journal of the Optical Society of America (1917-1983), 67, 370

Fuchs, A., Tallon, M., & Vernin, J. 1998, *Focusing on a Turbulent Layer: Principle of the "Generalized SCIDAR"*, PASP, 110, 86

Fusco, T., Conan, J.-M., Mugnier, L. M., Michau, V., & Rousset, G. 2000, *Characterization of adaptive optics point spread function for anisoplanatic imaging. Application to stellar field deconvolution*, A&AS, 142, 149

Genzel, R., Reid, M. J., Moran, J. M., & Downes, D. 1981, *Proper motions and distances of H2O maser sources. I - The outflow in Orion-KL*, ApJ, 244, 884

Genzel, R. & Stutzki, J. 1989, *The Orion Molecular Cloud and star-forming region*, ARA&A, 27, 41

Hales, A. S., Gledhill, T. M., Barlow, M. J., & Lowe, K. T. E. 2006, *Near-infrared imaging polarimetry of dusty young stars*, MNRAS, 365, 1348

Hardy, J. W. 1998, Adaptive Optics for Astronomical Telescopes (Adaptive Optics for Astronomical Telescopes, by John W Hardy, pp. 448. Foreword by John W Hardy. Oxford University Press, Jul 1998. ISBN-10: 0195090195. ISBN-13: 9780195090192)

Hashimoto, J., Tamura, M., Suto, H., Abe, L., Ishii, M., Kudo, T., & Mayama, S. 2007, *Subarcsecond Near-Infrared Images of Massive Star Formation Region NGC 6334V*, PASJ, 59, 221

Healy, K. R., Hester, J. J., & Claussen, M. J. 2004, *A Very Large Array Search for Water Masers in Six H II Regions: Tracers of Triggered Low-Mass Star Formation*, ApJ, 610, 835

Henney, W. J. 2000, *Kinematics and Ionization of the Proplyd M42 177-341*, in Revista Mexicana de Astronomia y Astrofisica Conference Series, ed. S. J. Arthur, N. S. Brickhouse, & J. Franco, 198–200

Henney, W. J. & O'Dell, C. R. 1999, *A Keck High-Resolution Spectroscopic Study of the Orion Nebula Proplyds*, AJ, 118, 2350

Henyey, L. G. & Greenstein, J. L. 1941, *Diffuse radiation in the Galaxy*, ApJ, 93, 70

Herbst, T. 2005, *LINC-NIRVANA Error Budget*, Tech. Rep. LN-MPIA-FDR-GEN-001, MPIA, Heidelberg, Germany

Herbst, T. M., Ragazzoni, R., Eckart, A., & Weigelt, G. 2004, *The LINC-NIRVANA interferometric imager for the Large Binocular Telescope*, in Presented at the Society of Photo-Optical Instrumentation Engineers (SPIE) Conference, Vol. 5492, Ground-based Instrumentation for Astronomy. Edited by Alan F. M. Moorwood and Iye Masanori. Proceedings of the SPIE, Volume 5492, pp. 1045-1052 (2004)., ed. A. F. M. Moorwood & M. Iye, 1045–1052

Hester, J. J. & Desch, S. J. 2005, *Understanding Our Origins: Star Formation in HII Region Environments*, in ASP Conf. Ser. 341: Chondrites and the Protoplanetary Disk, ed. A. N. Krot, E. R. D. Scott, & B. Reipurth, 107–+

Hill, J. M., Green, R. F., & Slagle, J. H. 2006, *The Large Binocular Telescope*, in Presented at the Society of Photo-Optical Instrumentation Engineers (SPIE) Conference, Vol. 6267, Ground-based and Airborne Telescopes. Edited by Stepp, Larry M.. Proceedings of the SPIE, Volume 6267, pp. 62670Y (2006).

Hillenbrand, L. A., Strom, S. E., Calvet, N., Merrill, K. M., Gatley, I., Makidon, R. B., Meyer, M. R., & Skrutskie, M. F. 1998, *Circumstellar Disks in the Orion Nebula Cluster*, AJ, 116, 1816

Hofmann, R., Blietz, M., Duhoux, P., Eckart, A., Krabbe, A., & Rotaciuc, V. 1992, *SHARP and FAST: NIR Speckle and Spectroscopy at MPE*, in Progress in Telescope and Instrumentation Technologies, ed. M.-H. Ulrich, 617–+

Huélamo, N., Brandner, W., & Wolf, S. 2007, *Polarimetric differential imaging of the protostar Elias-29*, in Revista Mexicana de Astronomia y Astrofisica,

vol. 27, Vol. 29, Revista Mexicana de Astronomia y Astrofisica Conference Series, 149–149

Huélamo, N., Brandner, W., Wolf, S., & Khanzadyan, T. 2005, *Polarimetric Differential Imaging of the Class I Protostar Elias 2-29 with NACO/VLT*, in Protostars and Planets V, 8209–+

Hughes, A. M., Wilner, D. J., Qi, C., & Hogerheijde, M. R. 2008, *Gas and Dust Emission at the Outer Edged of Protoplanetary Disks*, accepted for publication in ApJ

Isermann, R. 1992, Identifikation dynamischer Systeme: Grundlegende Methoden. 2. Auflage (Springer, Berlin)

Jeffries, R. D. 2007, *The distance to the Orion Nebula cluster*, MNRAS, 376, 1109

Jiang, Z., Tamura, M., Fukagawa, M., Hough, J., Lucas, P., Suto, H., Ishii, M., & Yang, J. 2005, *A circumstellar disk associated with a massive protostellar object*, Nature, 437, 112

Johnstone, D., Hollenbach, D., & Bally, J. 1998, *Photoevaporation of Disks and Clumps by Nearby Massive Stars: Application to Disk Destruction in the Orion Nebula*, ApJ, 499, 758

Kalman, R. E. 1960, *A New Approach to Linear Filtering and Prediction Problems*, Transactions of the ASME - Journal of Basic Engineering, 82, 35

Kellerer, A. & Tokovinin, A. 2007, *Atmospheric coherence times in interferometry: definition and measurement*, A&A, 461, 775

Kemball, A. 2002, *Observational studies of maser polarization*, in IAU Symposium, Vol. 206, Cosmic Masers: From Proto-Stars to Black Holes, ed. V. Migenes & M. J. Reid, 359–+

Kim, S.-H., Martin, P. G., & Hendry, P. D. 1994, *The size distribution of interstellar dust particles as determined from extinction*, ApJ, 422, 164

Kissler-Patig, M., Wilson, T., Bastian, N., D'Antona, F., de Grijs, R., Froebrich, D., Galliano, E., Grosbøl, P., Johnson, K., Keto, E., Klessen, R., Megeath, T., Rejkuba, M., Steinacker, J., & Zinnecker, H. 2007, *12 Questions on Star and Massive Star Cluster Formation*, The Messenger, 129, 69

Kolmogorov, A. N. 1961, *The local structure of turbulence in incompressible viscous fluids for very large Reynolds numbers*, in Turbulence, Classic Papers on Statistical Theory, ed. S. K. Friedlander & L. Topper (New York: Wiley-Interscience), 151–155

Kornilov, V., Tokovinin, A., Shatsky, N., Voziakova, O., Potanin, S., & Safonov, B. 2007, *Combined MASS-DIMM instruments for atmospheric turbulence studies*, MNRAS, 382, 1268

Krumholz, M. R. 2006, *Massive Star Formation: A Tale of Two Theories*, in Astronomical Society of the Pacific Conference Series, Vol. 352, New Horizons in Astronomy: Frank N. Bash Symposium, ed. S. J. Kannappan, S. Redfield, J. E. Kessler-Silacci, M. Landriau, & N. Drory, 31–+

Kuhn, J. R., Potter, D., & Parise, B. 2001, *Imaging Polarimetric Observations of a New Circumstellar Disk System*, ApJ, 553, L189

La Camera, A., Desiderá, G., Arcidiacono, C., Boccacci, P., & Bertero, M. 2007, *Advances in the reconstruction of LBT LINC-NIRVANA images*, A&A, 471, 1091

Lada, C. J. 1987, *Star formation - From OB associations to protostars*, in IAU Symposium, Vol. 115, Star Forming Regions, ed. M. Peimbert & J. Jugaku, 1–17

Lada, C. J., Muench, A. A., Haisch, Jr., K. E., Lada, E. A., Alves, J. F., Tollestrup, E. V., & Willner, S. P. 2000, *Infrared L-Band Observations of the Trapezium Cluster: A Census of Circumstellar Disks and Candidate Protostars*, AJ, 120, 3162

Lada, C. J., Muench, A. A., Lada, E. A., & Alves, J. F. 2004, *Deep 3.8 Micron Observations of the Trapezium Cluster*, AJ, 128, 1254

Lantéri, H., Soummer, R., & Aime, C. 1999, *Comparison between ISRA and RLA algorithms. Use of a Wiener Filter based stopping criterion*, A&AS, 140, 235

Laun, W., Baumeister, H., & Bizenberger, P. 2006, *The LINC-NIRVANA IR cryostat*, in Presented at the Society of Photo-Optical Instrumentation Engineers (SPIE) Conference, Vol. 6269, Ground-based and Airborne Instrumentation for Astronomy. Edited by McLean, Ian S.; Iye, Masanori. Proceedings of the SPIE, Volume 6269, pp. 626956 (2006).

Le Roux, B., Ragazzoni, R., Arcidiacono, C., Conan, J.-M., Kulcsar, C., & Raynaud, H.-F. 2004, *Kalman-filter-based optimal control law for star-oriented and layer-oriented multiconjugate adaptive optics*, in Presented at the Society of Photo-Optical Instrumentation Engineers (SPIE) Conference, Vol. 5490, Advancements in Adaptive Optics. Edited by Domenico B. Calia, Brent L. Ellerbroek, and Roberto Ragazzoni. Proceedings of the SPIE, Volume 5490, pp. 1336-1346 (2004)., ed. D. Bonaccini Calia, B. L. Ellerbroek, & R. Ragazzoni, 1336–1346

Lee, H.-T. & Chen, W. P. 2007, *Triggered Star Formation by Massive Stars*, ApJ, 657, 884

Lesurf, J. C. G., ed. 2001, Information and Measurement, 2nd Edition (CRC press)

Ljung, L. 2002, *Prediction error estimation methods*, Circuits, Systems, and Signal Processing, 21, 11

Lucy, L. B. 1974, *An iterative technique for the rectification of observed distributions*, AJ, 79, 745

Mathis, J. S., Rumpl, W., & Nordsieck, K. H. 1977, *The size distribution of interstellar grains*, ApJ, 217, 425

Mathis, J. S. & Wallenhorst, S. G. 1981, *The size distribution of interstellar particles. III - Peculiar extinctions and normal infrared extinction*, ApJ, 244, 483

Maxwell, J. C. 1868, *On Governors*, Proceedings of the Royal Society of London, 16, 270

McCabe, C. & Stapelfeldt, K. R. 2007, *Circumstellardisks.org: An Online Database of Spatially Resolved Circumstellar Disks*, in Proceedings of the conference In the Spirit of Bernard Lyot: The Direct Detection of Planets and Circumstellar Disks in the 21st Century. June 04 - 08, 2007. University of California, Berkeley, CA, USA. Edited by Paul Kalas., ed. P. Kalas, 47–+

McCaughrean, M. J. & Stauffer, J. R. 1994, *High resolution near-infrared imaging of the trapezium: A stellar census*, AJ, 108, 1382

Menten, K. M., Reid, M. J., Forbrich, J., & Brunthaler, A. 2007, *The distance to the Orion Nebula*, A&A, 474, 515

Metropolis , N. & Ulam, S. 1949, *The Monte Carlo Method*, Journal of the American Statistical Association, 44, 335

Metropolis, N., Rosenbluth, A. W., Rosenbluth, M. N., Teller, A. H., & Teller, E. 1953, *Equation of State Calculations by Fast Computing Machines*, J. Chem. Phys., 21, 1087

Meyer, L., Eckart, A., Schödel, R., Duschl, W. J., Mužić, K., Dovčiak, M., & Karas, V. 2006, *Near-infrared polarimetry setting constraints on the orbiting spot model for Sgr A* flares*, A&A, 460, 15

Monin, J.-L., Ménard, F., & Peretto, N. 2006, *Disc orientations in pre-main-sequence multiple systems. A study in southern star formation regions*, A&A, 446, 201

Muench, A. A., Lada, E. A., Lada, C. J., & Alves, J. 2002, *The Luminosity and Mass Function of the Trapezium Cluster: From B Stars to the Deuterium-burning Limit*, ApJ, 573, 366

Noll, R. J. 1976, *Zernike polynomials and atmospheric turbulence.*, Journal of the Optical Society of America (1917-1983), 66, 207

Nussbaumer, H., Schmid, H. M., & Vogel, M. 1989, *Raman scattering as a diagnostic possibility in astrophysics*, A&A, 211, L27

O'Dell, C. R. 2001, *The Orion Nebula and its Associated Population*, ARA&A, 39, 99

O'Dell, C. R. & Wen, Z. 1994, *Postrefurbishment mission Hubble Space Telescope images of the core of the Orion Nebula: Proplyds, Herbig-Haro objects, and measurements of a circumstellar disk*, ApJ, 436, 194

O'Dell, C. R., Wen, Z., & Hu, X. 1993, *Discovery of new objects in the Orion nebula on HST images - Shocks, compact sources, and protoplanetary disks*, ApJ, 410, 696

Olczak, C., Pfalzner, S., & Spurzem, R. 2006, *Encounter-triggered Disk Mass Loss in the Orion Nebula Cluster*, ApJ, 642, 1140

Ott, T., Eckart, A., & Genzel, R. 1999, *Variable and Embedded Stars in the Galactic Center*, ApJ, 523, 248

Pendleton, Y. J., Tielens, A. G. G. M., & Werner, M. W. 1990, *Studies of dust grain properties in infrared reflection nebulae*, ApJ, 349, 107

Petit, C., Quiros-Pacheco, F., Conan, J.-M., Kulcsar, C., Raynaud, H.-F., Fusco, T., & Rousset, G. 2004, *Kalman-filter-based control for adaptive optics*, in Presented at the Society of Photo-Optical Instrumentation Engineers (SPIE) Conference, Vol. 5490, Advancements in Adaptive Optics. Edited by Domenico B. Calia, Brent L. Ellerbroek, and Roberto Ragazzoni. Proceedings of the SPIE, Volume 5490, pp. 1414-1425 (2004)., ed. D. Bonaccini Calia, B. L. Ellerbroek, & R. Ragazzoni, 1414–1425

Prunet, S. 2007, *Polarization of the Cosmic Microwave Background: an introductory review*, in EAS Publications Series, Vol. 23, EAS Publications Series, 207–234

Ragazzoni, R. & Farinato, J. 1999, *Sensitivity of a pyramidic Wave Front sensor in closed loop Adaptive Optics*, A&A, 350, L23

Reipurth, B., Yu, K. C., Heathcote, S., Bally, J., & Rodríguez, L. F. 2000, *Hubble Space Telescope NICMOS Images of Herbig-Haro Energy Sources: [Fe II] Jets, Binarity, and Envelope Cavities*, AJ, 120, 1449

Rieke, G. H. 2007, *Infrared Detector Arrays for Astronomy*, ARA&A, 45, 77

Robberto, M. 2005, *The distance of the Orion Nebula Cluster*, in HST Proposal, 10552–+

Robberto, M., Beckwith, S. V. W., & Panagia, N. 2002, *The Infrared Emission of Circumstellar Envelopes, Dark Silhouettes, and Photoionized Disks in H II Regions*, ApJ, 578, 897

Robberto, M., O'Dell, R. C., Hillenbrand, L. A., Simon, M., Soderblom, D., Feigelson, E., Krist, J., McCullough, P., Meyer, M., Makidon, R., Najita, J., Panagia, N., Palla, F., Romaniello, M., Reid, I. N., Stauffer, J., Stassun, K., Smith, K., Sherry, B., Bergeron, L. E., Kozhurina-Platais, V., McMaster, M., & Villaver, E. 2005, *An overview of the HST Treasury Program on the Orion Nebula*, in Bulletin of the American Astronomical Society, Vol. 37, Bulletin of the American Astronomical Society, 1404–+

Rohloff, R.-R. 2005, *Piston Mirror Unit*, Tech. Rep. LN-MPIA-FDR-MECH-002, MPIA, Heidelberg, Germany

Sandoval-Villalbazo, A. & Maartens, R. 2005, *Brillouin scattering and the CMB*, General Relativity and Gravitation, 37, 1137

Schödel, R. 2004, *High Resolution Near-Infrared Imaging Observations of the Galactic Centre*, PhD thesis, Fakultät für Physik der Ludwigs-Maximilians-Universität München, Germany. 133 pp. (2004)

Schütz, O. 2005, *High-resolution studies of protoplanetary disks*, PhD thesis, Combined Faculties for the Natural Sciences and for Mathematics of the University of Heidelberg, Germany. IX + 111 pp. (2005)

Schütz, O., Böhnhardt, H., Pantin, E., Sterzik, M., Els, S., Hahn, J., & Henning, T. 2004, *A search for circumstellar dust disks with ADONIS*, A&A, 424, 613

Serkowski, K., Mathewson, D. L., & Ford, V. L. 1975, *Wavelength dependence of interstellar polarization and ratio of total to selective extinction*, ApJ, 196, 261

Setiawan, J., Henning, T., Launhardt, R., Müller, A., Weise, P., & Kürster, M. 2008, *A young massive planet in a star-disk system*, Nature, 451, 38

Shakura, N. I. & Syunyaev, R. A. 1973, *Black holes in binary systems. Observational appearance.*, A&A, 24, 337

Shannon, C. E. 1949, *Communication in the presence of noise*, Proc. Institute of Radio Engineers, 37, 10

Shaw-McMinn, P. G. 2006, *How to provide high-resolution vision: and introductory guide to prescribing iZon lenses*, Review of Optometry, 143, 1CE

Shu, F. H., Adams, F. C., & Lizano, S. 1987, *Star formation in molecular clouds - Observation and theory*, ARA&A, 25, 23

Shuping, R. Y., Bally, J., Morris, M., & Throop, H. 2003, *Evidence for Grain Growth in the Protostellar Disks of Orion*, ApJ, 587, L109

Shuping, R. Y., Kassis, M., Morris, M., Smith, N., & Bally, J. 2006, *Silicate Emission Profiles from Low-Mass Protostellar Disks in the Orion Nebula: Evidence for Growth and Thermal Processing of Grains*, ApJ, 644, L71

Simpson, J. P., Colgan, S. W. J., Erickson, E. F., Burton, M. G., & Schultz, A. S. B. 2006, *Hubble Space Telescope NICMOS Polarization Measurements of OMC-1*, ApJ, 642, 339

Skogestad, S. & Postlethwaite, I. 2005, Multivariable Feedback Control (John Wiley & Sons)

Stauffer, J. R., Prosser, C. F., Hartmann, L., & McCaughrean, M. J. 1994, *Additional constraints on circumstellar disks in the Trapezium Cluster*, AJ, 108, 1375

Störzer, H. & Hollenbach, D. 1999, *Photodissociation Region Models of Photoevaporating Circumstellar Disks and Application to the Proplyds in Orion*, ApJ, 515, 669

Straubmeier, C., Bertram, T., Eckart, A., Rost, S., Wang, Y., Herbst, T., Ragazzoni, R., & Weigelt, G. 2006, *The imaging fringe and flexure tracker of LINC-NIRVANA: basic opto-mechanical design and principle of operation*, in Presented at the Society of Photo-Optical Instrumentation Engineers (SPIE) Conference, Vol. 6268, Advances in Stellar Interferometry. Edited by Monnier, John D.; Schöller, Markus; Danchi, William C.. Proceedings of the SPIE, Volume 6268, pp. 62681I (2006).

Tamura, M., Kandori, R., Kusakabe, N., Nakajima, Y., Hashimoto, J., Nagashima, C., Nagata, T., Nagayama, T., Kimura, H., Yamamoto, T., Hough, J. H., Lucas, P., Chrysostomou, A., & Bailey, J. 2006, *Near-Infrared Polarization Images of the Orion Nebula*, ApJ, 649, L29

Terebey, S., Shu, F. H., & Cassen, P. 1984, *The collapse of the cores of slowly rotating isothermal clouds*, ApJ, 286, 529

Throop, H. B., Bally, J., Esposito, L. W., & McCaughrean, M. J. 2001, *Evidence for Dust Grain Growth in Young Circumstellar Disks*, Science, 292, 1686

Ulrich, R. K. 1976, *An infall model for the T Tauri phenomenon*, ApJ, 210, 377

van de Hulst, H. C. 1957, Light Scattering by Small Particles (Light Scattering by Small Particles, New York: John Wiley & Sons, 1957)

Vasconcelos, M. J., Cerqueira, A. H., Plana, H., Raga, A. C., & Morisset, C. 2005, *Gemini Multi-Object Spectrograph Integral Field Unit Spectroscopy of the 167-317 (LV2) Proplyd in Orion*, AJ, 130, 1707

Vicente, S. M. & Alves, J. 2005, *Size distribution of circumstellar disks in the Trapezium cluster*, A&A, 441, 195

Wang, Y., Bertram, T., Straubmeier, C., Rost, S., & Eckart, A. 2006, *The LINC-NIRVANA fringe and flexure tracker: Linux real-time solutions*, in Presented at the Society of Photo-Optical Instrumentation Engineers (SPIE) Conference, Vol. 6274, Advanced Software and Control for Astronomy. Edited by Lewis,

Hilton; Bridger, Alan. Proceedings of the SPIE, Volume 6274, pp. 62741O (2006).

Whitney, B. A. & Hartmann, L. 1992, *Model scattering envelopes of young stellar objects. I - Method and application to circumstellar disks*, ApJ, 395, 529

—. 1993, *Model scattering envelopes of young stellar objects. II - Infalling envelopes*, ApJ, 402, 605

Whitney, B. A., Kenyon, S. J., & Gomez, M. 1997, *Near-Infrared Imaging Polarimetry of Embedded Young Stars in the Taurus-Auriga Molecular Cloud*, ApJ, 485, 703

Whitney, B. A. & Wolff, M. J. 2002, *Scattering and Absorption by Aligned Grains in Circumstellar Environments*, ApJ, 574, 205

Whitney, B. A., Wood, K., Bjorkman, J. E., & Cohen, M. 2003a, *Two-dimensional Radiative Transfer in Protostellar Envelopes. II. An Evolutionary Sequence*, ApJ, 598, 1079

Whitney, B. A., Wood, K., Bjorkman, J. E., & Wolff, M. J. 2003b, *Two-dimensional Radiative Transfer in Protostellar Envelopes. I. Effects of Geometry on Class I Sources*, ApJ, 591, 1049

Wolfire, M. G. & Cassinelli, J. P. 1987, *Conditions for the formation of massive stars*, ApJ, 319, 850

Yorke, H. W. 2004, *Theory of Formation of Massive Stars via Accretion*, in IAU Symposium, Vol. 221, Star Formation at High Angular Resolution, ed. M. Burton, R. Jayawardhana, & T. Bourke, 141–+

Zavagno, A., Deharveng, L., Brand, J., Massi, F., Caplan, J., Comerón, F., & Lefloch, B. 2005, *Triggered massive-star formation on the borders of Galactic HII regions*, in IAU Symposium, Vol. 227, Massive Star Birth: A Crossroads of Astrophysics, ed. R. Cesaroni, M. Felli, E. Churchwell, & M. Walmsley, 346–351

Ziegler, J. B. & Nichols, N. B. 1942, *Optimum settings for automatic controllers*, ASME Transactions, 64, 759

List of Figures

List of Figures

List of Tables

Danksagung

Erklärung

Ich versichere, dass ich die von mir vorgelegte Dissertation selbständig angefertigt, die benutzten Quellen und Hilfsmittel vollständig angegeben und die Stellen der Arbeit – einschließlich Tabellen, Karten und Abbildungen –, die anderen Werken im Wortlaut oder dem Sinn nach entnommen sind, in jedem Einzelfall als Entlehnung kenntlich gemacht habe; dass diese Dissertation noch keiner anderen Fakultät oder Universität zur Prüfung vorgelegen hat; dass sie – abgesehen von unten angegebenen Teilpublikationen – noch nicht veröffentlicht worden ist sowie, dass ich eine solche Veröffentlichung vor Abschluss des Promotionsverfahrens nicht vornehmen werde. Die Bestimmungen dieser Promotionsordnung sind mir bekannt. Die von mir vorgelegte Dissertation ist von Herrn Prof. Dr. Andreas Eckart betreut worden.

<div align="right">Köln, den 21. April 2008</div>

Teile der Dissertation sind in den folgenden Publikationen enthalten:

Rost, S., Ott, T., Eckart, A. 2008, *Near-Infrared Polarization Images of the Orion Proplyds*, accepted for publication in A&A(date of acceptance: 27/03/2008)

Rost, S., Bertram, T., Straubmeier, C., Wang, Y., & Eckart, A. 2006, *The LINC-NIRVANA fringe and flexure tracker: piston control strategies*, in Proc. SPIE, Vol. 6274, Advanced Software and Control for Astronomy, 62741P

Weitere Veröffentlichungen:

Bertram, T., Arcidiacono, C., Straubmeier, C., Rost, S., Wang, Y., & Eckart, A. 2006a, *The LINC-NIRVANA fringe and flexure tracker: image analysis concept and fringe tracking performance estimate*, in Proc. SPIE, Vol. 6268, Advances in Stellar Interferometry, ed. J. D. Monnier, M. Schöller, & W. C. Danchi, 62683P

Bertram, T., Baumeister, H., Laun, W., Straubmeier, C., Rost, S., Wang, Y., & Eckart, A. 2006b, *The LINC-NIRVANA fringe and flexure tracker: cryoambient mechanical design*, in Proc. SPIE, Vol. 6268, Advances in Stellar Interferometry, ed. J. D. Monnier, M. Schöller, & W. C. Danchi, 62683L

Wang, Y., Bertram, T., Straubmeier, C., Rost, S., & Eckart, A. 2006, *The LINC-NIRVANA fringe and flexure tracker: Linux real-time solutions*, in Proc. SPIE, Vol. 6274, Advanced Software and Control for Astronomy, ed. H. Lewis & A. Bridger, 62741O

Briegel, F., Berwein, J., Kittmann, F., Volchkov, V., Mohr, L., Gaessler, W., Bertram, T., Rost, S., & Wang, Y. 2006, *The LINC-NIRVANA Common Software*, in Proc. SPIE, Vol. 6274, Advanced Software and Control for Astronomy, ed. H. Lewis & A. Bridger, 62741M

Straubmeier, C., Bertram, T., Eckart, A., Rost, S., Wang, Y., Herbst, T., Ragazzoni, R., & Weigelt, G. 2006, *The imaging fringe and flexure tracker of LINC-NIRVANA: basic opto-mechanical design and principle of operation*, in Proc. SPIE, Vol. 6268, Advances in Stellar Interferometry, ed. J. D. Monnier, M. Schöller, & W. C. Danchi, 62681I

Eckart, A., Schödel, R., Straubmeier, C., Bertram, T., Pott, J.-U., Muzic, K., Meyer, L., Moultaka, J., Viehmann, T., Rost, S., & Herbst, T. 2006, *Interferometric observations of the galactic center: LBT and VLTI*, in Proc. SPIE, Vol. 6268, Advances in Stellar Interferometry, ed. J. D. Monnier, M. Schöller, & W. C. Danchi, 62681J